ISSN 1000-9620

海洋通报

Marine Science Bulletin

NATIONAL MARINE DATD AND
INFORMATION SERVICE OF CHINA

2014
Volume 16
Number 2

MARINE SCIENCE BULLETIN

Vol. 16 No. 2 Oct. 2014

CONTENTS

Wave statistics for ship seakeeping in China offshore
..... LIU Shou-hua et al. (01)

Numerical simulation of construction project environmental impact on the tides and tidal currents in Aojiang offshore of Wenzhou ..... LV He-nan et al. (13)

Low frequency shift of wind wasves induced by long waves based on experimental observation data ..... YUE Xin-yang et al. (28)

Numerical modeling of seabed morphological effects from the construction of artificial islands in Danzhou, Hainan ..... YING Xiao-ming et al. (37)

Analysis on the land use and cover change in Tianjin Binhai New Area based on the remote sensing.....WANG Feng et al. (46)

Analysis of the integrated test and evaluation methods of tidal current energy generating devices in the offshore testing site.....GUO Wen-rui et al. (60)

Research on the characteristics of the vortex field of breakwaters by the PIV technique
..... QIE Lu-wen et al. (72)

Comprehensive evaluation of water quality parameters in Tianjin Dagu Dainage Canal
..... DONG Yu-bo et al. (90)

U.S. DEPARTMENT OF COMMERCE
NATIONAL OCEANIC AND ATMOSPHERIC ADMINISTRATION
NOAA

LIBRARY
Pacific Islands Fisheries Science Center
NOAA Fisheries
Honolulu, Hawai'i

Wave statistics for ship seakeeping in China offshore

LIU Shou-hua [1, 2], MU Lin[1]*, WANG Xing[3], CHEN Chang-lin[2], YUE Xin-yang[1], GAO Zhi-gang[1]

1. National Marine Data and Information Service, Tianjin 300171, China;

2. State Key Laboratory of Satellite Ocean Environment Dynamics, Hangzhou 310012, Zhejiang province, China;

3. North China Sea Environmental Monitoring Center, State Oceanic Administration, Qingdao 266033, Shandong province, China

LIBRARY
OCT 21 2015
WITHDRAWN
National Oceanic & Atmospheric Administration
U.S. Dept. of Commerce

Abstract: Ocean waves are the core environmental elements affecting the movements and structure design of ships. Statistical analysis of wave parameters is the basis for the establishment of long-term ship environmental adaptability prediction model. The observations from coastal stations, buoys, altimeters and volunteer ships that cover from 1993 to 2011 were interpolated into miller lon-lat grids by using bilinear method and the analytical fields of ocean waves were given. By using optimal interpolation, the analysis wave fields were assimilated into the WAVEWATCH III (WW3) simulation results. From the assimilated results, the wave rose statistics, the wave height of multiyear return period and the extreme 2-D wave spectrum are related to the ship seakeeping were calculated. Finally, the wave statistics in China offshore were analyzed in detail.

Keywords: ocean waves; statistical characteristics; ship seakeeping; ship environmental adaptability

Ocean wave is a physical phenomenon that exists on the ocean surface, which plays an important role in the movement of ships. Due to the complexity and unpredictability of ocean waves, the statistical characteristics of waves and wave spectrum are commonly used to describe the waves in engineering applications. Ship seakeeping is closely related to the wave height, wave direction and other factors. Thus, a comprehensive understanding of statistical properties of ocean waves would be essential for accurately grasping the characteristics of the ship under outer force, supplying a more powerful database for ship operation. By selecting 19 points in China offshore (Fig. 1), the wave statistics, such as wave height rose, the wave height of multiyear return period and extreme 2-D wave spectrum were calculated for the analysis of coastal wave

Received on Oct. 26, 2013

*Corresponding author: moulin1977@hotmail.com

characteristics in China.

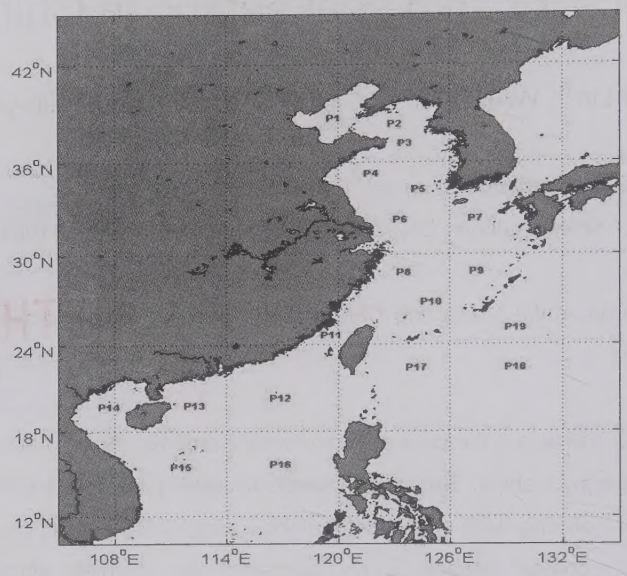

Fig. 1 Distribution of points for wave statistics

1 Dataset

Data used in this study were obtained from the database of National Marine Data and Information Service, including the observations from coastal stations, buoys, satellites and volunteer ships. There are about 70 stations in coastal areas with the longest data sequence up to 50 years. However, the observations only have a representation for shallow water offshore. Buoy observations that have a high precision are relatively far from the land, with limited time coverage not more than 4 years. Volunteer ship data are widely distributed in the ocean including wind waves, swell and wave direction. Nevertheless, the accuracy is insufficient. Observations from satellite altimeter have a better spatial and temporal coverage. The precision is similar to buoy observations (Young, 1999). Since the TOPEX/Poseidon satellite launched in 1992, there are more than 6 satellites with the same mission running in the space and a lot of data have been accumulated. Because the altimeter can only obtain the height information of sea surface, the wave direction is not included in observations.

As the problems demonstrated in the observations, they are really difficult to fully describe the wave directions which are important for the engineering. In view of this, the third-generation wave model WAVEWATCHIII (WW3) is used to simulate the ocean waves by assimilating observed wave data in order to get the wave direction information.

2 Method description

First of all, lon/lat gridded data from 1993 to 2011 was calculated from observations by using bilinear interpolation, with a spatial coverage of longitude 105° - 135°E and latitude 10° - 45° N (Fig. 1). The grid resolution was 0.5° × 0.5° and the temporal resolution was 10 days.

The third generation wave model WW3 (Tolman, 1999) was developed by NOAA/NCEP, based on WAVEWATCH I (Tolman, 1989, 1991) and WAVEWATCH II (Tolman, 1992). WW3 is mainly aimed at the deepwater wave simulation, which doesn't add any constraints on pre-spectra type. The source item functions include wind input, whitecaps dissipation, bottom friction and nonlinear wave interactions. Some improvements have been made in the numerical methods and wind input item, that bring a better computation efficiency and simulation accuracy. For rapidly changing wind and extreme weather conditions, the model can also perform well in the simulation of 1-D and 2-D spectrum (Liu et al, 2009). Due to the lack of wave direction and period information in the observations, we construct a hindcast simulation by assimilating the observed data to supply gridded wave parameters.

The region for numerical simulations has covered the observation positions, with the temporal coverage from Jan. 1st of 1993 to Dec. 31 of 2011. By opening the switch of wind input, whitecaps dissipation, bottom friction and four-wave nonlinear interaction in WW3 model, the simulation is running in the dimensions of frequency and direction besides the spatial dimension. The frequencies were set with the following equation (Eq.1).

$$\sigma_{m+1} = X_\sigma \sigma_m \tag{1}$$

where X_σ is the multiplier factor and is always set the value as 1.1. σ_0 to 0.041 8. The frequencies are set from 0.041 8 to 0.412Hz, with a total of 25 bands. There are 36 directions set with a resolution of 10°.

Optimal interpolation is used to assimilate the gridded observation data. Optimal interpolation method is aimed to find the minimum statistical error in the sense of least square method. It's also known as statistical interpolation method (Voorrips et al, 1997). The first guess field based on observations would be important in the error estimation. The wave spectra from observations is formed according to simulation results. It's assumed that the spectra shape of observations is the same with that of the simulations. The value of the observed 2-D spectrum is adjusted by the wave height ratio between simulation and

observation (Ye qin, 2006).

3 Discussions

Wave height, wave direction and other relative parameters are simulated by WW3 using data assimilation. 19 rose diagrams of significant wave height related to every selecting area are shown (Fig. 2 - Fig. 6). The wave height rose is divided into four intervals, namely 0 m - 1.5 m, 1.5 m - 3 m, 3 m - 6 m, lager than 6 m. P1 is located in the western part of Bohai Sea, and the large waves ranging from 3m to 6 m are mainly in the directions of NNE, N and NE with a proportion less than 1%. Most of the waves are below 3.0 m. P2 is located in the northern Yellow Sea, which is significantly affected by the monsoon, and the waves have a larger proportion in the directions of N and S corresponding to winter and summer, respectively. The waves are small in summer and large in winter. 1.5 m - 3 m, 3 m - 6 m waves are mainly focused in the directions of N and NNW. P3 is located in the central Yellow Sea (the east of Shandong peninsula), which appears a similar wave height rose feature with P2.

P4 and P5 are respectively located in the west and east of southern Yellow Sea and their rose features are almost similar except a slight difference in NNW and SSE directions. Due to being near the east side of mainland, P4 has less waves in NNW direction and more waves in SSE direction. On the other side, P5 is close to the west of Korea, so waves is more in NNW direction, and less in SSE direction. Waves ranging from 3 m to 6 m mainly concentrate in the NW - NNE directions in P4 and P5.

P6 and P8 are close to Chinese mainland, so it takes on similar wave rose characteristics between them. The large waves ranging from 3 m to 6 m are focused in the N - NE direction. Compared with P6, the waves larger than 1.5m in P8 have a higher proportion than P6, which also illustrates that the sea conditions in P8 are rougher than those in P6. P7 and P9 are close to Japan and the Ryukyu Islands, and also have the similar wave height rose features. Large waves from 3 m to 6 m are mainly in NW - N directions. The largest waves are mainly focused in the NNW direction. Compared with P7, the waves higher than 1.5 m in P9 have a larger proportion. Generally speaking, the significant wave height in the south of China Sea is larger than that in the north.

Large waves ranging from 3 m to 6 m in P10 are focused in the directions of N, NNE and NE, where, the waves larger than 1.5 m have a big proportion in N direction. P11 is located in central Taiwan Strait. For the impact of wind and terrain features, waves have an obvious concentration focusing in the NNE and SSW directions. The waves larger than 1.5 m are mainly in the direction of NNE, with a proportion of nearly 20%.

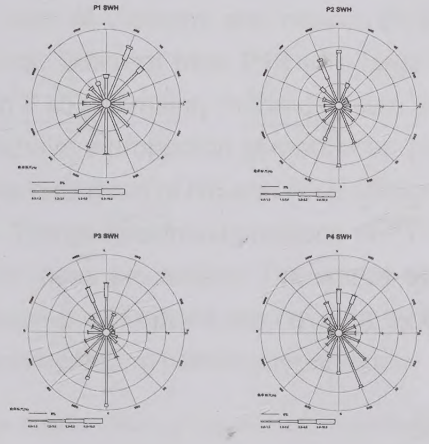

Fig. 2 Significant wave height roses of P1 - P4

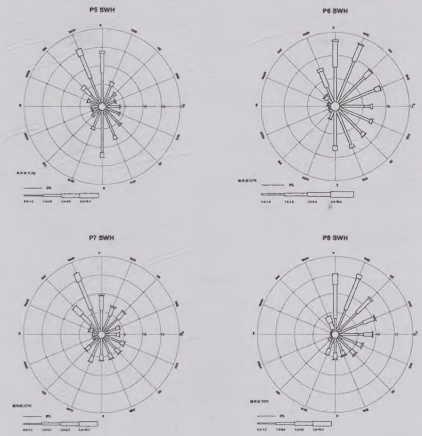

Fig. 3 Significant wave height roses of P5 - P8

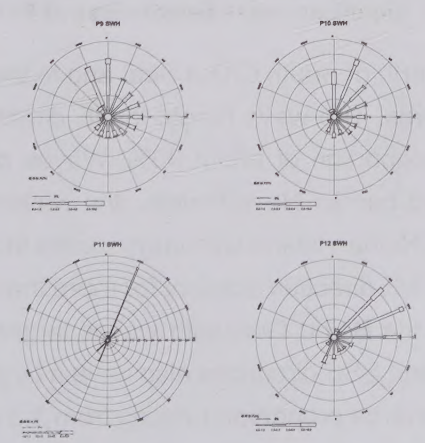

Fig. 4 Significant wave height roses of P9 - P12

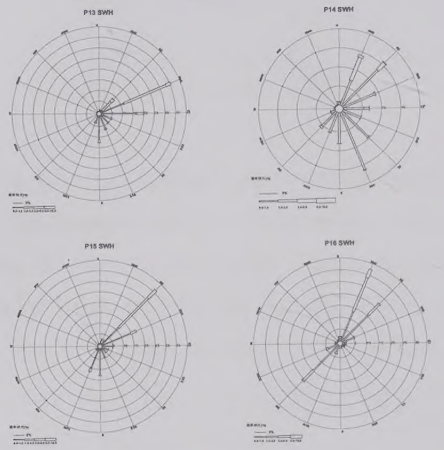

Fig. 5 Significant wave height roses of P13 - P16

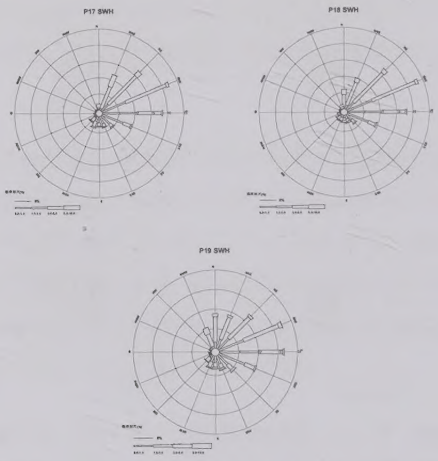

Fig. 6 Significant wave height roses of P17 - P19

P12 is located in the north of South China Sea, and to the east of the Bashi Channel. The area is full of large waves. The wave height in NE direction is large, and the waves larger than 1.5 m have a proportion of about 90%. Waves coming from E direction are relatively small due to a land barrier. Nevertheless, the waves larger than 3 m also exist. P13 is located in the east of Hainan Island with large waves focusing in ENE direction. The waves larger than 1.5 m in ENE direction account for more than 60% and nearly 90% in NE direction. P14 is located in the Beibu Gulf, with waves larger than 3 m focusing in NNE direction. The waves in NE and SSE directions also have a large proportion, and the waves in NE direction are big with a large proportion ranging from 1.5 m to 3 m. The waves in SSE direction are small, and the waves ranging from 0 m to 1.5 m have a proportion more than 90%.

P15 is located in the east of Vietnam, and near to P13. So their wave height rises exhibits similar characteristics. Different from P13 with large waves focusing in the ENE direction, the large waves in P15 are mainly in the direction of NE. The waves larger than 1.5 m in P15 in NE direction have a proportion of more than 70%. P16 is near P14, so their large waves are mainly in the directions of NE and NNE. There are also some waves larger than 1.5 m in SW direction. The geographical positions of P17, P18 and P19 are near and similar, so their wave height roses are similar. The waves above 3 m concentrate in the NNE~ESE directions. Because the locations are covered by the typhoon path in summer, the waves larger than 6 m account for a certain proportion.

Tab. 1 Multiyear return value of significant wave height in P1 - P19 (m)

P	Return years	100 years	50 years	25 years	20 years	10 years	5 years
1		6.55	6.15	5.73	5.60	5.15	4.68
2		6.22	5.96	5.69	5.60	5.31	4.98
3		6.14	5.79	5.43	5.31	4.93	4.51
4		5.96	5.71	5.45	5.37	5.08	4.76
5		7.02	6.81	6.59	6.51	6.26	5.98
6		6.96	6.64	6.31	6.20	5.84	5.44
7		9.78	9.25	8.69	8.51	7.91	7.27
8		11.29	10.54	9.76	9.51	8.69	7.82
9		10.56	9.96	9.33	9.12	8.45	7.71
10		10.51	9.97	9.40	9.21	8.59	7.91
11		8.07	7.57	7.05	6.88	6.33	5.74
12		9.98	9.31	8.63	8.41	7.69	6.92
13		8.69	8.16	7.62	7.44	6.86	6.23
14		7.46	6.98	6.49	6.33	5.80	5.25
15		8.39	7.92	7.43	7.27	6.74	6.18
16		9.24	8.66	8.06	7.87	7.24	6.56
17		11.91	11.25	10.55	10.32	9.54	8.67
18		12.57	11.77	10.93	10.65	9.72	8.70
19		12.51	11.79	11.02	10.76	9.89	8.90

In this study, the multiyear return period values of significant wave height of P1 - P19 are calculated. In a whole view, it takes on the feature that values in the south are larger

than those in the north in China. The 100 year return values of wave height in P1 - P4 are almost below 7 m. Where, P4 is close to the main land and has the lowest value of 5.96 m. The 100 year return value of P8 is relatively large, which is 11.3 m. Because the typhoons always pass through the East China Sea and the South China Sea, the values of multiyear return significant wave height are obviously large. The return wave heights are above 10 m in P8 - P10. P17 - P19 located in the east of Diaoyu Dao have the 100 year return value of 11m, and the value of P18 is up to 12.6 m. The South China Sea is also influenced by typhoon, but the wind speed is significantly reduced after passing the Philippines, which leads to a smaller 100 return value of significant wave height compared with that at the East China Sea. Such as P12 - P16, the 100 return significant wave heights are lower than 10 m.

Because the ocean waves is a very irregular random process, so the ship swaying in ocean waves is also an irregular random process. The swaying motion replication and period of ships is not a constant, but a wide range of random variables. On linear assumption, the boat swaying in irregular waves is composed of numerous shake components respectively transformed from regular waves of different frequencies. Therefore, spectral analysis is used in the research of ship swaying motions in irregular waves. 2-D wave spectrum is the core parameter to study the characteristics of outer force and seakeeping of ships. We present the multiyear max 2-D spectra of P1-P19 (Fig. 7 - Fig. 11).

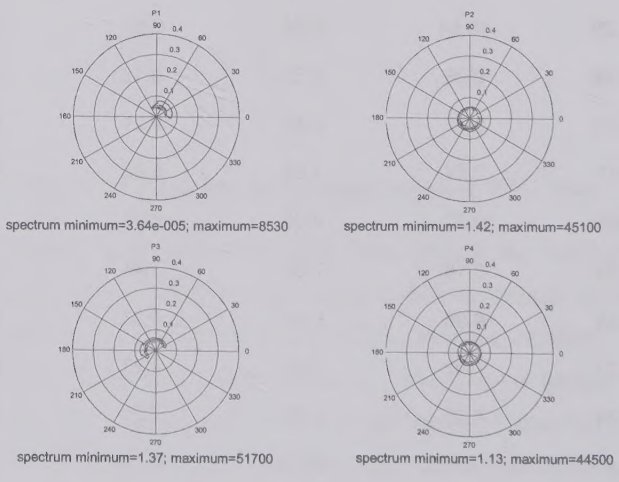

Fig. 7 The distribution of max 2-D spectrum in P1 - P4 (unit: m^2s/ rad)

The maximum of 2-D spectrum in P1 - P19 are extracted from the simulated results. The range of frequency of max 2-D spectrum is almost blow 0.05 Hz (Fig. 7 - Fig.11), which is close to the cutoff frequency of model. The max 2-D wave spectra reflects the direction

and magnitude of maximum significant wave height in a way, which occurs occasionally. P1 - P4 are located in the Yellow Sea and Bohai Sea and the extreme spectral values spread between 8 530 and 51 700. The extreme spectrum values of P1 and P3 appear in N - NNE directions, N - NW directions respectively. The distribution of spectrum in P2, P4 is more disperse compared with that in P1, with the maximum value of 45 100 and 44 500.

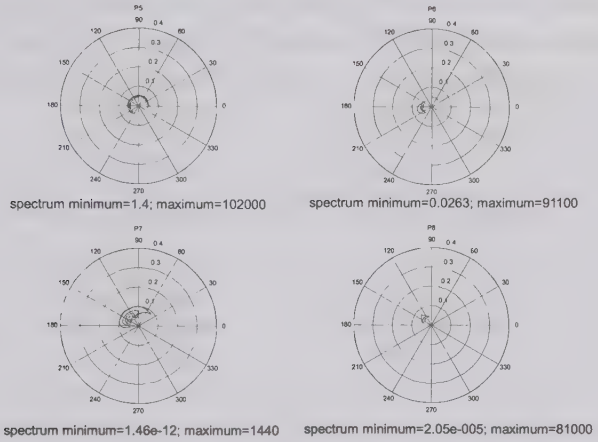

Fig. 8 Distribution of max 2-D spectrum in P5 - P8 (unit: m^2s / rad)

P5 - P10 are located in the Yellow Sea and the East China Sea. The maximum values of the 2-D spectra are higher than those in P1 - P4, with the values larger than 100 000. The distribution of 2-D spectrum in P5 is disperse and concentrated in P6 and P8, which reflects the occasionality of maximum wave height. The maximum 2-D spectra of P9 and P10 are distributed in N~W directions with the extreme values of 169 000 and 189 000 respectively.

Fig. 9 Distribution of max 2-D spectrum in P9 - P12 (unit: m^2s / rad)

The maximum 2-D spectrum has a focused distribution in P11 and P12, which is inconsistent with the wave height rose. The characteristics are related to the typhoon process. It will generate the extreme waves when typhoon passes the area. Due to the rotation of typhoon, the max wave height appears occasionally in all directions, so the max wave spectrum may be inconsistent with the wave height rose. Nevertheless, the maximum 2-D spectrum values in P13 - P16 mainly appear in NW direction, which reflects the general characteristics of the typhoon passing path. And the same feature also exhibits in P17 - P19, with extremes larger than 100 000. The distribution of 2-D spectrum in P17 concentrates, but disperses in P18 - P19.

Fig. 10 Distribution of max 2-D spectrum in P13 - P16 (unit: m^2s / rad)

Fig. 11 Distribution of max 2-D spectrum in P17 - P19 (unit: m^2s / rad)

4 Conclusions

The seakeeping characteristics of ship depend on the wave statistics. We constructed the simulation of ocean waves in China offshore by WW3. Through the assimilation of observations, the wave statistics of 19 points have been analyzed from wave height rose, multiyear return significant wave height and max 2-D spectrum. By using the wave statistics calculated in this study, the seakeeping analysis could be done for every ship. The outer force on the ship could be calculated by the two-dimensional wave spectrum. A method to assimilate the wave simulation results generated by WW3 model has also been given in our study. It also could be used in the real-time forecast models to compute the out force on the ship in future.

Acknowledgement

The authors appreciate supports from National Natural Science Foundation of China (No. 41406032 and No. 41376014) and Open Fund of State Key Laboratory of Satellite Ocean Environment Dynamics (No. SOED1305).

References

[1] Booij N, Ris R C, Holthuijsen L H. A third - generation wave model for coastal regions: 1. Model description and validation [J]. Journal of Geophysical Research: Oceans (1978 - 2012), 1999, 104(C4): 7 649 - 7 666.

[2] Liu S, Sun J, Guan C. Comparisons between the Wind Wave Results from WAVEWATCH III and the Observed Data[C]//The Nineteenth International Offshore and Polar Engineering Conference. International Society of Offshore and Polar Engineers, 2009.

[3] Tolman H L. The numerical model WAVEWATCH: a third generation model for hindcasting of wind waves on tides in shelf seas [R]. Communications on Hydraulic and Geotechnical Engineering, Delft Univ. of Techn. Rep. 1989, No.:89 - 2.

[4] Tolman H L. A third-generation model for wind waves on slowly varying, unsteady, and inhomogeneous depths and currents [J]. Journal of Physical Oceanography, 1991, 21(6): 782 - 797.

[5] Tolman H L. Effects of numerics on the physics in a third-generation wind-wave model [J]. Journal of physical Oceanography, 1992, 22(10): 1 095 - 1 111.

[6] Tolman H L. User manual and system documentation of wavewatch-iii version 1.18. NOAA [R]. Technical Note, 1999, 166.

[7] Voorrips A C, Makin V K, Hasselmann S. Assimilation of wave spectra from pitch and roll buoys in a North Sea wave model [J]. Journal of Geophysical Research: Oceans (1978 - 2012), 1997, 102 (C3): 5 829 - 5 849.

[8] Ye Q. Numerical Simulation and HF radar data assimilation for shallow water waves [D]. Ocean University of China, 2005.

[9] Young I R. Wind generated ocean waves [M]. UK: Elsevier Science Ltd, 1999.

基于舰船耐波性的中国近海海浪特征统计

刘首华[1,2]，牟 林[1*]，王 兴[3]，陈长霖[2]，岳心阳[1]，高志刚[1]

(1. 国家海洋信息中心，天津 300171；2. 卫星海洋环境动力学国家重点实验室 国家海洋局第二海洋研究所，浙江 杭州，310012；3. 国家海洋局 北海环境监测中心，山东 青岛，266033)

摘 要：海浪是影响舰船行进和结构设计的最核心的环境要素。海浪参数的统计分析是建立舰船环境适应性长期预测模型的基础。对 1993 - 2011 年沿海台站、浮标观测资料，高度计观测资料和船舶报观测资料进行双线性插值，给出了海浪波高的分析场。利用波高分析场对 WAVEWATCHIII（WW3）模拟结果进行最优插值同化。给出了海浪统计玫瑰图、极端海浪统计参数和海浪累年二维极值海浪谱等与舰船耐波性有关的海浪统计参数，分析了中国近海的波浪特征。

关键词：海浪；统计特征；舰船耐波性；舰船环境适应性

Numerical simulation of construction project environmental impact on the tides and tidal currents in Aojiang offshore of Wenzhou

LV He-na[1]; WANG Yi-hang[1,3*]; ZHANG Zhao[2]; SHAN Hui-jie[1]; YUE Yun-fei[1]

1. *Ningbo University Faculty of Science, Ningbo* 315211, *Zhejiang province, China;*

2. *Marine Environmental Monitoring Center of Wenzhou, SOA, Wenzhou* 325000, *Zhejiang province, China;*

3. *Ningbo Collaborative Innovation Center of Nonlinear Hazard System of Ocean and Atmosphere, Ningbo* 315211, *Zhejiang province, China*

Abstract: This paper have collected the measured tides and certain tidal current data in different stages of many projects during past three to five years near the Aojiang River. The harmonic method is used to analyze tide and tidal current data observed at five stations in the sea adjacent to Aojiang River. The results show that the tide is mainly regular and semidiurnal in the sea near Aojiang of Wenzhou. The tidal amplitudes of M_2 constituent are between 170 cm - 193 cm and the lags are between 260° - 280°. According to the comparison of analytical results of harmonic constants of these stations in 2007, 2010 and 2011, the maximum change of tidal amplitudes and phase-lag range for the main semidiurnal tides (M_2, S_2, N_2), the diurnal tide (K_1, O_1) and the shallow water tide (M_4, MS_4, M_6) are 1.8 cm - 4.4 cm and 3° - 7°, respectively. After analyzing the tide and tidal current characteristics of Aojiang River, this paper uses an unstructured grid and Finite-Volume Coastal Ocean Model (FVCOM) to test the results of simulation. The simulated results agree well with the measured data. The new shoreline and depth which are produced by the construction projects closed in important major years, and the tide and tidal current field for the new shoreline and depth are constructed, which describe the superimposed influences of construction engineering in Aojiang estuary.

Keywords: Aojiang estuary; tide and tidal current; environmental impact; numerical simulation; post-evaluation

The sea is the advantage and potential for the economic development in Wenzhou. The reclamation plays a positive and important role in economic growth of Wenzhou. Moreover, it is one of the critical ways to relieve the shortage of land and spatial resources.

Received on Jun. 14, 2014

*Corresponding author: wangyihang@nbu.edu.cn

According to "The development planning of the coastal industrial belts between Wenzhou and Taizhou", there will be 34 terms of tideland reclamations, possessing about 370 km^2 areas, along the coast of Wenzhou by 2020 and among which the Aojiang is a typical one. The large and relatively fast-developed reclamation provides the industry improvements of the coast with developing space. However, it also increases the tension on the coast of Wenzhou resulting in many negative benefits for the reclamation, which can usually lower water exchange ability and water self-purification ability, leading to sedimentation and increscence of pollution contents in water. These problems will not only cause a lot of the marine environmental and ecological problems and so on, but also restrict the sustainable development of the marine economy in Wenzhou. The study of reclamation project in Wenzhou on marine environmental impact shows that a single reclamation has little impact on the marine environment in Wenzhou, and the research on the effects of the cumulative reclamation on marine environments is still in the primary stage due to some factors, such as the lack of the typical reclamation engineering group and valuable marine monitoring data, etc. Therefore, the study about effects of the reclamation on marine environments in Wenzhou is a practical and cutting-edge issue. Tides and tidal currents are the typical features of sea that can reflect the marine and ecological environment. Hence, several reclamation projects as well as their effects on tide and tidal currents need to be paid attention for providing some more valuable instances for marine environment.

Many Chinese and foreign researchers have studied the effects of the reclamation on tide and tidal superposition. Until recently, there are already some related researches on effects of offshore construction and engineering in Wenzhou on tide and tidal currents, such as setting up widespread mathematical models of two-dimensional tidal currents and suspending sediment transport including Oujiang River, Feiyunjiang River and Aojiang River. Those projects focus on the long-term reclamation projects' effects on the distribution of the suspended sediments, profiling sand transport rate as well as the evolution of seabed scour and deposition, which belongs to three main rivers flowing into the sea and coastal waters (Wang et al., 2008). Shen et al. (2009) built 2D tidal current numerical model and water exchange model for Wenzhou offshore and estuary, which simulated the effects of the reclamation in Wenzhou on the water exchange capacity for Oujiang River, Feiyunjiang River and Aojiang River estuaries. These studies focused on a large scale area, but didn't accurately assess the changes of the marine dynamic environment of the offshore area. At the same time, some domestic scholars have studied the effects of the cumulative reclamation on tides and tidal currents, such as the analysis of the characteristics of the dynamics and concentration and erosion and deposition in the Bacao Bay(Jiang et al., 2005). Using the Delft3d to model the hydrodynamics of Aojiang estuary, the reclamation influence has been analyzed from tidal prism, tidal level, velocity

and residual flow(Wang et al., 2013); they also retrospectively evaluated the effect of Shenzhen land reclamation engineering on the tide, tidal volume, the marine environment and so on (Guo et al., 2005); the topography and coast line of 1963, 2003 and 2010 were simulated based on POM, and the impact of reclamation on hydrodynamic cumulative effect of the Xiangshan Bay surrounded has been studied by Zeng et al.(2011); Lingni embankment apart of Wenzhou Peninsula Engineering is the first marine engineering implementation of post project analysis on the marine environmental impacts in China (Wang et al.,2010); Wang et al.(2000) and Wang et al.(2010) utilized the establishment of other mathematical models to study the effects of reclamation engineering on the marine environment as well. These scholars focused on the study on river runoff of Aojiang or any other area, while, in this paper we have collected the tide and tidal current data from Aojiang estuary, and then compared and simulated superposition effects and influences of working condition of each process of Aojiang estuary by using the observed data correlation method and combining with irregular triangular grids and finite volume method of FVCOM model. Then the superposition effect of reclamation activities on the Wenzhou Aojiang offshore movement and the scope and degree of impact on the surrounding seas were revealed by using all the information and data, and it is expected to provide examples for the study of the effects of the cumulative reclamation on marine environments, and provide a reference basis for formulating reclamation of superposition effect measures.

We have collected three typical data of tides and tidal currents from the observation of five stations' during the reclamation engineering from 2007 to 2013, which locate in Aojiang offshore. On the basis of analyzing the characteristics of tides and tidal currents of Aojiang, we have used the FVCOM to simulate local tides and tidal currents of Aojiang in order to further verify our calculated results. Then the effects of the reclamation on tides and tidal superposition for each typical reclamation closed time were analyzed by comparing the measured data and simulated data.

1 Introduction for the studied area

Aojiang estuary and offshore is research area in this article, and the exact coordinates are 120.52°E - 120.89°E, 27.42°N - 27.78°N (Fig. 1). As for this area, east-west width is about 36 km, and north-south length is about 40 km, whereas the offshore coastline is very complex. Aojiang is about 90 km long and 1 km wide at the mouth, which is termed as a typical horn. Its climate type is subtropical maritime monsoon, which has mild and humid climate, four distinct seasons and abundant precipitation. The annual precipitation peak is between March and September, among which, March and April are the spring period, May and June are the Meiyu period, July and September are the tropical

storm rain period, and the annai precipitation is diminishing from the land to the island(Li et al., 2012). There are Si Yu Island, San Yu Island, Shang Touyu Island, Suan Yu Island, Tie Tingyu Island and other islands outside Aojiang estuary, and Man Toushan Reef and Feng Huangdan Reef locating in the north of Aojiang estuary. The Aojiang estuary and coast silt year by year due to the upstream flows with sediments and it is affected by sea continental shelf sediment movement sending sediments elsewhere, and expanding the deposition surface, which lead to form the broad estuary and coastal area of tidal flat (Yao et al., 1998; Can et al., 2013; Nanjing Hydraulic Research Institute, 2005). From 1064(the first year of Northern Song Dynasty - Zhiping) to 1979, the coast had moved 2 - 7 km to East China Sea, and the average annual rate was 2.2 m - 7.7 m, while, the rate was 10 - 20 m after the founding of the People's Republic of China. In the south of Aojiang, there are 17 000 acres of reclamation of Jiangnan, which belongs to Cangnan county; in the north, Xiaonan belongs to Pingyang county which has the reclamation of 2 000 acres, and the developed tidal flat area is very broad. The north area connects with Feiyunjiang, and the south area to Pi Pa Hill, with the total reclamation of 255 000 acres. Among them, 120 000 acres have been out of the water; 50 000 acres can be reclaimed in the Jiangnan region; and there are 135 000 acres above the theoretical datum. With the rapid development of Wenzhou economy and the growth of population, there are some reclamation project (Fig. 1) built or to be built for the shortage of land resource and the sustainable development of Wenzhou. The reclamation of Xiwannan, which locates in the north of Aojiang estuary and was constructed from 1999 to 2002, has the reclamation area of 3.48 km^2(5 220 acres) and dike of 5 116 m. The polder of Jiangnan, which locates in the east coast of Cangnan at the south of Aojiang estuary and was constructed from 2007 to 2010, has the reclamation area of 4.69 km^2(about 7 031 acres) and the total area of the ocean is 29.57 km^2. The reclamation of Huarun Cangnan power(including the breakwater), which was constructed from 2008 to 2011, is located in the north of Jiangnan polder.

2 Analysis and comparison for the observation data

2.1 Analysis of the tide features

In this paper, we compare the harmonic constants (Tab. 1) of five stations (Fig. 2) in different years, which locate in Aojiang coastal waters. Through the tide station harmonic analysis results, and according to the formula $(H_{k_1} + H_{O_1})/H_{M_2}$, we calculate the tidal coefficient of each tide station and find that the values are between 0.21 and 0.35, and consequently this area has semidiurnal tides, and the ratios of H_{M_4}/H_{M_2} show us that the

values are 0.007 and 0.01 in Beiji Island and Nanji Island, respectively, and increasing to 0.13 in Aojiang station. The phenomenon shows the tide from the regular semidiurnal tide of Beiji Island to the informal semidiurnal shallow sea tide of Aojiang mouth(Fang et al., 1986). Based on the analysis of the observation data, the tide reaches more than 4 m in the study field, and the tidal day phenomenon is significant, which indicate that the obvious characteristics of semidiurnal tide; the duration of rise and ebb is consistent in the Aojiang estuary, while the spring duration is reduced and ebb duration is increased when it enters the mouth, so the spring duration is less than that of ebb.

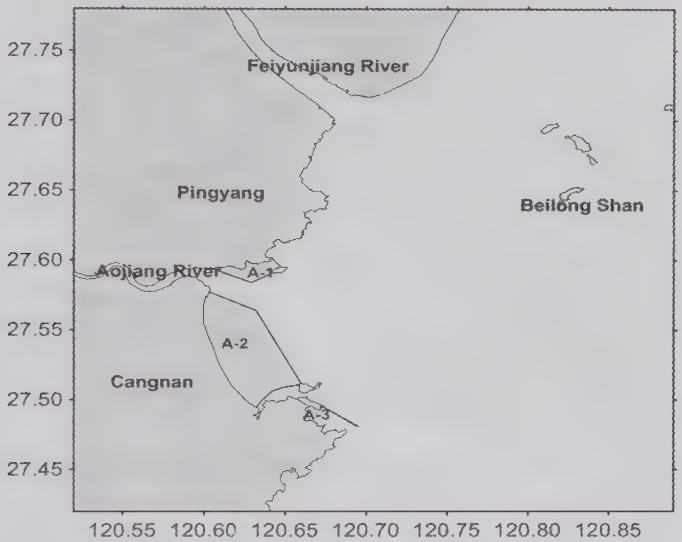

Fig. 1 Schematic map for major sea reclamation projects located in Aojiang estuary

Tab. 1 shows the harmonic constants of five tide stations in the sea adjacent to Aojiang River, and the M_2 constituent dominates in Aojiang district. Considering the results of the harmonic constants of main constituents from the five stations of different years, the majority of partial tide amplitudes have fallen slightly, but the decline range is very limited. The changes of partial tide amplitude are within 5 cm in the Aojiang surrounding waters, and the biggest difference of phase lag is 8.3°, and the range is between 1.5% and 3.0%, which means the range ability is small. Meanwhile, the biggest changes between adjacent years of M_2 amplitude in Aojiang, Shipeng and Beiji stations are 1.6 cm, 2.7 cm and 2.7 cm respectively, and the maximum ratios are 0.85%, 1.39% and 2.46% respectively, and the variational maximum value of phase lags are 5.4 °, 2.3° and 5.4° respectively, so that the effect of M_2 constituent is not significant. We also can know the other partial tides, K_1, O_1, S_2 and N_2 are similar to M_2, and the range ability of amplitude and phase lag are very tiny. And the obvious areas for the shallow water tide M_4, MS_4 are in Aojiang and Shipeng stations, not in Tong Panshan and Beiji stations, and the biggest difference of amplitude

reaches 5 cm, while the changes of them are relatively stable, and M_6 constituent feature is not obvious in all stations. Our computed results show that the cumulative effect of all reclamation on tide is inconspicuous, and the change of tide characteristics is not significant.

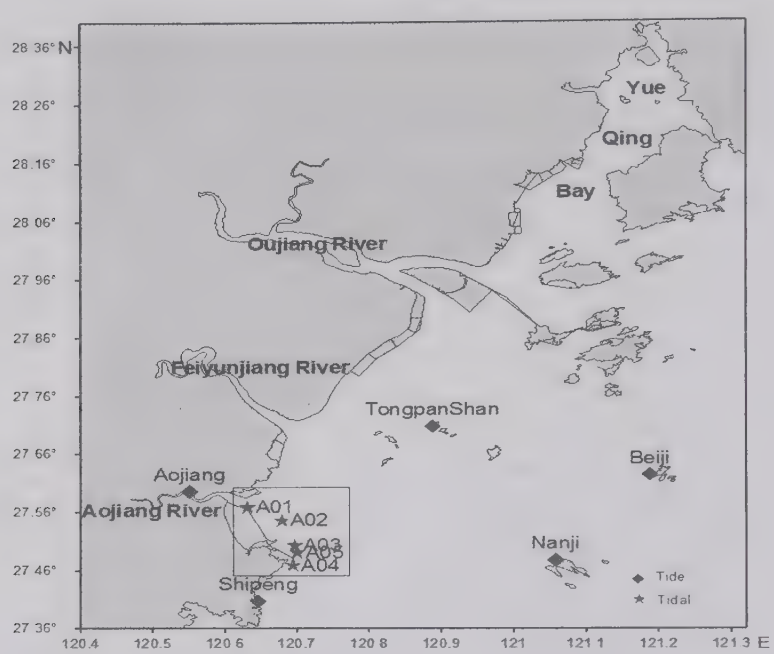

Fig. 2 Calculated range and distribution of measuring stations(diamond-tide measure, star-current measure)

2.2 Analysis of the tidal current feature

As shown in Fig. 2, five consecutive tidal stations, A01-A05 near Aojiang in Wenzhou, are selected and analyzed as typical stations. The property in this sea area is the regular semidiurnal tidal current. The flow velocity decreases gradually from the surface to the bottom, divided into small change in the flow direction, and the flow exhibits reversing current characteristics. In the surrounding of Aojiang, the direction of the spring tide is mainly NW direction, and the ebb direction is mainly SE. The direction for the reversing current is parallel to the coast, while individual site has the rotary current in Cangnan. The spring velocity of Aojiang mouth is mainly influenced by the runoff in the upper, so that the runoff is small in the dry season and spring tide current velocity is sufficiently larger than that of the ebb. The runoff gets bigger in flood seasons, which causes the decrease of spring tidal current velocity, raises duration and increases the ebb velocity and the ebb tide duration, so that the ratio of rise and ebb velocity decreases.

Tab.1 Harmonic constants of five tide stations in the sea adjacent to Aojiang River

Station	Year	M_2		S_2		K_1		O_1	
		H / cm	g / °	H / cm	g / °	H / cm	g / °	H / cm	g / °
Aojiang	2007	187.8	279.1	61.3	324.2	23.5	243.5	20.1	190.6
	2010	189.4	275.7	62.3	319.3	26.5	245.5	21.4	188.6
	2011	189.1	279.4	59.6	326.2	23.1	243.8	18.5	190.6
	2013	189.4	274	63.5	322.7	23.6	236.4	16.9	194.2
Shipeng	2010	193.7	270.7	66.2	312.1	29.4	227.2	24.8	189.6
	2011	191.0	272.8	67.3	313.2	28.8	227.2	23.2	190.6
	2013	191.6	270.5	65.4	313.2	29.5	227.5	23.6	192.5
Tongpanshan	2013	197.9	261.0	68.9	303.9	30.1	222.6	23.4	187.0
Beiji	2009	178.5	260.2	63.1	300.2	29.2	224.7	23.0	189.1
	2010	174.1	263.1	62.9	303.6	28.6	224.3	23.2	187.1
	2011	172.1	264.1	62.0	304.3	28.7	224.8	22.3	188.0
	2013	170.0	268.3	62.1	312.6	29.3	228.1	22.4	191.4
Nanji	2008	151.1	265.7	71.7	309.8	30.4	196.6	22.7	189.6

Station	Year	N_2		M_4		MS_4		M_6	
		H / cm	g / °	H / cm	g / °	H / cm	g / °	H / cm	g / °
Aojiang	2007	34.4	264.7	24.8	136.4	17.4	178.5	4.8	303.2
	2010	33.0	261.3	22.7	134.5	14.0	174.8	4.7	270.9
	2011	32.9	265.0	21.7	135.3	17.1	183.0	2.2	269.7
	2013	34.7	259.6	19.5	112.5	15.4	164.5	5.2	233.4
Shipeng	2010	33.7	256.3	3.8	31.1	3.6	75.3	2.1	92.6
	2011	33.2	258.5	5.0	29.7	4.4	72.4	2.1	91.3
	2013	33.3	256.1	4.6	31.3	3.4	76.5	2.2	77.1
Tongpanshan	2013	34.4	246.7	4.1	353.5	4.6	48.0	2.7	75.0
Beiji	2009	31.1	245.9	0.4	231.7	0.2	105.9	1.0	76.9
	2010	30.3	248.8	1.0	1.5	1.6	45.7	0.8	71.0
	2011	29.9	249.7	1.3	351	1.6	44.6	1.0	68.2
	2013	29.6	254	2.4	8.6	2.8	57.1	2.4	53.3
Nanji	2008	65.5	242.8	11.5	158.2	3.9	89.1	7.0	220.2

According to the estuary of Aojiang to the outlets, from the velocity and duration of spring and ebb tidal current, the ebb velocity and duration are greater than those of flood tide due to the influence of the upstream runoff, and they are both gradually weakened;

and the estuary belongs to a typical strong tidal creek estuary, which is influenced by the runoff and tide; and its surrounding waters belong to typical rectilinear currents, and spinning is not strong. Since the Aojiang river mouth area has regular semidiurnal tidal currents and the M_2 constituent is as main constituent, we analyze the ellipticity value K and the long axis of the ellipse of M_2 of five different years and continuous flow stations. We find that the ellipticity value K of M_2 in 2011 has changed insignificantly by comparing with those in 2010 and 2007, and the values are between 0.01 and 0.03 in all the measured stations. At the same time, the value of the long axis of M_2 in 2011 is slightly less than that in 2007, with the average velocity of 0.05 m/s, and the direction represents the tidal wave propagation direction, and its size represents the maximum velocity of tide of the corresponding tidal constituent. Therefore, superimposed effect of the outer reclamation engineering on the surrounding sea tidal movement is not significant in Aojiang surrounding waters.

3 Superimposed effect simulation and impact assessment

3.1 Establishment and validation of the model

3.1.1 Introduction for FVCOM

Due to the limitation of the measured data in time and space, it is difficult to systematically evaluate data in future only with the measured data. However, the numerical model based on a large amount of measured data can more accurately simulate in the whole area and can verify the related numerical data. It is an efficient evaluation method for post evaluation. We have built three dimensional hydrodynamic models FVCOM (an unstructured grid, Finite-Volume Coastal Ocean Model) (Chen et al., 2006) by analyzing the terrain and land boundary data of 2007, 2010 and 2011 in this study, which investigate the simulation of the superposition effect and influence of each process in Aojiang waters. The FVCOM employs the finite-volume method which can well combine the advantage of finite element method and the finite difference method. It can guarantee the conservation of mass, momentum and energy for the computation though the coast is complex. It uses a σ-coordinate in the vertical direction that can be good to adapt to the changes of terrain, and can use unstructured triangular mesh nonoverlapping in the horizontal direction, which can fit the complicated coastal and can make refinement mess for the focus area. It uses the Mellor-Yamada 2.5 turbulence closure model for calculating vertical mixing coefficients, and uses the Smagorinsky formulation for calculating horizontal mixing coefficients. In addition, it applies a mode-splitting technique for splitting the fast moving gravity wave modes outside from the slow moving internal. Therefore, we have built FVCOM models for

the coast of Aojiang waters, which are complex, and have harbour large tidal flat area and uneven distribution in the area. The level, velocity, and flow are validated using the data of 2007, 2010 and 2011.

3.1.2 Setting up model

As shown in Fig. 3, this research mainly investigates Aojiang area, for which the north-south length is 155 km and east-west width is 134 km, and the horizontal resolution varies from 50 m in the offshore to 2 000 m in the sea, and there are six distributed layers in the vertical direction. Though there is debugging in this mode, the computational time steps of 6s and 30 s are used for the external and model respectively. There are 168 307 units and 88 363 nodes in the whole area. This design of the mode grid can depict the complex of coastline, which is caused by the ocean engineering construction.

The friction coefficient of bottom is as follow:

$$C_d = \max\left(\frac{k^2}{\ln\left(\frac{z_{ab}}{z_0}\right)^2}, 0.0025\right) \tag{1}$$

where Z_0 is the roughness of the seabed and the value is 0.01 in this simulation after debugging, and k is the Karman constant and the value is 0.4, and Z_{ab} is the distance between the latest grid and the bottom of the sea. In this mode, the value of bottom friction coefficient is 0.004.

The open boundary conditions are specified in the form of sea surface elevation:

$$\zeta = \sum_i f_i H_i \cos(\omega_i t + v_{0i} + u_i - g_i) \tag{2}$$

where ζ is the tidal level, ranging from 1 to 8, and just represents the eight main constituents, including M_2, S_2, K_1, O_1, N_2, K_2, M_4, MS_4. ω_i is the tidal angular velocity. f_i and μ_i are the nodal factors and nodal phase correction respectively. H_i and g_i are the tidal harmonic and constants, and their values are based on the tidal harmonic and constants which we have collected in Wenzhou offshore and the previous results taken as the reference after debugging(Chen et al., 2003). The model starts from static sea and continues to compute for one month after obtaining stable tide, employing the least square method to analyze the harmonic analysis and features of the tide and tidal currents.

3.1.3 The validation of tide elevation

In order to further verify our calculated results, we compare time series in one month for two tide stations: Aojiang and Beiji (Fig. 2). Actual observed sea levels and stimulated ones are shown in Fig. 4. The mean-root-square error for Aojiang and Beiji are 0.18 m (2007.04) and 0.19 m (2011.04), 0.11 m (2007.07) and 0.15 m (2007.07) respectively. The simulated tide elevation is more accurate. The results show that the stimulated model has better agreement with the actual tidal change of Aojiang in Wenzhou.

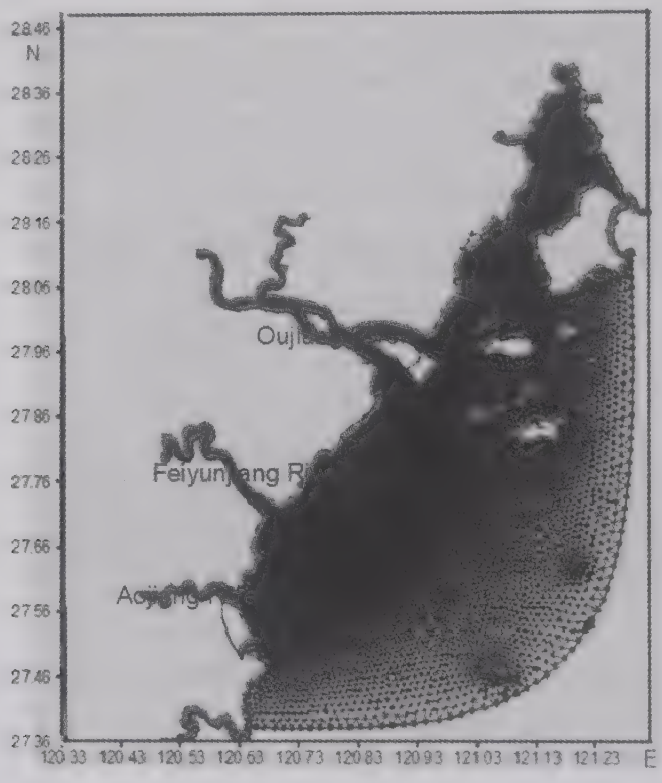

Fig. 3 Grid of calculated range

3.1.4 The validation of tidal current

Comparison of two tidal stations A02 and A05 between observed and modeled values of flow velocity and direction in the surface and underlying are shown in Fig. 5. Both of the tidal currents in two sites are regular semidiurnal tidal currents, which can also be concluded from the simulation results. From the contrast of flow velocity and direction, the simulation results are basically consistent with the measured ones, and the direction is better in agreement with the actual measurement data. The mean-root-square errors of flow velocities in A02 and A05 in the surface and underlying are 9.8 cm/s, 8.9 cm/s, 7.8 cm/s

and 5.7 cm/s，respectively. The mean-root-square errors of flow direction are 17.3°, 22.4°, 19.1° and 21.2° respectively. The simulated flow velocity and direction fit well with the observation. The results show that the mode can well response the change of tidal currents in Aojiang.

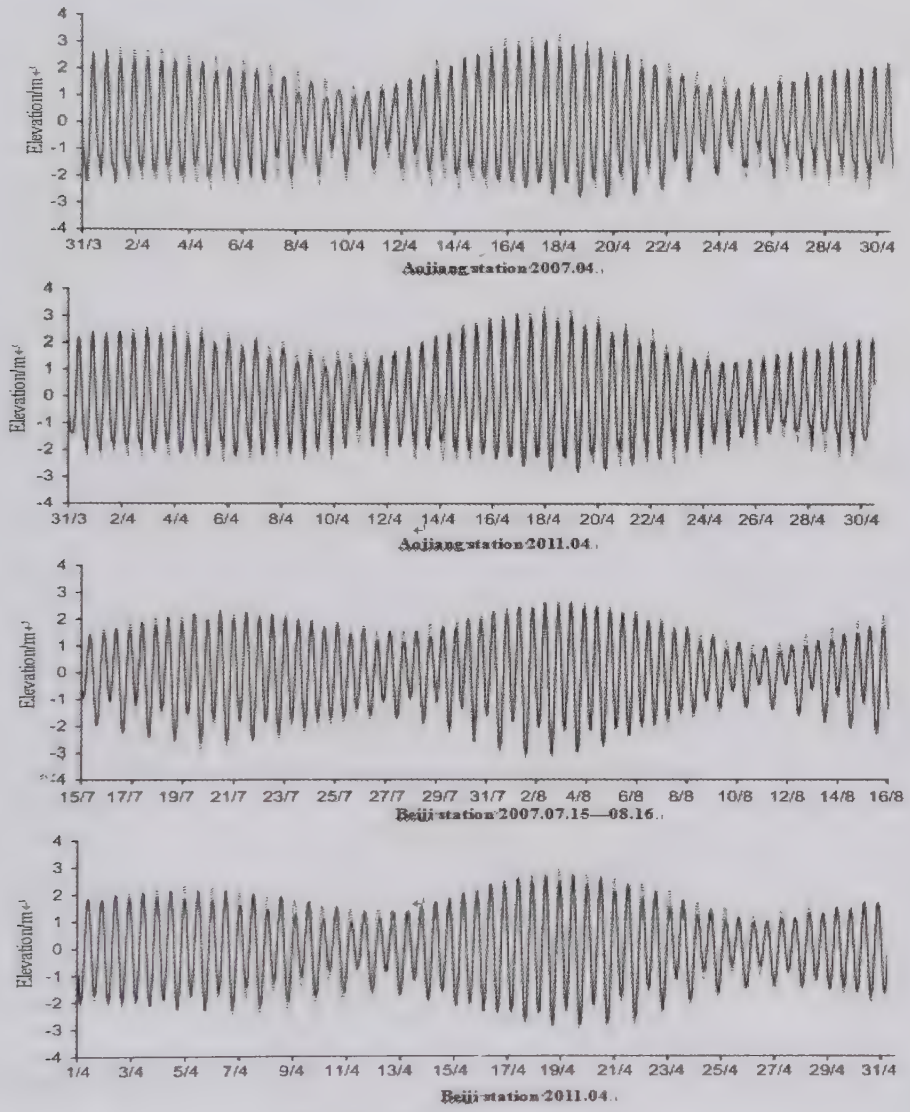

Fig. 4 Elevation comparison between simulated and measured values in Aojiang and Beiji

3.2 The change of the flow field

From the spring and ebb tide graphs of flow field in different years, it shows that the reclamation project does not change superimposed effect in the following state in the sea area near Aojiang and the overall framework of tidal current field in Aojiang doesn't change

neither. The flow direction is mainly from the northwest to southeast, which is caused by the morphology of terrain. The water mainly flows from southwest to northeast during the spring tide, and from northeast to southwest during the ebb tide. The graphs of flow fields for spring and ebb tides in 2007and 2011 are shown in Fig. 6 and Fig. 7, respectively.

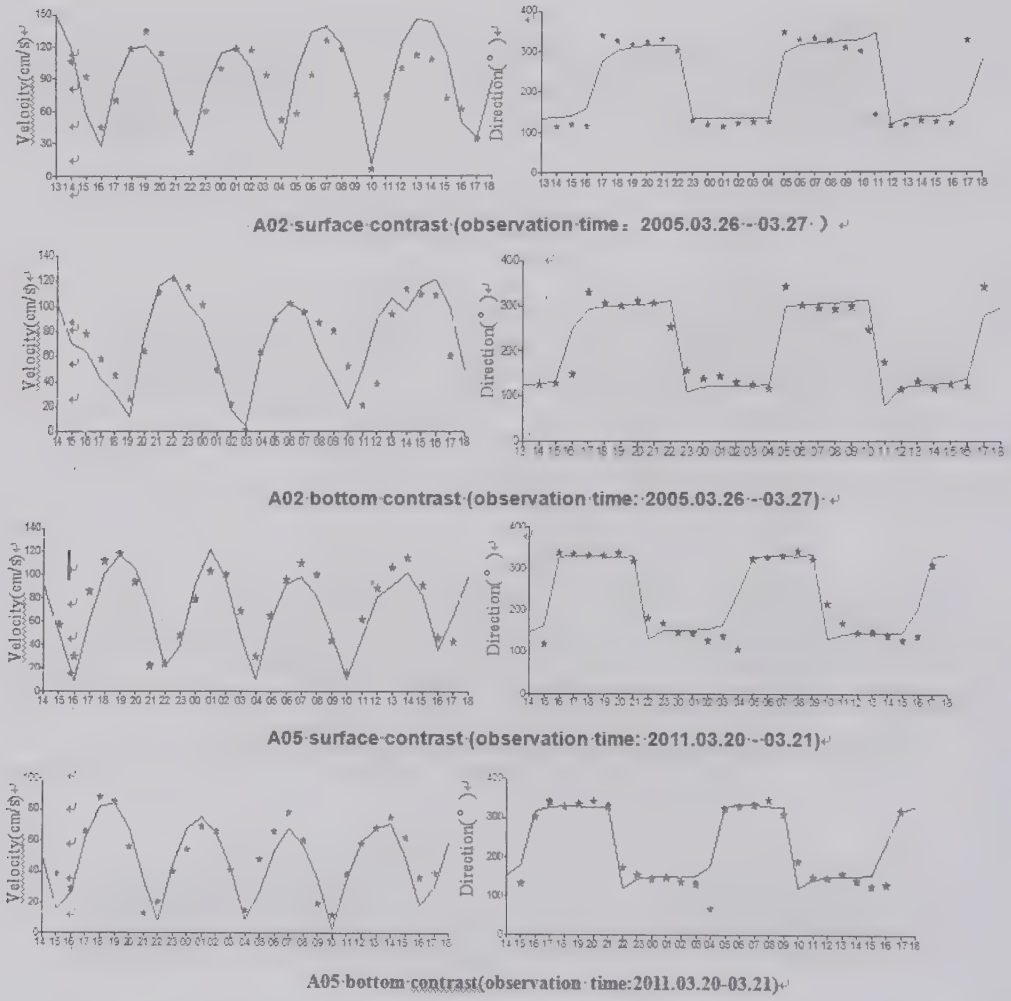
Velocity(cm/s)
Direction(°)
A02 surface contrast (observation time: 2005.03.26--03.27)
A02 bottom contrast (observation time: 2005.03.26--03.27)
A05 surface contrast (observation time: 2011.03.20--03.21)
A05 bottom contrast(observation time:2011.03.20-03.21)

Fig. 5 Flow velocity and direction compariosn between simulated values(line) and measured ones(small star) in A02 and A05

As shown in Fig. 6, the overall flow field has little change before and after the reclamation of Jiangnan polder and Cangnan Power when ebb happens in Aojiang estuary. There is little change in the edge of the reclamation for the tidal current in the size of the current, but the direction largely follows along the beach to the southeast direction. Fig. 7 indicates that the tidal currents south of the Cangnan power are consistent before and after

the works. Although the direction diverts to the north based on the northwest direction reclamation before the Jiangnan polder, and the current velocity increases slightly, other sea areas have little change. Above all, the flow field has no significant change in Aojiang before and after the reclamation works.

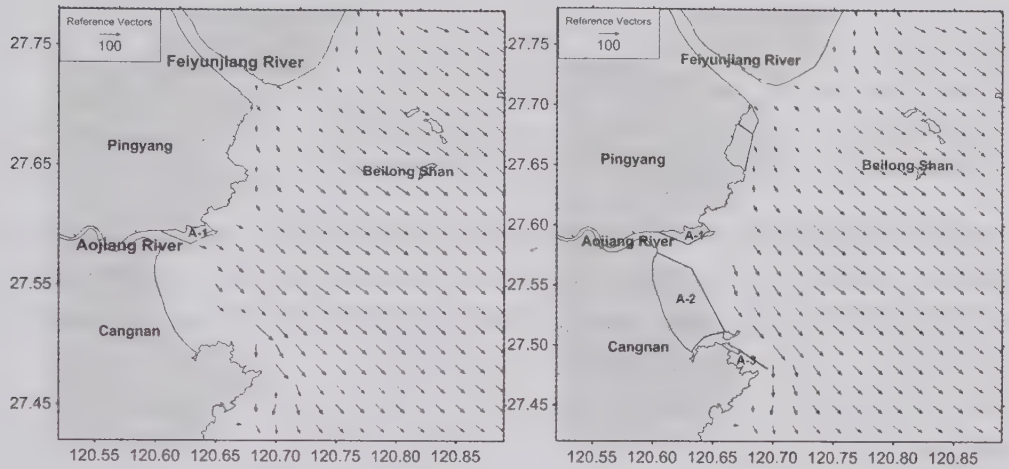

Fig. 6 Current fields in Aojiang offshore at the ebb in 2007 (left) and 2011 (right)

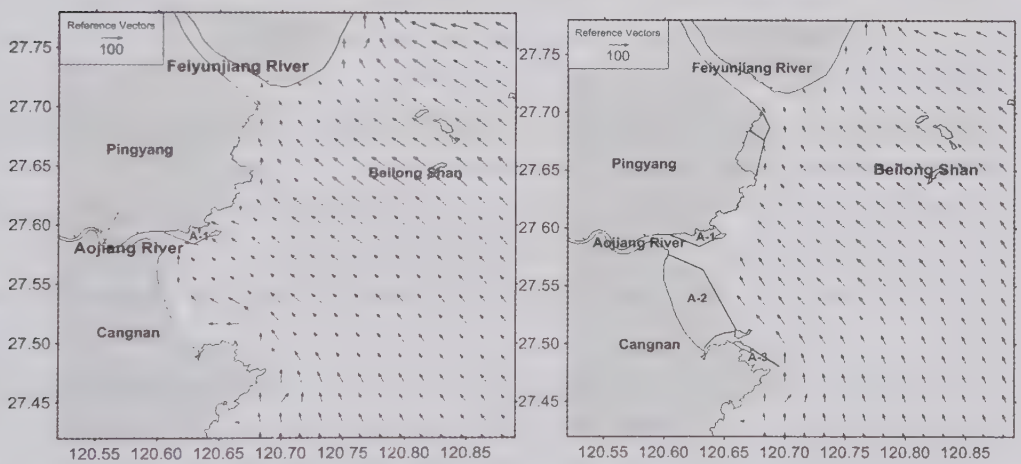

Fig. 7 Current fields in Aojiang offshore at the spring in 2007(left) and 2011(right)

4 Conclusions

Through the analysis and calculation for the real measured data for Aojiang offshore superposed influences of tide and tidal currents from the reclamation can be concluded as follows:

(1) Through comparing and analyzing the measured data of 2007, 2010 and 2011,

the tide level has little change in these years. The difference of tide amplitudes and lags for M_2, S_2, N_2, K_1, O_1, M_4, MS_4 and M_6 are in 1.8 cm - 4.4 cm and 3° - 7° respectively. These data demonstrate that cumulative effects of all reclamation works on tides are inconspicuous.

(2) By the comparison with the realistic data, the result shows that ellipticity value K of tidal component M_2 in 2011 had no obvious change, compared with those in 2010 and 2007. The value of the long axis of M_2 in 2011 is slightly shorter than that in 2007. Therefore, the reclamation works slightly change the superposed influence of the tide and tidal currents surrounding Aojiang.

(3) Both the stimulation and actual measurement confirm the accuracy of the model. The good agreement of stimulation results with the real data suggests this research reasonable. Through the analysis of the flow field of flood and ebb in different years, it can be found that the change is not significant in Aojiang.

References

[1] Chen C S, Robert C, Beardsley R C. An Un-structured Grid, Finite-Volume Coastal Ocean Model-FVCOM User Manual. Data Assimilation Methods, MASS-Dart-mouth Technical Report, 2006, 06 - 0602.

[2] Cai D D, Zhou H C, Wang S S, et al. The analysis of the evolution characteristics of the beach in Wenzhou Feiyunjiang and Aojiang [J]. Zhejiang Hydrotechnics. 2013, 3:14 - 18.

[3] Chen Q, Huang D J, Zhang B Z, et al. The research of the tidal features in the coastal zone of Zhejiang Province [J]. Donghai Marine Science, 2003, 21(2): 1 - 12.

[4] Fang G H, Zheng W Z, Chen Z Y, et al. Analysis and prediction of tides and tidal currents [M]. 1986: 474.

[5] Guo W, Zhu D K. Reclamation and Its Impact on Marine Environment in Shenzhen Area, China [J]. Journal of Nanjing University (Natural Sciences), 2005, 41(3): 286 - 296.

[6] Jiang G J, Li X Y, Yao Y M, et al. The Change of Dynamics and Concentration and Their Influence on the Erosion and Deposition in the Bacao Bay [J]. South Zhejiang, China, Marine Science Bulletin, 2005, 24(2): 33 - 39.

[7] Li M G, Wen C P, Cai Y, et al. Advances in research and development in Wenzhou sea area [J]. Journal of Waterway and Harbor, 2012, 33(4): 277 - 290.

[8] Nanjing Hydraulic Research Institute, Zhejiang province Wenzhou Shipping Management Office, The overall planning of Ruian port. Nanjing: Nanjing Hydraulic Research Institute, 2005.

[9] Shen L J, Chen D X, Huang H M, et al. Impact of reclamation project on the water exchange capacity of the estuaries in Wenzhou [J]. Journal of Marine Sciences, 2009, 27(4): 72 - 76.

[10] Wang L, Jiang G J. Impact of Jiangnan reclamation in the Aojiang estuary on the discharging capacities and residual flow [J]. Marine Science Bulletin, 2013, 32(5): 559 - 567.

[11] Wang L S, Fang Z J, Huang H M, et al. Impact of reclamation on the sediment transport in the Wenzhou offshore and estuarine waters [J]. Journal of Waterway and Harbor, 2008, 29(6):386 - 393.

[12] Wang X, Chen W Q, Jiang Y W, et al. Evaluation of losses in bay environmental capacity based on numerical simulation-a case study of sea reclamation in Tong'an Bay, Xiamen [J]. China Environmental Science, 2010, 30(3): 420 - 425.

[13] Wang X C, Sun C Q, Sun Y L, et al. Study on impact of Jiaozhou Bay sea- filling on hydrodynamic environment [J]. Marine Environmental Science, 2000, 19(3): 55 - 59.

[14] Wang Z Y, Bao X W, Wang S G, et al. A primary study on methods of post project analysis on marine environmental impact assessment in China—Post project analysis of Lingni embankment's impacts on marine environment as an example [J]. Marine Environmental Science, 2010, 29(1): 139 - 144.

[15] Yao Y M, Chen J Y, Chen Y P, et al. The Relationship between Current and Topography in Wenzhou Bay [J]. Journal of East China Normal University (Natural Science), 1998, 2: 61 - 68.

[16] Zeng X M, Guan W B, Pan C, et al. Cumulative influence of long term reclamation on hydrodynamics in the Xiangshangang Bay [J]. Journal of Marine Sciences, 2011, 29(1): 73 - 83.

温州鳌江近海建设工程环境影响潮汐潮流数值模拟

吕和娜[1]，汪一航[1,3*]，张 钊[2]，单慧洁[1]，岳云飞[1]

（1. 宁波大学理学院，浙江 宁波 315211；2. 国家海洋局温州海洋环境监测中心，浙江 温州 325027；
3. 宁波非线性海洋与大气灾害系统协同创新中心，浙江 宁波 315211）

摘 要：收集了近年来鳌江口附近海域多个工程不同阶段 5 个潮位站的 3～5 年潮位实测数据和部分海流实测资料，通过对鳌江口附近海域的不同年份的水位资料进行潮汐调和常数分析，鳌江近海海域主要为半日潮区，其中 M_2 分潮的振幅在 170 cm ～ 193 cm；迟角在 260°～280°之间，这些站的 2007 年、2010 年、2011 年调和常数分析结果相比，主要的半日分潮 M_2、S_2、N_2，全日分潮 K_1、O_1 及浅水分潮 M_4、MS_4、及 M_6 等分潮振幅、迟角的最大变化分别在 1.8 cm ～ 4.4 cm 和 3° ～7° 之间。在初步掌握了鳌江口潮汐潮流特征的基础上，采用无结构的三角形网格和有限体积法的 FVCOM 海洋数值模型，进行模拟结果验证，计算结果与实测数据符合良好。构建重点年份建设工程合拢产生新的岸线水深的潮汐潮流场，刻画鳌江口建设工程的叠加影响。

关键词：鳌江口附近海域；潮汐；潮流；环境影响；数值模拟；后评价

Low frequency shift of wind waves induced by long waves based on experimental observation data

YUE Xin-yang[1], ZOU Xiao-chen[2], LIU Shou-hua[1, 3, 4*], LI Xiao-guang[1]

1. *National Marine Data and Information Service, Tianjin* 300171, *China;*

2. *College of Physical and Environmental Oceanography, Ocean University of China, Qingdao* 266100, *Shandong province, China;*

3. *The Second Institute of Oceanography, SOA, State Key Laboratory of Satellite Ocean Environment Dynamics, Hangzhou* 310012, *Zhejiang province, China;*

4. *Key Laboratory of Ocean Circulation and Waves, Chinese Academy of Sciences, Qingdao* 266071, *Shandong province, China*

Abstract: The influence of long regular waves on wind waves are examined in the laboratory tank. The wave spectra of wind waves are compared when there is and there is not long waves. Besides the widely addressed suppression of wind waves by long waves, it is also found that, the presence of long regular wave induces low frequency shift of wind waves when long wave slope is small and also its frequency f_l is quite apart from wind wave crest frequencies f_p. The effect of long wave modulation on wind wave spectra is estimated according to Longuet-Higgins & Stewart (1960) (abbreviated as LS60 afterwards), which is found to be prominent at the large ratio of f_p/f_l. It's also found that, when the limitation of wave breaking on wind wave steepness is taken account of, the LS60 theory can explain the low frequency shift satisfactorily. The work suggests that, at small long wave slope and large ratio of f_p/f_l, the LS60 modulation mechanism together with the enhanced wave breaking may dominate the influence of long waves on wind waves.

Keywords: wind wave; swell; long wave-short wave interaction

1 Data and methods

Waves normally show as mixed waves combining wind waves and swell together, which is not the simple superposition, and the swell influence the wind waves in many aspects. Understanding the characteristics of the mixed waves and revealing the effect of swell modulation on wind waves are important to the ocean wave theory, ocean remote sensing and ocean engineering. Using laboratory tank to observe mix waves is an effective

Received on Feb. 16, 2014

*Corresponding author: huazai950@hotmail.com

method to study the interaction mechanism.

The research of the influence of long regular waves on short gravity waves has experienced more than half a century, and a variety of possible mechanism has been proposed during this period. Longuet-Higgins et al (1960) (abbreviated as LS60 afterwards) proved the nonlinear factor of second-order and came up with the variation in the wave number and amplitude of the short waves, according to the study that long wave modulation on the short wave is on the basis of surface wave potential currents theory. Phillips (1981) used the natural coordinate system which is shifted with the swell to bring up the dispersion of long wavelets in the dominant orbital velocity of long wave, and the modulation in the long wave amplitude is given by using the action conservative equation. Longuet-Higgins (1987) established the fully nonlinear theory of the long wave-short wave interaction according to the increasing of long wave slope. In these theories, the long wave modulation on the short wave may be dominated by the effects of convergence, divergence and radiation stress. Phillip et al. (1974) indicated that the wind wave break was the effect of swell modulation on wind drift, which would change wind wave spectra. The amplitude of wind waves is the greatest at wave crest and lowest at wave trough according to this mechanism, opposite to the LS60 theory. Chen et al. (2000) (abbreviated as CB2000 afterwards) suggested that the dominate modulation mechanism might be the blockage of long waves on the wind stress. Although the ratio of wave spectra of wind waves in order 0 when there is and there is no swell close to the observation data given by CB2000 and Phillips(1983), the mechanisms are quite different. Masson（1993）studied the influence of four-wave resonance interaction mechanism on the coupling between swell and wind waves. It is believed that, the wind wave energy will transfer to swell when their frequency is very close, and the energy transfer is negligible when well frequency is quite apart from wind wave frequency. Although there are many correlation studies, the law and mechanism of swell modulation on wind wave remain unclear. There is still more detailed work to do. The influences of long regular waves on wind waves are examined in the laboratory tank. The long wave inducing low frequency shift of wind waves is taken the consideration of and explained.

2 Experimental observation

The experiment is examined in wind-wave-current laboratory in the college of Physical and Environmental Oceanography in Ocean University of China. The tank is 65 m × 1.2 m × 1.5 m. There are a wave maker and a wind blower on one side of the tank to generate regular waves and wind waves. And there is a wave dispersion on the other side to reduce the reflection. The wave gauge made of Ta material and its diameter is 5 mm

which is used to measure the transient height of the surface(precision is 1 mm). The wave gauge is placed in 11 m, 19 m, 26 m and 35 m fetch. Its sampling frequency is 50 Hz, and sampling time is 5 min. The wind speed is measured by the anemometer which is placed 30cm higher on the mean water. During the experiment, we first generate regular waves by wave maker, then open the wind blower, and the measurement begins when the mix wave is stable. The parameters of regular waves are shown in Fig. 1 Mix waves of each regular wave are generated by 4 m/s, 7 m/s and 10 m/s wind speed.

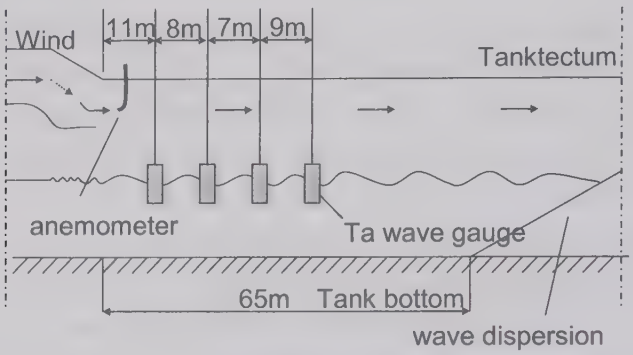

Fig. 1 Sketch of the experimental set-up

Tab. 1 Parameters of regular waves

wave slope	wave height / mm	period / s
0.01	35	1.5
0.02	70	1.5
0.04	140	1.5
0.06	210	1.5

The wave spectra is calculated by using Fourier coefficient. Comparing the pure wind wave spectra and mixed wave spectra with regular wavelet, it is found that, the influence characteristic of long waves on wind waves are as follows:(1)suppression of wind waves, when long wave slope S_l is 0.04 or 0.06, wind waves nearly disappear. (2) low frequency shift of wind waves. Huang et al. (2009) analyzed the first characteristic in detail, we focus on the second characteristic in this study. The related theories and experimental researches mentioned refer in section one addressed the suppression of wind waves by long waves, and the second characteristic was not mentioned. Fig. 2 shows the wave spectra when regular wave length is 0.35 m, period is 1.5 s and wind speed are 4 m/s, 7 m/s

and 10 m/s respectively, and the low frequency shift of wind waves is obvious. When S_l =0.01, the suppression of wind waves by regular waves is not obvious and the low frequency shift is prominent especially when wind speed is low and fetch is short. When S_l =0.02, the low frequency shift is covered up by the suppression of wind waves. So the data produced when S_l = 0.01 is used in this paper to study the possible mechanism of low frequency shift induced by long waves.

3 Observation data analyze

The wave spectra is calculated by using Fourier coefficient. Comparing the pure wind wave spectra and mixed wave spectra with regular wavelet, it is found that, the influence characteristics of long waves on wind waves are as follows: (1) Suppression of wind waves, when long wave slope S_l is 0.04 or 0.06, wind waves nearly disappear. (2) Low frequency shift of wind waves. Huang et al. (2009) analyzed the first characteristic in detail, we focus on the second characteristic in this study. The related theories and experimental researches mentioned in section one addressed the suppression of wind waves by long waves, and the second characteristic was not mentioned. Fig. 2 shows the wave spectra when regular wave length is 0.35 m, period is 1.5 s and wind speeds are 4 m/s, 7 m/s and 10 m/s respectively, and the low frequency shift of wind waves is obvious. When S_l =0.01, the suppression of wind waves by regular waves is not obvious and the low frequency shift is prominent especially when wind speed is low and fetch is short. When S_l =0.02, the low frequency shift is covered up by the suppression of wind waves. So the data produced when S_l = 0.01 are used in this paper to study the possible mechanism of low frequency shift induced by long waves.

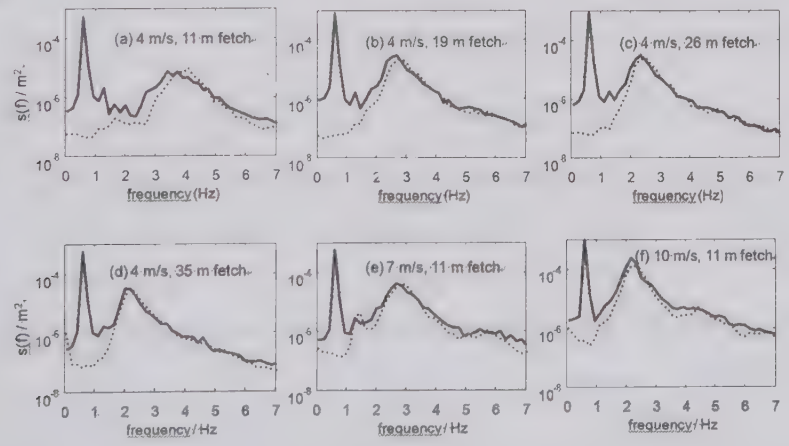

Fig. 2 The comparison of pure wind wave spectra (dashed line) and mixed wave spectra (solid line)

4 The possible mechanism of low frequency shift induced by long waves

The suppression of wind waves by long waves will induce high frequency shift of wind waves (according to CB2000). In an earlier paper (Phillips et al., 1974), it was shown that the modulation mechanism of long waves on wind wave breaking is the wind drift, that causes the smallest at long wave crest. Cong et al. (2010) analyzed the distribution of wind wave energy which was influenced by regular wave phase of the mix waves in the experimental observation, and it was found that, the wind wave was the greatest around the regular wave crest, satisfying the LS60 theory. So in this paper, we try to use the LS60 theory and take the limitation of wave breaking on wind wave into account to find out whether the LS60 modulation mechanism can explain the frequency shift of wind waves.

When the amplitude is short, the pure wind wave is:

$$\zeta(t)=\sum_{n=1}^{\infty} a_n \sin(\omega_n t+\varepsilon_n) \tag{1}$$

where, a_n, ω_n and ε_n are the amplitude, angular frequency and initial phase of the $\zeta_n(t)$. Simplify the long regular wave of this experiment into sine wave, in the given fetch, that is:

$$\zeta_l(t)=a_l \sin(\omega_l t) \tag{2}$$

where a_l and ω_l are the amplitude and angular frequency of long waves. In a second-order approximation, the $\zeta_l(t)$ modulation on the amplitude and phase of $\zeta_n(t)$, $\zeta_n'(t)$ is the modulated $\zeta_n(t)$, according to LS60 that is

$$\zeta_n'(t)=a_n\begin{bmatrix}\sin(\omega_n t+\varepsilon_n)\\ +a_l k_l \sin(\omega_l t)\sin(\omega_n t+\varepsilon_n)\\ -\frac{k_n}{k_l}a_l k_l \cos(\omega_l t)\cos(\omega_n t+\varepsilon_n)\end{bmatrix} \tag{3}$$

The modulated phase shift of wind waves can be shown as the linear super position of $\zeta_n'(t)$, in such that

$$\zeta'(t)=\sum_{n=1}^{\infty} a_n\begin{bmatrix}\sin(\omega_n t+\varepsilon_n)\\ +a_l k_l \sin(\omega_l t)\sin(\omega_n t+\varepsilon_n)\\ -\frac{k_n}{k_l}a_l k_l \cos(\omega_l t)\cos(\omega_n t+\varepsilon_n)\end{bmatrix} \tag{4}$$

As shown in equation(4), when the amplitude of wind waves and slope of long waves is small, the modulation of wind waves is dominated by the ratio of wavelet number $\frac{k_n}{k_l}$, that is, the modulation is more obvious when the frequency of wind wave crest is quite apart from long waves. In laboratory, when k_l is given, wind speed small, fetch short, and wind wave frequency is apart from long waves, the modulation is obvious. It may be because the influence of long wave modulation on wind waves is prominent. Fig. 3(a) shows the pure wind wave spectra and the modulated spectra of $\zeta'(t)$ when wind speed is 4 m/s and fetch is 11 m, and the amplitude and period of regular waves are 35 mm and 1.5 s. The comparison of pure wind wave spectra and $\zeta'(t)$ spectra is shown in Fig. 3(a), which indicates that, the influence of long regular waves on wind waves will enhance the wind wave energy and widen the spectra.

By comparing the mix wind wave spectra and $\zeta'(t)$ spectra shown in Fig. 3(a), the energy of high frequency of mix wind wave spectra is lower. In fact, the wave slope will increase around the long wave crest and the wave will break when wave slope is bigger than the limit, which means the waves, of which the slope is bigger than the limit, are unreasonable and can no longer be maintained.

$\zeta_n(t)$ is given according to the calculation of the amplitude and initial phase of each wave by using the observation data of pure wind wave surface shift, and the $\zeta'(t)$ is calculated by using equation (4). When reading the wave slope of each time zones from $\zeta'(t)$, in order to avoid the interference of high frequency burr of the wave surfer, we cut of the high frequency from the summation of the waves calculated by equation (4) and take the pure wind wave crest frequency which is 1.5 times. The Fourier coefficient is used to calculate the spectra of $\zeta''(t)$, and $\zeta''(t)$ is the rest waves form $\zeta'(t)$, of which the wave slope is under limitation.

There are differences on the wave slope limit between different researchers. Ochi and Tsai (1983) came up with the criterion for the limit of single wave break based on laboratory data, which is $H/gT^2 \geq \delta$, where *H*, *T* and *g* are wave height, period and gravity. The δ are 0.020 and 0.027 for deepwater random wave and regular wave, that is close to

the theory of Michell (1893) and Longuet-Higgins (1975). According to the result of this paper, the spectra of $\zeta''(t)$ coincide well with the wind wave spectra of the measured mix wave spectra. In Fig. 3(a), the modulated spectra ($\zeta''(t)$ spectra) and the spectrum after the breaking is taken into account. It is shown that, the dissipation of high frequency is enhanced and the wind wave spectra low frequency shift is induced by the wave breaking. The Fig. 3 shows the pure wind wave spectra, mix wave spectra, $\zeta'(t)$ spectra and $\zeta''(t)$ spectra of the other three fetches, of which the wind speed is 4 m/s and the 11 m fetch, of which the wind speed is 7 m/s and 10 m/s, and the wave height of regular wave parameters is 0.35 m and periods are 1.5 s.

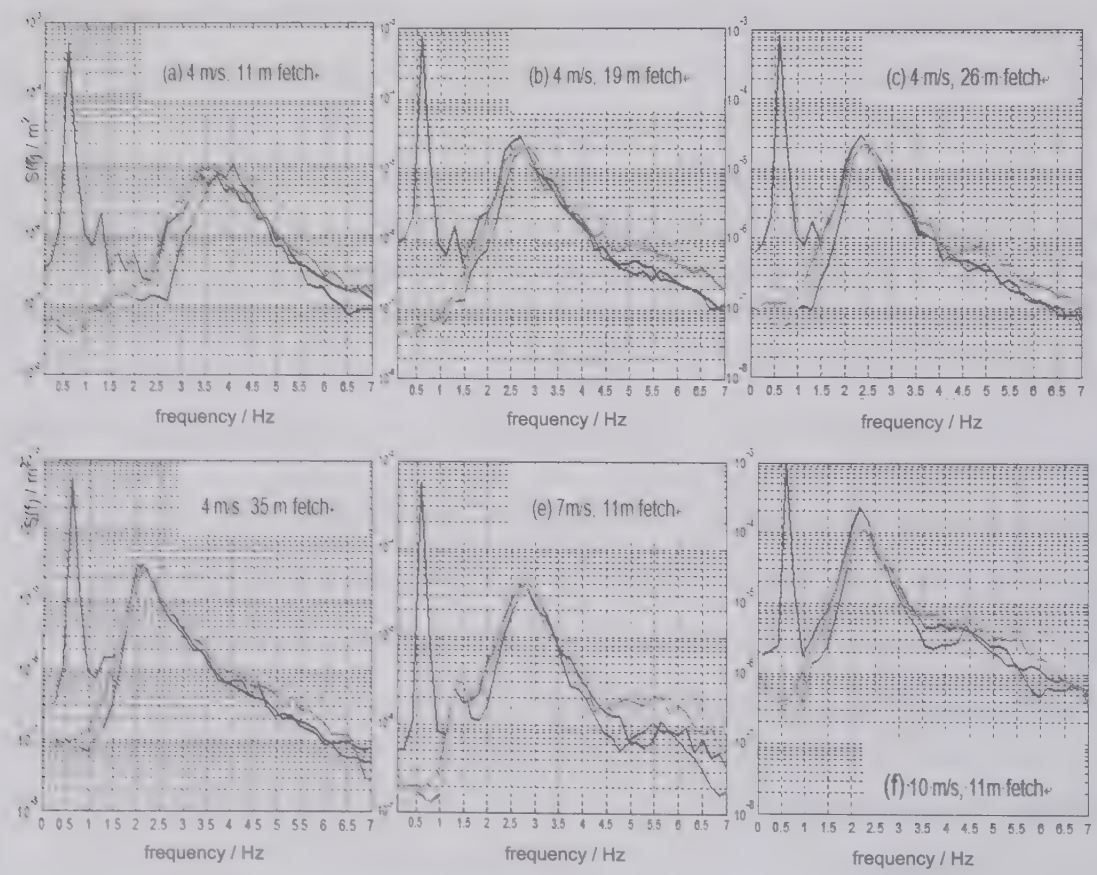

Fig. 3 Effect of long wave modulation (according to LS60 theory) as well as wave breaking on wind waves

(The solid, dotted, dashed, long dash-dot represented the measured mixed wave spectra, the measured pure wind wave spectra, the modulated spectra and that after breaking is taken into account.)

5 Conclusions

The influence of long regular waves on wind waves are examined in the laboratory tank. The wave spectra of pure wind waves and mix waves are compared. It is found that, it presences the low frequency shift of wind waves and there is hardly any suppression when regular wave slope is small. According to LS60, the sequence of long regular wind waves is calculated, the modulation mechanism and wind wave spectra change induced by the limitation of wave breaking on wind wave steepness are analyzed. It is found that, the LS60 modulation mechanism is prominent when long wave frequency is quite apart from the wind wave peak frequency, and this modulation mechanism together with the limitation of wave breaking on wind wave steepness can explain the low frequency shift satisfactorily. Thus, when long wave slope is small while its frequency is quite apart from wind wave peak frequencies, the LS60 modulation mechanism together with the enhanced wave breaking may dominate the influence of long waves (for example, swell) on wind waves.

References

[1] Longuet-Higgins M S, Stewart R W. Changes in the form of short gravity waves on long waves and tidal currents [J]. Fluid. Mech., 1960, 8: 565 - 583.

[2] Phillips O M. The dispersion of short wavelets in the presence of a dominant long wave [J]. Fluid. Mech. 1981, 107: 465 - 485.

[3] Longuet-Higgins M S. The propagation of short surface waves on longer gravity waves [J]. Fluid. Mech., 1987, 177: 293 - 306.

[4] Phillips, O M, Banner M L. Wave breaking in the presence of wind drift and swell [J]. Fluid. Mech., 1974, 66: 625 - 640.

[5] Chen G, Belcher S E. Effects of long waves on wind-generated waves [J]. Phys. Oceanogr., 2000, 30: 2 246 - 1 156.

[6] Masson D. On the nonlinear coupling between swell and wind waves [J]. Phys. Oceanogr., 1993, 23: 1 249 - 1 258.

[7] Huang B G, Zheng G Z, Cong P X. Laboratory Research on the Influence of Swell on Wind Wave Energy, Periodical of Ocean University of China.2009,39(3): 381 - 386.

[8] Cong P X, Zheng G Z, Pei Y H. Phase modulation of short wind waves by long waves. Advances in Water Science, 2010, 21(2): 261 - 266.

[9] Ochi M K, Tsai C H. Prediction of occurrence of breaking waves in deep water [J]. Phys. Oceanogr., 1983, 13: 2 008 - 2 019.

[10] Michell J H. The highest wave in water. Phil. Mag., 1893, 36: 430 - 437.

[11] Longuet-Higgins M S. Integral properties of periodic waves of finite amplitude. Proc. Roy. Soc., London, 1975, A342: 157 - 174.

实验室观测条件下的规则长波对风浪低频频移影响

岳心阳[1]，邹晓晨[2]，刘首华[1,3,4*]，李晓光[1]

（1. 国家海洋信息中心，天津 300171；2. 中国海洋大学海洋环境学院，山东 青岛 266100；
3. 卫星海洋环境动力学国家重点实验室 国家海洋局第二海洋研究所，浙江 杭州 310012；
4. 中科院海洋环流与波动重点实验室，山东 青岛 266071）

摘 要：本文利用实验室波浪水槽观测规则长波对风浪的影响。谱分析显示，较之纯风浪谱，除已被广泛关注的长波抑制风浪这一现象外，当长波波陡较小，且频率远离风浪峰频时，长波还使得风浪谱向低频移动。本文利用 Longuet-Higgins & Stewart（1960）理论，并考虑到风浪破碎的约束，计算了规则长波的存在对风浪谱的影响，发现可以较好地解释这一现象。这一工作表明，当长波波陡小且频率远离风浪峰频时，长波对短波的二阶调制及其引起的破碎加强可能是长波影响风浪的主要机制。

关键词：风浪；涌浪；长-短波相互作用

Numerical modeling of seabed morphological effects from the construction of artificial islands in Danzhou, Hainan

YING Xiao-ming, JIA Hou-lei, CAO Ling-long, XIE Jian

South China Sea Marine Engineering and Environment Institute, State Oceanic Administration, Guangzhou 510300, *Guangdong province, China*

Abstract: Haihua Islands is a large artificial island in Danzhou, Hainan. The construction of Haihua Islands changes the hydrodynamic environment of Yangpu waters, and further affects its morphological change. Delft3D is used to set up a two dimensional nested hydrodynamic and sediment model for Yangpu waters in this paper, and this paper focuses on simulating the velocity and morphological change due to the construction of Haihua Islands after the verification of the model. The seabed deposition is small because of low suspended sediment concentration and less sand source near Yangpu waters. The bed level erodes in the south area of Xiaochan Reef and the Yangpu channel due to the velocity increase in the area.

Keywords: Haihua Islands; seabed morphological effect; numerical modeling

1 Introdution

The regional marine construction of Haihua Islands is located in the Yangpu waters in Danzhou ,Hainan (Figure 1), near the Baimajing Town. The project intends to adopt the form of an offshore artificial island with planning five artificial islands, and bridges among the islands and between the island on both sides and the land in the Baimajing Town (South China Sea Marine Engineering and Environment Institute, 2012).

The tidal trend is irregular diurnal in Yangpu waters, and the tidal flow is of the reciprocating flow with a slight rotation. The measured surface flow velocity is about 0.82 m/s, and the annual average wave height is 0.8 m in Dongfang Station near the project. The suspended sediment concentration (SSC) is low with the average value of 0.02 - 0.03 kg/m^3, and the sea bed is mainly silty clay (South China Sea Marine Engineering and Environment Institute, 2012). The minimum area of the five artificial islands is about 0.1 457 km^2, and the maximum area is about 3.811 4 km^2, and the distance among the

Received on Jul. 10, 2014

Corresponding author: yingxm@scsb.gov.cn

islands is about 48 m - 196 m. Haihua Islands is mainly located in Yangpu shallows (Fig. 1) with the depth less than 2 m. The tidal passage of the Yangpu Bay is a curved deep channel with the length of 8.2 km, width of 600 m and depth of 10 m - 20 m. The deepest depth is above 24 m, and the shallowest depth is about 5 m in the sandbar area, and the length of the depth less than 8.5 m is about 3.5 km.

Haihua Islands belongs to a large-scale reclamation project, and the project implementation causes hydrodynamic environment changes in Yangpu waters and adjacent area, further affects the sea bed morphological change. The evolution of sea bed sedimentation and erosion is worth to study. The numerical model of Delft3D is used to simulate the effects of sea bed morphological change caused by the project and the reasons are analyzed in this paper.

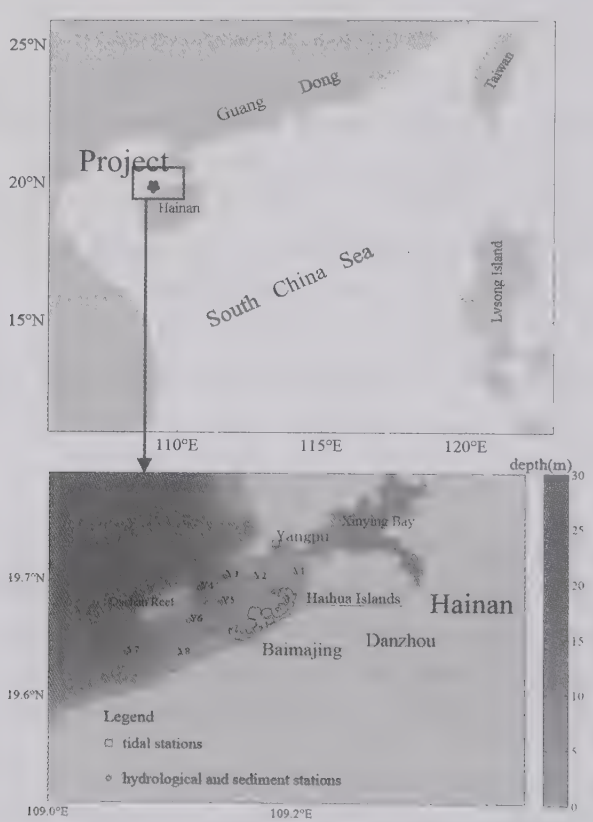

Fig. 1 Location of Haihua Islands in Hainan, the depth of Yangpu waters and hydrological stations

2 Numerical model

In this study, the numerical model of Delft3D is used to establish a wide range of

Hainan Island and a nested two dimensional hydrodynamic and sediment model in the vertical average for Danzhou sea water. The sediment model of Delft3D is currently more advanced model of sediments in the world, in which the water depth and topography are coupled and simulated simultaneously. The Delft3D integrates modules of hydrodynamic, water quality, ecology, sediment transport and morphological change, etc (Lesser, et al., 2004). The model is developed earlier, and relatively stable and powerful, so there is a wide applications in many areas in many countries (Smit, et al., 2008, Hu, et al., 2009, Jeuken and Wang, 2010).

Delt3D is used to study fluid and material transport in rivers, estuaries and coastal regions by solving the three-dimensional shallow water equations of motion (the free surface of a three-dimensional Navier-Stokes equations of incompressible fluid). The model adopts the orthogonal curvilinear grid, which simulates the curved shoreline better. The model provides Cartesian and spherical coordinates, and uses the staggered grid solving variables by ADI (Alternative Direction Implicit scheme) method. The model uses moving boundary processing technology with dry and wet, while it provides visualization module for the pre-processing and post-processing. The basic equations of the water fluid movement and sediment transport in orthogonal curvilinear coordinates see Delft3D manual (Deltares, 2011).

3 Model setup and verification

3.1 Model setup

Model uses two-grid nesting mode (Fig. 2). The number of grid for the big area is 112 × 122; the range is about longitude 105.6 ° E - 112.3 ° E, latitude 16.6 °N - 21.8 °N, the maximum grid spacing of ξ direction is about 6 254 m, and the minimum grid spacing is about 1 690 m; the maximum grid spacing of η direction is about 15 655 m, and the minimum grid spacing is about 1 847 m. The number of grid for the detailed area is 210 × 278; the range is about longitude 108 °E - 109.3 °E, latitude 19.2 °N - 20.4 °N; the maximum grid spacing of ξ direction is about 4 021 m, and the minimum grid spacing is about 17 m; the maximum grid spacing of η direction is about 4 082 m, and the minimum grid spacing is about 26 m. Islands and land filling works within the scope of simulation are represented by the dry point in model grids.

The water level boundaries are set on the open boundary in the big model. Open boundary of flow velocity is driven by the change of water levels. The eight tidal constituents are selected to calculate water level in this paper, including M_2, S_2, K_1, O_1, N_2, K_2, P_1, Q_1.The initial value of the eight tidal constituents are obtained from global harmonic

constants TPXO7.2 (http://volkov.oce.orst.edu/tides/global.html), and further adjusted based on harmonic analysis of the model. The SSC at open boundary is set to 0. The wind field data are obtained from http://www.esrl.noaa.gov/psd/data/gridded/data.ncep.reanalysis.surface. html. The spatial resolution is 2.5°, and the frequency is one day.

The open boundary of detailed model is set to the water level nested from the big model. The manning coefficient is about 0.013.The time step is 1 minute and 0.5 minute for big model and detailed model, respectively. The frequency of morphology update is 12 hours, taking into account the impact of SSC on water density. The wave is neglected due to low annual average in Yangpu waters.

The sediment erosion stress and deposition stress are set to the equal value, with the range of 0.13 - 0.20 N/m^2. The erosion parameter M is approximately 1×10^{-6} - 1×10^{-5} $kg/m^2/s$, and the sediment settling velocity is about 5×10^{-4} mm/s. All of the parameters are set referring to papers (Hu, et al., 2009 and Xie, et al., 2009), and further determined in accordance with the verification of the model.

3.2 Model verification

The big model mainly provides water level for the detailed model. Limited by observed data, the water level is only verified at Yangpu tidal station in the big model, and the water level is adopted from the tidal chart in 2011. The location of Yangpu tidal station see Fig. 1. The comparison results of fundamental six tidal constituents are shown in Tab. 1. The amplitude error is less than 1.2 cm, the phase-lag error is less than 2°, which indicates that the big model can simulate the variation of water level well.

Tab. 1 Comparison of fundamental tidal constituents (unit: amplitude, cm; phase-lag, degree)

Constituent	M_2		S_2		K_1		O_1		P_1		Q_1	
	amplitude	Phase-lag	amplitude	Phase-lag	amplitude	Phase-lag	amplitude	Phase-lag	amplitude	Phase-lag	amplitude	Phase-lag
Tidal chart	22. 5	139	5.8	199	75.6	87	84.8	25	23.3	79	17.2	352
Simulation	22.4	138	6.1	203	76.8	87	85.9	25	23.8	78	17.3	352
difference	-0.1	-1	0.3	4	1.2	0	1.1	0	0.5	-1	0.1	0

Flow velocity and SSC are verified in the detailed model. The observed stations are shown in Fig. 1. The results of four stations are shown in Fig. 3 and Fig. 4 for the velocity and SSC, respectively. Because the distance among observed stations are small, and the results of other four stations are not shown. The error between simulated flow velocity and flow direction is small, the variation processes of simulated and observed velocities are

similar, which indicates the parameters adopted in the detailed model can better simulate the variation of flow velocity in the study area, and the detailed model can simulate the velocity field well. The error between simulated SSC and observed SSC is less, indicating the sediment parameter adopted by the detailed model can better simulate suspended sediments in the study area. The measured SSC indicates that the SSC is low in the study area.

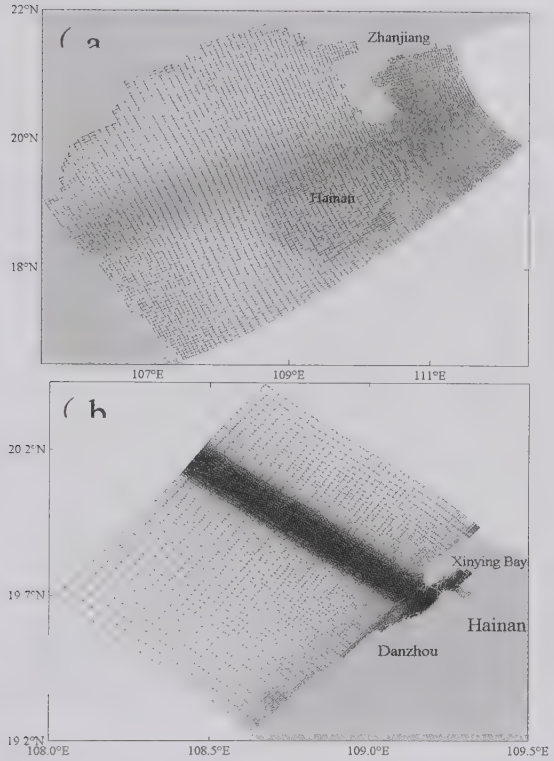

Fig. 2 Model grid (a: large scope; b: detailed scope)

4 Effects of the morphological change before and after the project and analysis of the cause

The Haihua Islands are arranged into 1#, 2# and 3# (see Fig. 5). The detailed model simulated the morphological change for 1 year after the construction of Haihua Islands in this paper. The detailed model simulated one year after the simulation for 15 days into the stable situation. Fig. 5 shows that the annual morphological change is small with about 5 cm/a, which mainly ranges the north of Haihua Islands near Xiaochan Reef and the land of Danzhou. The sea bed erodes slightly in the entry area of Yangpu channel, and the area among Haihua Islands is mainly eroded. The erosion amplitude exceeds 10 cm/a in the

area between 1# and 2# islands, but the scope is smaller. The revetment of Haihua Islands needs to build firm to prevent the tidal flow from eroding the dam.

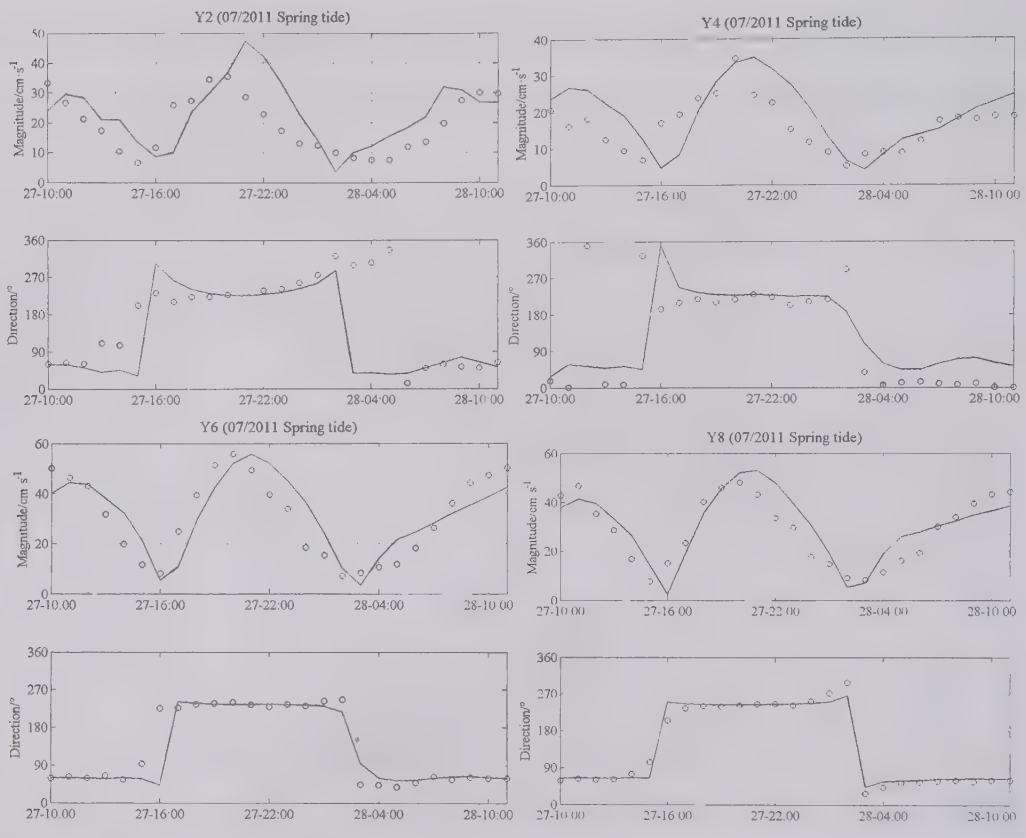

Fig. 3 Verification of the current velocity, and direction (circle is the observed, line is the simulated)

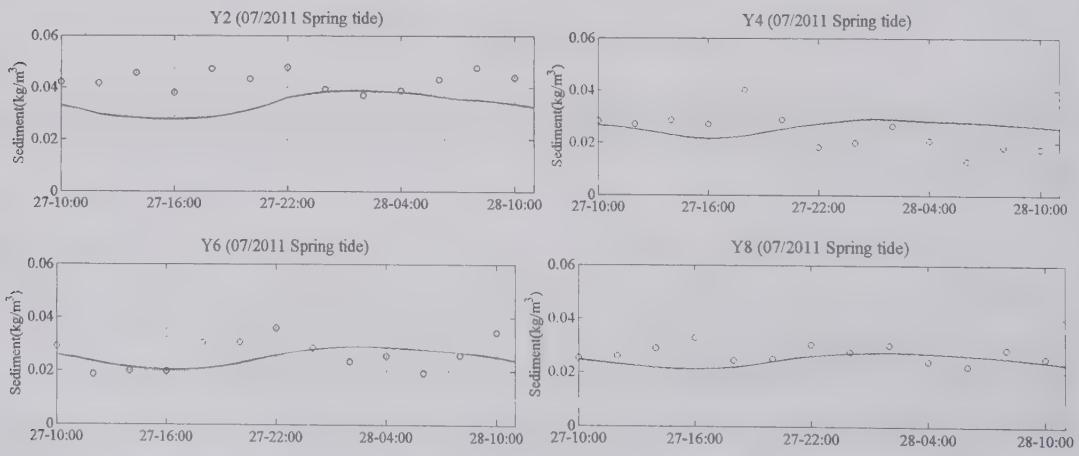

Fig. 4 Verification of suspended sediments (circle is the observed, line is the simulated)

It can be seen from Fig. 5, the variation of sea bed erosion and deposition is smaller after the construction of Haihua Islands. The dominant reason is the few sediment source, low SSC, small sediment erosion and deposition, and long stabilization of coast and sea bed in the study area. Flow velocity increase easily leads to the sea bed erosion, on the contrary, it leads to the sea bed deposition. As can be seen in Fig. 6, whether at flood maximum or at ebb maximum, the flow velocity increases with about 20 cm/s in the south of Xiaocha Reef. Therefore, the sea bed erodes both in the south of Xiaochan Reef and entry of Yangpu channel. The flow velocity increases with the amplitude of 30 cm/s at flood maximum and slightly increase at ebb maximum between 1# and 2# islands, which leads to the morphological erosion. The sea bed may deposit at the petals of the islands due to the reduction of the flow velocity.

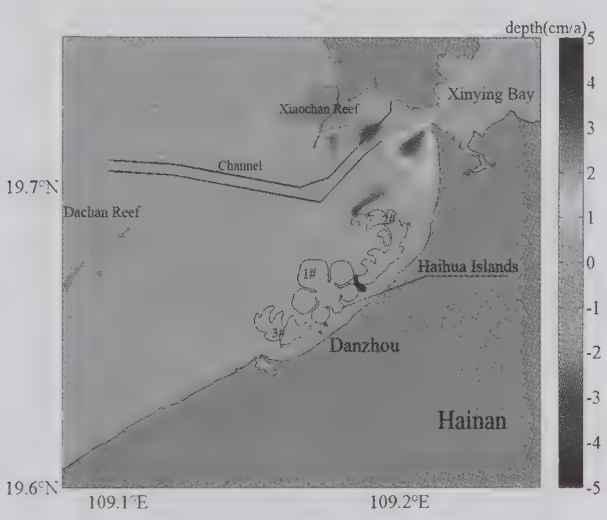

Fig. 5 Computed bed level increase (cm) in one year after the construction of Haihua Islands

(+ deposition, - erosion)

5 Conclusions

In this paper, Delft3D is used to set up a nested two dimensional hydrological and sediment model in the vertical average in Yangpu waters, Danzhou. The model is verified and its results indicate that the model can simulate flow velocity and sediment process, and the model can be used to simulate the sea bed morphological change due to the construction of Haihua Islands.

The measured data show that the low SSC results in the less erosion of sediments, therefore, the sea bed annual morphological change is small after the construction of the project. Flow velocity increase is the dominant reason of the sea bed erosion in the south

of Xiaochan Reef and entry of Yangpu channel by the analysis of the variation of flow velocity before and after the project.

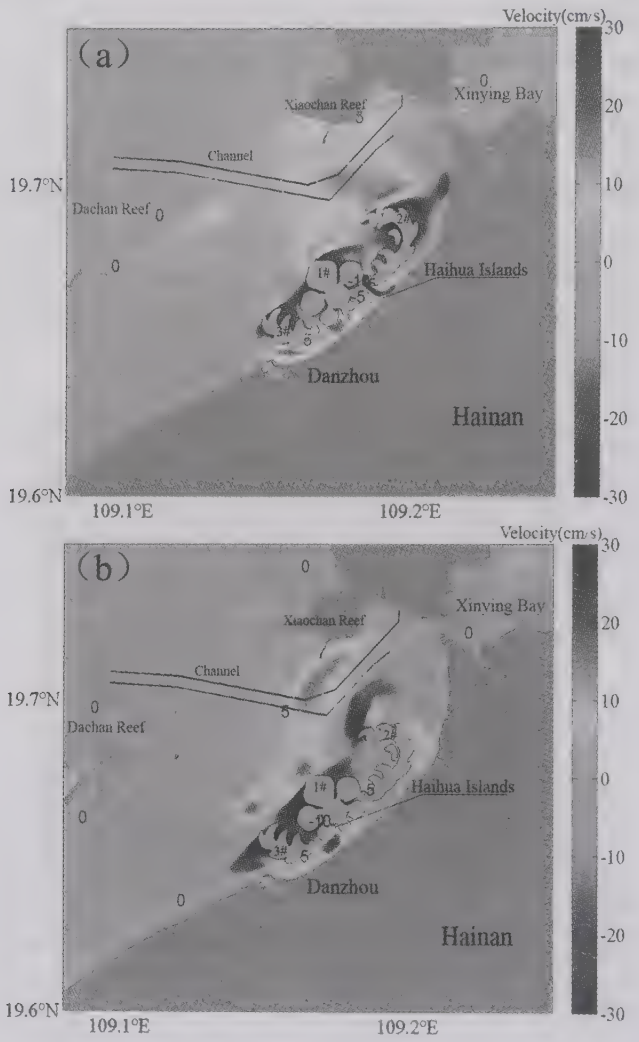

Fig. 6 Flow velocity change (cm/s) due to the construction of Haihua Islands

(a) maximum flood; (b) maximum ebb (+ increase, - decrease)

Yangpu waters is located in the west and north side of Hainan Island, and contrary to the direction of the normal typhoon. The effect of typhoon is mainly from the landing in the Hainan Island, Leizhou Peninsula or the tropical cyclones into the Beibu Gulf, however, the typhoon landing or entering into the Beibu Gulf has already weakened, so the area affected by typhoon is relatively small (South China Sea marine Engineering and Environment Institute, 2012). Therefore, the effects of typhoon to the morphological change is not simulated in this paper. The suspended sediment diffusion will cause the local sea bed deposition near the project due to the reclamation and overflow during the project

implementation. Because the time of construction is not long, the effects of reclamation and overflow is neglected.

References

[1] South China Sea Marine Engineering and Environment Institute. Report of regional marine use evaluation for Baima Haihua Islands in Danzhou, 2012.

[2] Lesser G R, Roelvink J A, Van kester J A T M, et al. Development and validation of a three-dimensional morphological model [J]. Coastal Engineering, 2004, 51: 883 - 915.

[3] Smit M W J, Reniers A J H M, Ruessink B G, et al. The morphological response of a nearshore double sandbar system to constant wave forcing [J]. Coastal Engineering, 2008, 55: 761 - 770.

[4] Hu K L, Ding P X, Wang Z B, et al. A 2D/3D hydrodynamic and sediment transport model for the Yangtze Estuary, China [J]. Journal of Marine Systems, 2009, 77: 114 - 136.

[5] Jeuken M C J L, Wang Z B. Impact of dredging and dumping on the stability of ebb-flood channel systems [J]. Coastal Engineering, 2010, 57: 553 - 566.

[6] Deltare. Delft3D-flow simulation of multi-dimensional hydrodynamic flows and transport phenomenon, including sediments. User Manual, 2011

[7] Xie D F, Wang Z B, Gao S, et al. Modeling the tidal channel morphodynamics in a macro-tidal embayment, Hangzhou Bay, China [J]. Continental Shelf Research, 2009, 29: 1 757 - 1 767.

海南儋州人工岛建设对海床冲淤影响数值模拟

英晓明，贾后磊，曹玲珑，谢 健

（国家海洋局 南海海洋工程勘察与环境研究院，广东 广州 510300）

摘 要：海南儋州海花岛填海规模较大，工程实施引起洋浦海域水动力环境改变，进而影响海床冲淤演变的变化。本文利用 Delft3D 数值模式建立了洋浦海域二维嵌套水沙数学模型，在对模型进行了验证基础上，模拟了海花岛实施前后海床冲淤演变和潮流变化。由于洋浦海域含沙量较低，附近沙源少，海花岛实施后附近海域海床淤积幅度较小。由于小铲礁南侧水流动力增加，小铲礁南侧和洋浦航道局部为冲刷。

关键词：海花岛；海床冲淤影响；数值模拟

Analysis on the land use and cover change in Tianjin Binhai New Area based on the remote sensing

WANG Feng[1, 2], LIU Shu-ming[2], LU Wen-hu[2], DU Qiong-wei[2], JIANG Wei-nan[2], LI Jia-rui[2]

1. *College of Oceanography and Environmental Science, Xiamen University, Xiamen* 361005, *Fujian province, China;*

2. *National Marine Data and Information Service, Tianjin* 300171, *China*

Abstract: This paper carries out quantitative analysis on the land use/cover (LU/C) change of Tianjin Binhai New Area in recent 10 years through using land use transition matrix from the three-stage LU/C classification maps of 2000, 2005 and 2010 drafted by means of the National Land Classification System of China based on Landsat TM satellite remote sensing image and the Tianjin Binhai New Area 1:50 000 relief maps. On this basis, the impact of such driving factors as the economy and population on LU/C is further analyzed. The results show that the area of the building land in Binhai New Area has increased significantly over the ten years, and the greenland, wetland, and shoals of high ecological value have been dramatically transformed into the building land and unused land for the development and construction, and the change is more significant in the later five years.

Keywords: Binhai New Area; remote sensing; land use and cover change; driving factors

The land is the most fundamental material basis that mankind relies on to survive and develop. As the research of global change develops further, it is gradually realized that the land use/cover change caused by human activities will eventually affect the survival and development of mankind themselves in return.

The ways to classify land are diversified, including the classification by utilization ways, by functions, and by resources, and comprehensive classification. The classification by land cover/land use (LC/LU) adopted in this paper is a new way of land classification as the remote sensing technology appears. Land classification by means of remote sensing features fast speed, high precision and wide scope, and fully embodies the timeliness, objectivity and wide range of monitoring. It has become a main trend in the research of LU/C to use remote sensing technology to observe the land, uncover the rules of its space change and establish driving force model of regional land use change for analysis. The

Received on Jun. 8, 2014

Corresponding author: wangfengbest@hotmail.com

research content involves in a series of significant issues such as protection and utilization of land resources, protection and control of ecological environment, sustainable development of social economy [1] [2].

Tianjin Binhai New Area is located at the eastern coast of Tianjin, including the former three administrative districts Tanggu, Han'gu and Dagang, and some areas of Dongli District and Jinnan District. It has been included in the strategic layout of the national overall development in the program of the "11th Five Year Plan" [3], with establishing the resource-saving and environment-friendly city development mode and building eco-city as its strategic goals. Therefore, currently, many government organizations, research departments, social groups and researchers are more and more concerned with the land use/cover change of this area. Meng Weiqing et al. carried out quantitative analysis on the landscape indices of the coastal wetlands in recent 30 years by means of the landscape ecology, and the result showed that the coastal wetlands were tending to be fragmented and artificialized [4]. Xu Dayong et al. conducted image extraction, analysis and prediction on the vegetation coverage change in this area based on normalized deferential vegetation index (NDVI) and came to the conclusion that the vegetation coverage in this area obviously showed a downward trend, which threatened the ecological safety [5]. The above mentioned studies could not fully reflect the land change in Binhai New Area in recent years, especially after it was put into the program of the "11th Five Year Plan" and the strategy of "Ten Battles" was carried out as their study objects were relatively long time ago; besides, their study targets were relatively unitary, so the change of various surface features and the situation of mutual transformation were not fully reflected.

Based on the previous experience, this study has made a three-phase (2000, 2005 and 2010) land use/cover classification picture of Binhai New Area based on Landsat TM remote sensing image, and carried out corresponding statistics and conducted quantitative description on Binhai New Area LU/CC in recent years by applying land use transition matrix. On this basis, it further analyzed the influence of such anthropic factors as economy and population on LU/CC in this area and specifically described the change and mutual transformation of land types and land area in a more comprehensive way to provide a theoretical foundation for environmental protection and sustainable development in Binhai New Area.

1 Research method and data source

1.1 Classification system of land use

LU/CC classification system, a primary prerequisite for studying LU/CC, not only

affects the expression of research result, but also decides the application field of the research data. Since 1970s, with the development of 3S and computer technologies, the classification system mainly for studying LU/CC has been rapidly developed. It focuses on the difference of land types for the investigation and research. Therefore, the size of scale, precision, decidability of remote sensing data, regional characteristics, practicability and systematicness should be considered in an all-round way [6].

In order to adapt it to the specific research purpose and degree, scholars in the world have built a lot of land classification systems from different perspectives; therefore, plenty of inconveniences are caused for summarizing, analyzing and sharing data due to the lack of uniform standard and bad compatibility. Until today, however, there is no "universal" land classification system that is extensively recognized around the world and fits all [7]. In view of this, this study comprehensively compares and analyzes the abovementioned classification system, develops a LU/CC two-grade classification system suitable for Tianjin Binhai New Area (Tab. 1) according to the land use and vegetation characteristics of this area based on the (tentative) National Standards of Land Classification, among which, Grade I includes the building land, moor, ocean, fresh waters, salt pan, vegetation and unused land.

Tab. 1 Tianjin Binhai New Area LU/C Change Classification System

Grade I Classification	Grade II Classification
Building land	Urban-rural resident area, industrial, mine and factory land, land for traffic use, etc.
Moor	Area with accumulated water and mud, wetland, et al.
Ocean	
Fresh waters	Lake, river, reservoir
Shoal	Rocky beach, sand beach, mud bank
Salt pan	Salt pan, pit-pond, culture pond, etc.
Vegetation	Grassland, woodland, farmland, etc.
Unused land	Reclaimed land from sea, Gobi, saline-alkali soil, bare land

1.2 Processing of remote sensing data

American Landsat sensor TM/ETM data are used in the study. Data of the three years 2000, 2005 and 2010 are selected and compared for the study.

Binhai New Area boundary vector graph is obtained by using Tianjin Binhai New Area 1:50 000 topographic map. Geometric precision correction is conducted on the image. Image enhancements such as histogram equalization, image fusion and thin cloud removal

are applied to the images with relatively bad contrast. ENVI software is used to clip the original remote sensing image.

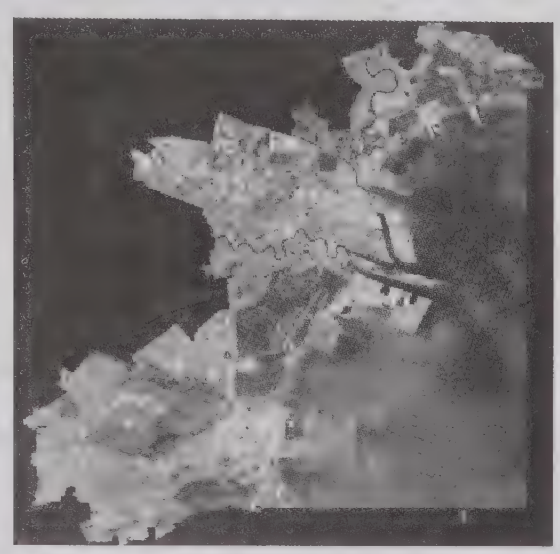

Fig. 1 Clipped scope of Binhai New Area

In terms of image classification, this study carries out automatic classification with computer by using the method combining supervised classification with texture-based object-oriented fuzzy classification. In order to protect the accuracy of extracting information of various surface features, field survey is conducted for the verification; besides, 1:50 000 topographic map and Google Earth image of corresponding period are used as the reference for artificial visual interpretation so that the data can be correct. Finally, the final classification image data of the years 2000, 2005 and 2010 are obtained (Fig. 2).

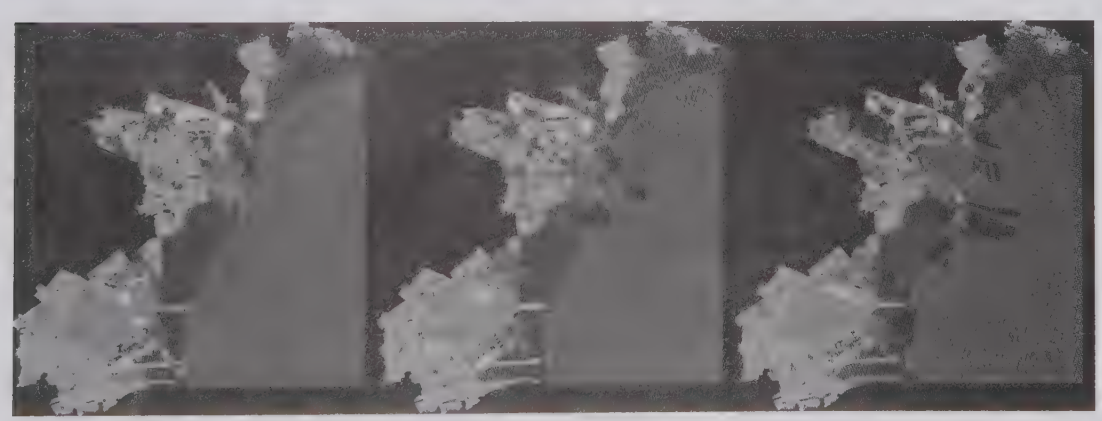

Fig. 2 Land use classification data of Binhai New Area in 2000, 2005 and 2010 (from left to right)

2 Statistical analysis of LU/C change

2.1 Analysis on overall quantity change and characteristics of Binhai New Area LU/C

2.1.1 Range of land use change

The LU/C change includes the change of area, space and quality of different types of lands. The change of area is firstly reflected in the total quantity of different types of land; through analyzing the change of the total quantity of various land use types, the change of land use structure and the overall trend of the change can be understood [8].

The result shown in Tab. 2 and Fig. 3 is obtained from statistical analysis on the land use classification data (Fig. 2) of Binhai New Area of the three phases, respectively, by using the abovementioned data.

The result shows that during the 10 years, the quantity change of land use types in Binhai New Area features sharp increase of building land and unused land, and sharp decrease of vegetation and ocean. The increases of building land and unused land are 335.113 km^2 and 202.417 m^2, respectively; while the decreases of vegetation and ocean area are as high as 238.859 km^2 and 139.542 km^2, respectively. With the implementation of multiple policies and the acceleration of developing process, the area change from 2005 to 2010 is obviously higher than that from 2000 to 2005.

Tab. 2 LU/C area change of various types of Binhai New Area in recent 10 years (unit: km^2)

	2000	2005	2010	Change 2000-2010	Annual change rate
Vegetation	957.550	893.456	718.691	-238.859	-2.49%
Salt pan	726.565	757.924	640.302	-86.263	-1.19%
Building land	231.764	283.902	566.877	335.113	14.46%
Fresh waters	113.926	125.436	108.591	-5.335	-0.47%
Moor	235.541	206.242	211.453	-24.088	-1.02%
Unused land	37.448	76.178	239.865	202.417	54.05%
Ocean	1947.599	1925.247	1808.057	-139.542	-0.72%
Shoal	69.848	52.813	27.590	-42.258	-6.05%
Total area	4320.241	4321.198	4321.426		

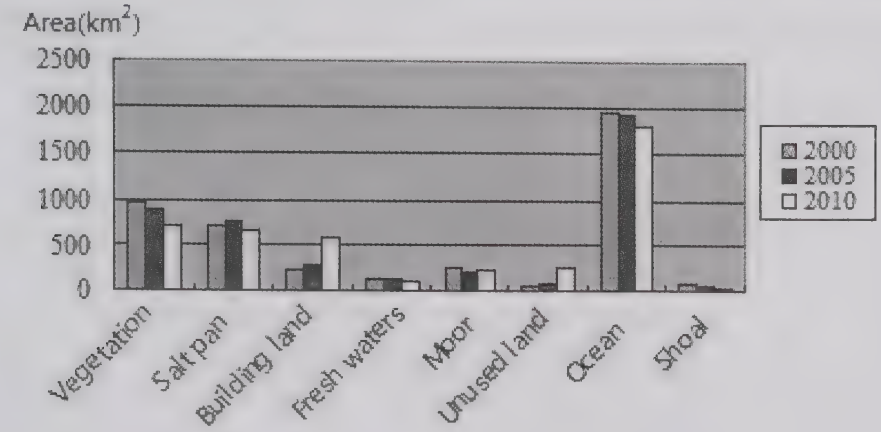

Fig. 3 Statistics of area change of various types of LC/LC in the 10 years

2.1.2 Dynamic degree of LU/CC

The dynamic degree of land use types refers to the quantity changes of certain type of land use within a given period of time in some research zone, which quantitatively describes the changing speed of land resource quantity and plays an active role in predicting the trend of land use change [9].

Its expression is as follows:

$$K = \frac{U_b - U_a}{U_a} \times \frac{1}{T} \times 100\%$$

where U_a and U_b are the quantity of certain types of lands at the beginning and at the end of the research period, respectively; T is the research duration; when T is assumed as one year, the dynamic degree of land use types, the value of K is the annual change rate of such land type in the research zone.

It can be known from Tab. 2 that the area of unused land and building land in Tianjin Binhai New Area has increased at a relatively high speed, with the annual change rate as high as 54.05% and 14.46%, respectively. The area of such land types as vegetation, salt pan, fresh waters, moor, ocean and shoal has also been reduced at different speeds, among which the relatively obvious annual change rates are -6.05% for the shoal and -2.49% for the vegetation. Besides, in spite of the relatively small change rate of ocean, but the final result should consider its change degree as its base number of area is relatively large.

The abovementioned two methods and results can relatively well reflect the quantity and change of LU/CC of Binhai New Area, but overlook the innate process of land use change. Therefore, other research methods are needed for further description.

2.2 Land use transition matrix

Under certain conditions, the mutual transformations between land use types have the characteristics of Markov Random Process; therefore, the model of Markov Transition Matrix can be used for further description. Markov chain comes from quantitative description of system state and state transition in the system analysis[10], which is a special random motion process characterized as "memoryless". It reflects a series of process for a semi-stable system to transit from the time T_1 to the time T_2; such transition requires that the state of T_2 is only related to that of T_1 [11].

Usually, the key for the application of Markov model to the land type transition lies in the determination of transition probability matrix. Transition matrix can show the dynamic change of types of certain LU/C from one year to another, namely, the ratio of certain type that remains unchanged, and the number transformed to other types and the ratio of transforming to other types [12].

Tab. 3 Land use transition matrix model

		T_2					
		A_1	A_2	$\cdots$	A_n	P_{i+}	Decrease
T_1	A_1	P_{11}	P_{12}	$\cdots$	P_{1n}	P_{1+}	$P_{1+}-P_{11}$
	A_2	P_{21}	P_{22}	$\cdots$	P_{2n}	P_{2+}	$P_{2+}-P_{22}$
	$\vdots$	$\vdots$	$\vdots$	$\ddots$	$\vdots$	$\vdots$	$\vdots$
	A_n	P_{n1}	P_{n2}	$\cdots$	P_{nn}	P_{n+}	$P_{n+}-P_{nn}$
P_{+j}		P_{+1}	P_{+2}	$\cdots$	P_{+n}	1	
Increase		$P_{+1}-P_{11}$	$P_{+2}-P_{22}$	$\cdots$	$P_{+n}-P_{nm}$		

In Tab. 3, the items in the row stand for the land use type at the time T_1 and ones in the column stand for the type at the time T_2. P_{ij} stands for the percentage of the area of land type j transformed from land type i during the period from T_1 to T_2; P_{ii} stands for the percentage of area of land use type i that remains unchanged during the period from T_1 to

T_2. P_{i+} stands for the percentage of land type i in the total area at the time of T_1. P_{+j} stands for the percentage of land type j in the total area at the time T_2. $P_{i+} - P_{ii}$ is the percentage of area reduction of land type i during T_1 - T_2 period; $P_{+j} - P_{jj}$ is the percentage of area increase of land type j during T_1 - T_2 period[13].

Tab. 4 Land type use change transition matrix (2000-2005)

		2000							
		Greenland	Salt pan	Building land	Fresh waters	Moor	Unused land	Ocean	Shoal
2005	Greenland	80.1219	9.1137	12.0071	10.6554	6.2471	9.8111	0.0016	0.4710
	Salt pan	8.9797	81.5518	7.1809	4.3108	11.6268	44.6141	0.0466	18.0237
	Building land	6.4986	3.1853	77.9166	1.0118	1.7802	23.9999	0.0384	4.0063
	Fresh waters	1.5100	1.3515	0.2644	71.1277	8.1790	0.0523	0.0020	0.2323
	Moor	1.9667	0.2888	0.2199	11.6211	72.1598	4.2617	0	0
	Unused land	0.7820	4.0762	2.1962	0.4274	0	16.1277	1.0123	11.0848
	Ocean	0	0.0893	0.0706	0.2394	0	0	98.4833	7.3854
	Shoal	0	0.3100	0.1316	0.5804	0	1.1332	0.4160	58.7965
	Class Changes	19.8781	18.4482	22.0834	28.8723	27.8402	83.8723	1.5167	41.2035
	Image Difference	-6.6936	4.3161	22.4959	10.1033	-12.4393	103.4248	-1.1477	-24.3887

Tab. 5 Land type use change transition matrix (2005-2010)

		2005							
		Greenland	Salt pan	Building land	Fresh waters	Moor	Unused land	Ocean	Shoal
2010	Greenland	76.5995	2.1754	2.0552	1.8813	3.0570	4.1168	0.0006	0.0043
	Salt pan	2.5330	78.3102	1.3645	7.6295	0.0977	2.6128	0.1798	9.5457
	Building land	17.5097	8.8070	95.5719	1.4151	0.4866	69.6897	0.6708	6.7679
	Fresh waters	0.3006	0.4740	0.0369	71.1817	5.8558	0.0018	0.0330	0.3937
	Moor	0.1089	0.0007	0.0002	17.6014	90.5029	0	0.0250	2.3875
	Unused land	2.9286	9.8046	0.9478	0.1921	0	23.2264	5.1731	35.9239
	Ocean	0.0039	0.0006	0.0193	0.0927	0	0.3527	93.7328	5.6628
	Shoal	0.0008	0.4277	0.0042	0.0061	0	0	0.1849	39.3143
	Class Changes	23.4005	21.6898	4.4281	28.8182	9.4971	76.7737	6.2672	60.6857
	Image Difference	-19.5605	-15.5189	99.6736	-13.4290	2.5269	214.875	-6.0870	-47.7591

The results can be concluded from the transition matrix.

During the two periods, shoal and unused land of relatively large ratio are transited and the transition degree of other land types is relatively small.

From 2000 to 2005, the transition ratios of the unused land area and shoal area are as high as 83.872 3% and 41.203 5%. Among them, the main ground features of unused land are salt pan and building land while the shoal of relatively large ratio is transformed to the unused land and salt pan.

It is more obvious from 2005 to 2010 that 35.923 9% of the total area of shoal was transformed to the unused land, with total transformation rate as high as 60.685 7%; 69.689 7% of unused land was transformed into the building land, with total transformation rate of 76.773 7%; besides, 17.509 7% of greenland was transformed into the building land.

The above results appropriately match the implementation of projects, such as regional construction, community demolition and relocation, and reclaiming lands from the sea in Binhai New Area, and coincide with the construction goal of prioritized projects in the "Ten Battle" strategy.

3 Discussion

The dynamic change of LU/C is a change of land use purpose and pattern under the action of various driving forces. There are a lot of driving factors affecting land use change, which can be generally divided into natural factors and anthropic factors. Natural factors refer to the tellurian physical factors exerting certain degree of influence on the land use management and pattern, mainly including climate, hydrology, terrain, soil, vegetation and natural disaster; anthropic factors include such aspects as society, economy, politics, culture, and technical progress, which are mutually connected, interacted and affected[14]. From a relatively short period of time, the change of the frequency and speed of natural elements is blunt and slow compared with the complex and rapid change of social and economic elements. The LU/C change of Binhai New Area in recent 10 years is mainly caused by human activities. Therefore, it is more important to analyze the anthropic driving factors of land use.

3.1 Economic factors

Economic factors, including economic structure and development level, industrial and transportation conditions, urban development and market condition, commerce and trade development, are the fundamental conditions deciding the development and utilization of land. The features of the changes of these economic factors directly affect the direction, structure, scale, layout and profit of the development and utilization [15].

In recent 10 years, Binhai New Area has kept continuous and rapid development since this area has deepened the reform, expanded opening-up, taken initiative to keep up with the international economy, improved investment conditions and worked hard to create a first-rate investment environment. In the 10 years, the gross output of the primary industry in Tianjin Binhai New Area has an average annual growth rate of 5.72%, the growth rate of 79.52% for the secondary industry and 76.79% for the tertiary industry. The

total output value in Binhai New Area has increased from 57.174 billion Yuan in 2000 to 503.011 billion Yuan in 2010 [16] (Tab. 6).

Tab. 6 Statistics of total output value of Binhai New Area (100 million Yuan)

Year	New Area subtotal	Primary industry	Secondary industry	Tertiary industry	Percentage in those of the whole city / %
2000	571.74	5.20	383.45	183.09	33.6
2001	685.32	5.67	454.22	225.43	35.7
2002	862.45	6.09	576.06	280.30	40.1
2003	1046.30	7.30	697.66	341.34	40.6
2004	1323.26	7.91	878.85	436.50	42.5
2005	1633.93	7.15	1092.55	534.22	41.8
2006	1983.63	7.25	1354.40	621.98	44.4
2007	2414.26	6.78	1669.86	737.63	46.0
2008	3349.99	7.02	2304.37	1038.60	49.9
2009	3810.67	7.43	2569.87	1233.37	50.7
2010	5030.11	8.17	3432.81	1589.12	54.5
Average annual growth rate / %	77.98	5.72	79.52	76.79	

In Binhai New Area, the change of industrial structure has caused a re-distribution of land resources among industries, which consequently causes the change of land use structure. The ratio of primary industry tends to go down and the secondary and tertiary industries tend to go up. Driven by the mechanism of economic interests, land use is constantly transformed from agricultural land of low profit to non-agricultural land, showing an unbalanced situation. Meanwhile, with the development of social economy and the increase of total output value, human's ability to develop and use land has been improved, which provides a basic condition for the further and more extensive development and utilization, promoting the development of various wastelands and transformation of farmland and woodland of the middle or low production.

3.2 Factor of population

As a unique factor, population is the most important element in the anthropic factor for LU/C change, also one of most vigorous driving forces for the LU/C change. Firstly, the quantity of population directly affects the LU/C change; secondly, people try to meet their demands for the living environment by changing the type and structure of land use/cover to reinforce the intervention degree on the land, this natural complex. Therefore, in the study of LU/C change, the factor of population is often regarded as a comprehensive

parameter reflecting the contribution of human activities to the change of land use/land cover [17].

In 2010, the permanent resident population in Binhai New Area accounts for 2.482 1 million, which is 1.293 1 million more than that 10 years ago, with the increasing rate of 108.75%, and the average annual growth rate is 7.64% [18]. Among the permanent resident population, the areas with relatively concentrated population include Tanggu with 850 974 persons, accounting for 34.28% of the total population of this area, Han'gu with 217 107, accounting for 8.75%; and Dagang with 523 144, occupying 21.08%.

If the land use in Binhai New Area is compared to an open system, population will be the organizers and participants in this systematic structure, and the consumers of the output product of this system as well. In other words, people accelerated the land development in Binhai New Area with growing utilization rate by adjusting and organizing the system structure of land use by means of production technology and activity patterns. Meanwhile, as participants, they also occupy the building land –land of certain area as a place for living. And finally, as consumers, people consume the product from land use system and increase pressure on the productivity of ecological system of land. Therefore, the growth of population leads to the growth of building land and causes higher production pressure on the farmland, woodland and greenland that are continuously diminishing [19].

3.3 Policy implementation and reclaiming land from sea

The guidance of government policy will play a key role in the change of land use featuring regional scale [20]. Since the program of the "11th Five Year Plan", Tianjin Binhai New Area has become another potential economic growth pole besides Shenzhen Special Economic Zone and Pudong New Area. Furthermore, the government has deployed the implementation of "Ten Battles" development strategy in 2009. However, over-emphasis on the economic development in making policies for the land use and development and overlook on the environmental construction to some degree have caused a low level of sustainable land use in Binhai New Area and the land use was not truly transformed from economy-dominated development pattern to sustainable development pattern[21]. Eventually, the area of such land types as vegetation, wetland and shoal favorable for maintaining ecological stability has sharply diminished and the area of the building land used for economic development dramatically increased. Developing towards this direction, it will definitely limit the sustainable development of the environment, economy and society in Binhai New Area in future.

The project of reclaiming land from the sea in Tianjin Binhai New Area is the largest project of land reclamation from sea in China, with a total plan area of more than 200 km^2,

including subprojects such as Dongjiang port area, port industrial zone, port property zone and south port industrial zone. This project alleviated the shortage of land for industrial and residential use to some degree, met the demand of economic development and population growth on land reserves, and also increased the curve and length of the coastal line of the above mentioned areas [22]. However, the implementation of this project caused the area reduction and aggravated the fragmentation of natural land types such as shoal and wetland, which posed a severe challenge to the ecological environment of Binhai New Area.

4 Conclusions

There are a lot of methods to extract LU/C types from remote sensing image. This study chooses to use automatic classification with the computer by using the method combining supervised classification with texture-based object-oriented fuzzy classification, and then artificial visual interpretation is carried out to get classified images. Finally, the area, speed and location of land use/cover change of various types in Binhai New Area are known from the analysis by means of statistical calculation and land use transition matrix.

Economic development, population growth, policy implementation and land reclamation from sea have all exerted influence to some degree on the LU/C change in Binhai New Area. The area of building land has sharply increased and the land types of relatively higher ecological value such as greenland, wetland and shoal are dramatically diminished.

In future, correlation analysis between LU/C change and influential factors such as economy and population in the research zone can be carried out to give more clear interpretation and prediction by means of establishing mathematical model. Also, assessment can be conducted on the sustainable use of land for establishing a land sustainability assessment index system and scientific and rational assessment system fit for the research zone by combining the process of change.

References

[1] Gong Wen, Zhou Jinsheng. Analysis on the Role of Remote Sensing Monitoring Technology in Land Use Supervision [J]. Natural Resource Economics of China, 2011, (5): 49 - 50.

[2] Liu Jun. Study on Land Use/Cover Change of Recession Belt of Three Gorges Reservoir Based on 3S Technology [D]. Chongqing: Chongqing Jiaotong University, 2010.

[3] Wu Jiali, Li Hongjun, Yuan Haozheng. Innovative Study of Overall Planning of Land Use in Tianjin

Binhai New Area [A]. City, 2011, (11): 52 - 55.

[4] Meng Weiqing, Li Hongyuan, Hao Cui, et al. Analysis of Remote Sensing Monitoring on Wetland Landscape Pattern of Tianjin Binhai New Area in Recent 30 Years [J]. Geo-Information Science, 2010, (3): 436 - 443.

[5] Xu Dayong, Zhang Tao, Sun Yichao, et al. Study of Vegetation Cover Degree Change and Prediction of Tianjin Binhai New Area Based on NDVI [J] Ecological Economics, 2010, (12): 45 - 50.

[6] Zhao Gengxing, Li Yuhuan, Xu Chunda. Study of Remote Sensing and GIS-Supported Dynamic Monitoring of Land Use – A case study Kenli County in Yellow River Delta [J]. Chinese Journal of Applied Ecology, 2000, 11(4): 573 - 576.

[7] Zhang Jinghua, Feng Zhiming, Jiang Luguang. Study Progress of Land Use/Land Cover Classification System [J]. Resources Science, 2011, 33 (6): 1 195 - 1 203.

[8] Zhu Huiyi, Li Xiubing, Analysis of Time-Space Change of Land Use in Bohai Rim [J], Journal of Geographical Sciences, 2001, 56 (3): 253-260.

[9] Wang Xiulan, Bao Yuhai. Discussion on Study Method of Dynamic Change of Land Use [J]. Progress in Geology, 1999, 18 (1): 81 - 87.

[10] Xu Lan, Zhao Yi. Prediction on Change of Land Use Pattern in Dongling District by Markov Process [J]. Chinese Journal of Apply Ecology, 1993, 4 (3): 272 - 277.

[11] Wang Siyuan, Liu Jiyuan. Land Use Pattern and Evolution of China in Recent 10 Years [J]. Journal of Geographical Sciences, 2002, 57 (5): 523 - 530.

[12] Chen Siqing, Liu Jiyuan, Zhuang Dafang, et al. Land Cover Change in Xilin River Valley based on Landsat TM/ETM data [J]. Journal of Geographical Sciences, 2003, 5 (1): 45 - 52.

[13] Liu Rui, Zhu Daolin. Discussion on Data Digging Method of Land Use Change Based on Transition Matrix [J]. Resources Sciences, 2010, (8): 1 544 - 1 550.

[14] Liang Changxiu. Beijing Land Use/Cover Change Study Based on RS and GIS [D]. Beijing: Beijing Forestry University, 2009.

[15] Wu Chuanjun, Guo Huancheng. Land Use of China [M]. Beijing: Science Press, 1994.

[16] Zong Guoying, Du Xiping. Statistical Book of Tianjin Binhai New Area 2011 [M]. Beijing: China Statistical Publishing House, 2011.

[17] Wang Xiulan, Analysis of Population Factor in Land Use/Land Cover Change [J]. Resources Science, 2000, 22 (3): 39 - 42.

[18] Tianjin Statistic Bureau. Report of Main Data of the Sixth Nationwide Census of Tianjin 2010, [EB/OL]. 2011-4-29. http://www.stats-tj.gov.cn/Article/tjgb/pcgb/201105/17511.html

[19] Qin Minzhou. Theory and Practice of Land Use and Sustained Development [M]. Xi'an, Xi'an Map Press, 1998.

[20] Liu Jiyuan, Zhang Zengxiang. Analysis of Space Pattern of Recent Land Use Change in China [J], Science in China: Edition D, 2002, 32 (12): 1 031 - 1 040.

[21] Cao Ying. Assessment of Sustainable Land Use and Study of Regional Development Countermeasures of Tianjin Binhai New Area [D]. Tianjin: Tianjin Normal University, 2013.

[22] Zhao Yingjie, Liu Xianbing, Liu Aizhen, et al. Discussion on the Rationality of Sea Use Manner in South Port Industrial Zone of Tianjin [J]. China Water Transport, 2011, (5): 49 - 52.

基于遥感的天津滨海新区土地利用/覆盖变化分析

王 丰[1,2]，刘书明[2]，卢文虎[2]，杜琼玮[2]，姜伟男[2]，李佳芮[2]

（1. 厦门大学海洋与地球学院，福建 厦门 361005；2. 国家海洋信息中心，天津 300171）

摘 要：采用全国土地分类系统，基于 Landsat 卫星 TM 遥感影像与天津滨海新区 1:50,000 地形图，进行相应数据处理，编制出 2000 年、2005 年、2010 年三期滨海新区土地利用/覆盖分类图，并运用土地利用转移矩阵对近 10 年来天津滨海新区土地利用/覆盖变化进行定量分析。在此基础上，进一步分析了经济、人口等驱动因子对土地利用/土地覆盖的影响。结果表明：十年间，滨海新区的建筑用地面积增加显著，而绿地、湿地、滩涂等高生态价值的土地向建筑用地、未利用地等开发建设用地大幅度转化，后五年变化尤为显著。

关键词：滨海新区；遥感；土地利用/覆盖变化(LUCC)；驱动因子

Analysis of the integrated test and evaluation methods of tidal current energy generating devices in the offshore testing site

GUO Wen-rui[1], ZHU Yong-qiang[1], YE Qing[1], LI Xue-lin[2], WANG Xin[2], DUAN Chun-ming[3*]

1. *Institute of electric and electronic engineering, North China Electric Power University, Beijing* 102206, *China;*

2. *National Marine Technology Center, Tianjin* 300112, *China;*

3. *Power Economic Research Institute, State Grid Jibei Electric Power Company Limited, Beijing* 100045, *China;*

Abstract: Actual sea condition testing and inspection and evaluation method research are carried out for tidal energy devices to provide scientific and effective technical support for the ocean high-tech achievement transformation and marine renewable energy development. By analyzing three core indicators, including the power output characteristics of the tidal current device, the generating capacity, energy conversion efficiency, proposed the test contents and evaluation methods of indicators are proposed in this paper; and based on the research of wind farms, power quality testing and assessment methods of offshore tidal energy device are proposed; given the security access to the test contents of tidal current energy device, tidal current energy device running conditions in the testing ground are comprehensively assessed.

Keywords: testing ground; tidal current energy; generating device; integrated test; evaluation method

1 Introduction

China has long coastline with rich marine resources, well-developed eastern coastal areas, intensive electric loads and a strong power grid, which make favorable conditions for the utilization and development of large-scale marine power. From the perspective of energy demand in China, Xiong [1] analyzed the main problems and positive conditions in the utilization and development of marine energy of China, and proposed directions for the development in the future. After an elaborate introduction of the development of marine energy and its power generation technology in China, Zhu [2] and You [3] pointed out that China's technology of tidal current energy utilization still stayed in the status of

Received on Jul. 20, 2014

*Corresponding author: ruoxiren1988@126.com

engineering prototype machine testing and demonstration experiment, which was far from the large-scale industrialized application.

Beginning with the first test site Nissum Broads which located in the western coastline of Denmark and was put into operation in 2003[4], more than 10 offshore experiment and test sites have been constructed around the world until now. In 2006, European Marine Energy Center (EMEC) finished the construction of marine energy test site in Orkney, Scotland [5]. Afterwards, Scotland, Denmark and the U.S. set up similar public real sea state grid connection test platform [6]. Real sea state grid connection test is the key step for marine energy devices to transform from engineering prototype machine to large-scale industrialized application. Li [7] pointed out that in the early stage of ocean energy tests of devices in real sea state, long term investigations into the status of ocean energy resources, hydrologic meteorological environment and seafloor sediments in test waters were needed. Afterwards, seabed infrastructure construction, seabed cable casting and offshore engineering such as grid connection should also be carried out. The preparation stated above consumes a large amount of manpower and resources, which will greatly enlarge experimental cost and test duration. Offshore experiment and test sites and the comprehensive test and evaluation system of tidal current energy are the most effective solutions to solve the aforementioned problems.

The situation that no ocean energy test experiment and test site has been constructed in China allows of no delay to perform construction of test sites and theoretical research of comprehensive test and evaluation system. In 2010, the State Oceanic Administration, together with the Ministry of Finance, formulated and promulgated 'The Interim Measures for Marine Renewable Energy Special Funds Management' and established Application Guidelines of Marine Renewable Energy Special Funds in 2010. Various supporting projects are carried out actively and continuously.

Zhang [8] proposed a general framework for the utilization and development of tidal current energy, including investigation and evaluation of tidal current resources and environment [9], power generation devices of tidal current energy, construction and operation of tidal current energy test site, et al.

National Marine Technology [10] presented an integrated content of test system for tidal current power generation devices used in offshore test site, which fulfilled the requirements of the following aspects of tidal energy generation devices including conversion efficiency testing in real sea state, environmental adaptability analysis, reliability justification and grid-connection testing. The aforementioned test system includes oceanic environment observation subsystem, data integration and management

subsystem, comprehensive test and evaluation subsystem and monitoring system, et al. This paper focuses on the three core indices, including tidal current devices including power output characteristics, annual energy output, energy conversion efficiency, and test and evaluation of power quality, and test method for the access of tidal current devices.

2 Measurement methods of power output characteristics of tidal current devices

During the test and evaluation process of the power output characteristics of tidal current devices, measurement of current velocity at the front of the generation devices and the power output of the devices should be conducted synchronously. Current velocity data and power output data are measured once a minute according to the measurement method, and are collected in the same time period. When the current velocity of a tidal current device is below the lowest designed operating velocity or above the largest designed operating velocity, the tidal current device stops working; the unidirectional tidal current power generation device stops running during the current reversion, and therefore no power output during the cut-out of the tidal current device; the aforementioned current data should be sifted and eliminated before the data analysis and processing.

Data points acquired are separated into different groups called analysis sections before power characteristics are analyzed. Grouping is based on the current velocities in the data points. Data points allocated in a group meet the conditions that current velocities are above or equal to certain velocity, and are below other current velocity. For example, current velocity at moment *k* is allocated to section *m*, which can be described as $v_{ck} \in [v_{cm}, v_{c(m+1)})$, where the beginning of a section is defined by the lower limit current velocity v_{cm}, and the terminal of a section is defined by the upper limit current velocity $v_{c(m+1)}$. The section width of each analysis section is defined by the difference of the beginning and the terminal of the analysis section, as the formula $L_m = v_{c(m+1)} - v_{cm}$. Scopes of possible current velocities are divided into several sections. The terminal of one section is the beginning of the section behind, which ensures that each valid data point can be allocated to only one section.

The representative data points of each analysis section are the arithmetic average of current velocities v_{cn} and the electric power values p_{gn} of the data points in that section, which are represented by $\overline{v}_{cn}$ and $\overline{p}_{gn}$ respectively. The curve of power output characteristics of devices is acquired by numerical fitting of the representative data points.

The width of the analysis section and the number of data points in the section should be carefully selected, which determines the validity of the representative points, and

constitutes the basis of the fitting of the curve of power characteristics. The optimal section width selection related to the rated operating current velocity scope of devices should be determined by the comparison and analysis of magnitude of errors generated by different section width selections.

3 Measurement and evaluation method of energy conversion efficiency

Measurement and evaluation method of energy conversion efficiency in tidal current energy devices is designed to evaluate the utilization of marine energy in the operation of tidal current energy devices, which can be seen as reliable reference for the development and construction of tidal current energy devices. Relevant parameters of power generation system in real sea dynamic environment and power output of generators are focal points in the measurement of the test site, which are used to verify and revise the calculations of the evaluation model, and to set up calculation method for the evaluation of conversion efficiency.

3.1 Research of measurement and evaluation method of power inputs

Two aspects of measurement of power inputs should be considered as follows. Firstly, owing to the gap between measurement devices and power generation devices, measurement data do not synchronize with the data in current field surrounding the device. Secondly, measurement devices and current field surrounding the device interact, and devices also exert influences on the surrounding current field in operation. Research of evaluation method mainly includes calculation method for static performance evaluation considering tidal current energy devices and mathematical model for dynamic performance evaluation.

Given the current velocity at the measurement point at moment k, v_{ck}, current power can be found as the following:[11]

$$p_{lk} = \frac{1}{t}\int_0^t \frac{1}{2}\rho {v_{ck}}^3(t) \times A \times 10^{-3} dt \tag{1}$$

where ρ is the current density; t is the time span corresponding to the width of ananalysis section divided, L_n; A is the vane area, which is also a function of diameter of water wheel, and can be found as $A=hD^2$, where h is determined by the type of the vane wheel, and $h=\pi/4$ is chosen for the horizontal axis paddle type vane.

Using the discrete magnitude, current power can be calculated as follows:

$$p_{lk} = \frac{1}{n\Delta t}\sum_{k=1}^{n}\frac{1}{2}\rho v_{ck}\cdot A\cdot\Delta t = \frac{1}{n}\sum_{k=1}^{n}\frac{1}{2}\rho v_{ck}\cdot A \tag{2}$$

where Δt is the sampling period and n is the total sampling time.

3.1.1 Static performance evaluation method

According to the main performance index of measurement devices such as vertical current velocity distribution, electricity capture area of power generation devices and position, available power generated by capture area of power generation devices can be calculated and further used for the evaluation purpose.

3.1.2 Dynamic performance evaluation method

Fluid and solid coupled calculation method and model of marine dynamic environment and marine energy devices are built with several coupled marine dynamic factors such as tidal current, wave, wind, etc., and on the basis of N-S function of incompressible viscous fluid. Relevance and real time transfer characteristics of data are researched and test methods of instantaneous and short time corresponding characteristics are realized. Meanwhile, tidal current energy of small region adjacent to berths is calculated using offshore numerical model, and tests of efficiency of the two-stage conversion from energy in site region to the actual power input of devices and from actual power input to the power output of the device are realized.

3.2 Measurement of power output and analysis of overall efficiency

At the same time period, principal axis power output of hydraulic turbine can be calculated as the following [12]:

$$p_{jk} = \frac{1}{t}\int_0^t M\times\omega\times10^{-3}dt = \frac{2\pi}{t}\int_0^t M\times r\times10^{-3}dt \tag{3}$$

where M is the instantaneous torque; ω is the rotational angular speed; r is the instantaneous rotational speed. To be received by data acquisition system, signals of torque and rotational speed should be sampled. Power output expressed by discrete magnitude can be found with the following formula:

$$p_{jk} = \frac{1}{n\Delta t}\sum_{k=1}^{n}M_k\cdot n_k\cdot\Delta t \tag{4}$$

where M_k and n_k are sampling values of instantaneous torque and rotational speed at moment k respectively.

Electric power output of tidal current devices at moment *k* can be found as the following:

$$p_{gk} = \frac{1}{t}\int_0^t u(t)\cdot i(t)dt \tag{5}$$

where $u(t)$ and $i(t)$ are instantaneous values of voltage and current output at the terminal of the generator at moment *k* respectively. Likewise, to be received by data acquisition system, voltage and current signals should be sampled. Electric power expressed by discrete magnitude can be calculated as the following:

$$p_{gk} = \frac{1}{n\Delta t}\sum_{k=1}^{n} u_k \cdot i_k \cdot \Delta t = \frac{1}{n}\sum_{k=1}^{n} u_k \cdot i_k \tag{6}$$

where u_k and i_k are sampling values of instantaneous voltage and currents at moment *k*.

Energy availability, C_p, can be found with the following formula:

$$C_p = p_{jk} / p_{lk} \tag{7}$$

Power generation efficiency of power machine, η_d, can be calculated as the following:

$$\eta_d = p_{gk} / p_{jk} \tag{8}$$

Efficiency of marine tidal current power generation devices can be calculated with the following formula:

$$\eta = C_p \cdot \eta_d \tag{9}$$

Conversion efficiency of tidal current power generation systems is restrained by several factors. For example, sea state variation adds influence to the first stage of power system conversion, and output status of the first-stage conversion has influence on the second-stage power system conversion efficiency. In addition, for the magnitude of influences of various factors on power systems based on different principles is not identical, and in order to acquire an objective evaluation of power generation efficiency of marine energy power generation systems, a comprehensive consideration of different factors should be conducted, and magnitude of influences of different factors on conversion efficiency of various power generation systems should be measured. Only by this way, evaluation and analysis method of conversion efficiency of power generation system can be acquired, and purpose of improvement of design and conversion efficiency can be realized.

4 Measurement method of annual electricity production

Traditional method of measurement of annual electricity production of tidal current energy generation devices is based on long term on site demonstrating operation, which is not economically wise because of its long time occupation of the limited test resources of test sites. Therefore, after introducing relevant theories from physical oceanography and mathematical statistics into the research, and optimizing estimation method, annual electricity production of devices is estimated through a continuous test of a process containing a spring tide and a neap tide, in which test time consumption for estimation is reduced, and the operability of test method of the annual power generation of tidal current devices is strengthened. Accordingly, estimation method can be applied as follows: on the basis of the aforementioned analysis section division, test data sifted are counted, and frequency of occurrence of data falling into different analysis sections is acquired. Assuming 8760 hours constituting a year, and on the basis of power output characteristics analyzed before, annual electricity production of the device estimated can be calculated with the following formula: [13]

$$AEP = h_{AE} \sum_{i=1}^{N} \frac{a_i}{n} \times \overline{p}_{gi} \tag{10}$$

where *AEP* is the annual electricity production; h_{AE} is the annual power generating hours; *N* is the number of analysis sections involved in the calculation; *n* is the number of data points acquired in the measurement(total sampling times); a_k is the number of current velocities involved in data points acquired in the measurement falling into the section *i*; $\overline{p}_{gi}$ is the representative power output of the analysis section *i*.

It is worth noting that current field distribution characteristics and seasonal variation characteristics adjacent to tidal current berths in test sites should be analyzed.

5 Power quality test and evaluation

5.1 Power quality evaluation method

Power quality test of power output of tidal current devices involves two stages, long term stage and short term stage. Characteristic parameters of long term test include rated parameters of devices, power output characteristics, et al.; short term test requires high speed data acquisition and analysis, and the characteristic parameters include voltage fluctuation, voltage flicker, harmonic waves, etc. Besides, influences of devices on voltage

fluctuation and flicker are different between continuous operation and switching operation, which calls for measurement and evaluation of voltage fluctuation and flicker under the two operation modes separately.

The voltage fluctuation and flicker of the point of common coupling (PCC) should meet the conditions of "GB/T 12326-2008 power quality, voltage fluctuation and flicker" after the grid connection of wave energy and tidal current energy generation devices.

IEC61400-21 recommends that power system load flow analysis should be used to evaluate influence of grid connection of wind turbine generators on the grid voltage in the steady state, which aims to ensure voltage amplitude not to overrun the allowable range due to grid-connected operation of wind turbine generators [14]. During the grid-connected operation of tidal current generators, load flow analysis is also applied to conduct the evaluation.

According to the requirements of load flow analysis, power outputs of tidal current generators include largest allowable active power P_m and corresponding reactive power Q_m, or average active power and average reactive power within 60 seconds (P_{60}、Q_{60}), or average active power and average reactive power within 0.2 seconds. $P_{0.2}$ and $Q_{0.2}$ can be calculated as the following:

$$P_{0.2\Sigma} = \sum_{i=1}^{Z} P_{t,i} + \sqrt{\sum_{i=1}^{Z} \left(P_{0.2,i} - P_{t,i}\right)^2} \tag{11}$$

$$Q_{0.2\Sigma} = \sum_{i=1}^{Z} Q_{t,i} + \sqrt{\sum_{i=1}^{Z} \left(Q_{0.2,i} - Q_{t,i}\right)^2} \tag{12}$$

where $P_{t,i}$ is the rated active power of tidal current generator *i*; and $Q_{t,i}$ is the rated reactive power of tidal current generator *i*; and *Z* is the number of tidal current generators.

5.2 Voltage fluctuation and voltage flicker evaluation method

In continuous operation, evaluation method of voltage fluctuation and voltage flicker is shown in Fig. 1.

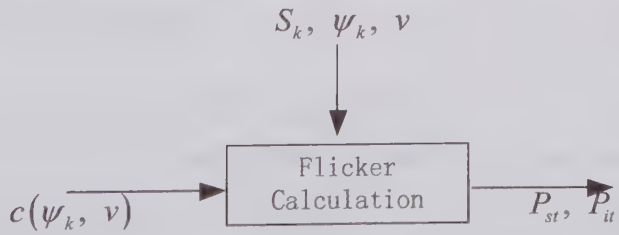

Fig. 1 Flicker assessment method in continuous operation

According to the requirements of IEC61000-3-7, long-term flicker values can be calculated by finding cubic roots of the average cubic value of the 12 continuous short term flicker values. Flicker of the tidal current generators is the function of ocean current velocity, whereas tidal current velocity can be invariable within two hours, which indicates that the 12 short-term flicker values can be equal as well. Based on the aforementioned analysis, long term flicker coefficient and short term flicker coefficient are identical for tidal current generators.

In continuous operation, quantile flicker values of single tidal current energy generator can be calculated by the following formula:

$$P_{st} = P_{it} = c(\psi_k, v)\frac{S_t}{S_k} \tag{13}$$

where $c(\psi_k, v)$ is the flicker coefficient of tidal current energy generator when grid impedance angle of PCC is ψ_k, and given annual average velocity of the ocean current is v, S_t is the rated apparent power of the tidal current energy generator; S_k is the short circuit capacity of the PCC; P_{st} is the short term flicker value; P_{it} is the long term flicker value.

Multiple tidal current energy generators are connected to the PCC, and total voltage flicker can be calculated as the following:

$$P_{st\Sigma} = P_{it\Sigma} = \frac{1}{S_k}\sqrt{\sum_{i=1}^{Z}\left(c(\psi_k, v)\cdot S_{t,i}\right)^2} \tag{14}$$

where $S_{t,i}$ is the rated apparent power of the tidal current generator i.

6 Research of safety access test method of tidal current energy device

In order to accurately evaluate safety bearing capacity of marine tidal current energy devices, and to improve the safety of operation process of marine power generation devices, establishment of a reasonable safety access standard is the prerequisite of normal operation of tidal current devices. Safety access test of tidal current device includes following aspects [9]:

(a) Appearance test of the system includes interior and exterior surface macroscopic check such as erosion, mechanical damage, deformation.

(b) Static test of the system. The device is generalized, and approved empirical formulae are applied to calculate the total force and total force moment and to make a

preliminary judgment on the overall security of the device itself.

(c) Dynamic simulation test on the field. After the installation of tidal current device on the test platform, both form of force and load born by devices and the platform under marine dynamic environment will change, which calls for a dynamic simulation test of the force form and load born by devices after their installation in the field, using numerical method before their actual installation.

(d) Dynamic test of the system structure. Observation data or fluid load calculated by using mathematical models are analyzed. Finite element numerical models of structures are built to study the form of force born, structure deformation and dynamic response of the overall device and the key components.

(e) Evaluation of vulnerable components. Pre-evaluation of the overall security of the tidal current devices under extreme environmental conditions during the operation is conducted to ensure the security of devices and the platform during the test and to lower the damage of the components. The evaluation mainly focuses on the overall tidal current energy generation device and its vulnerable key structural components.

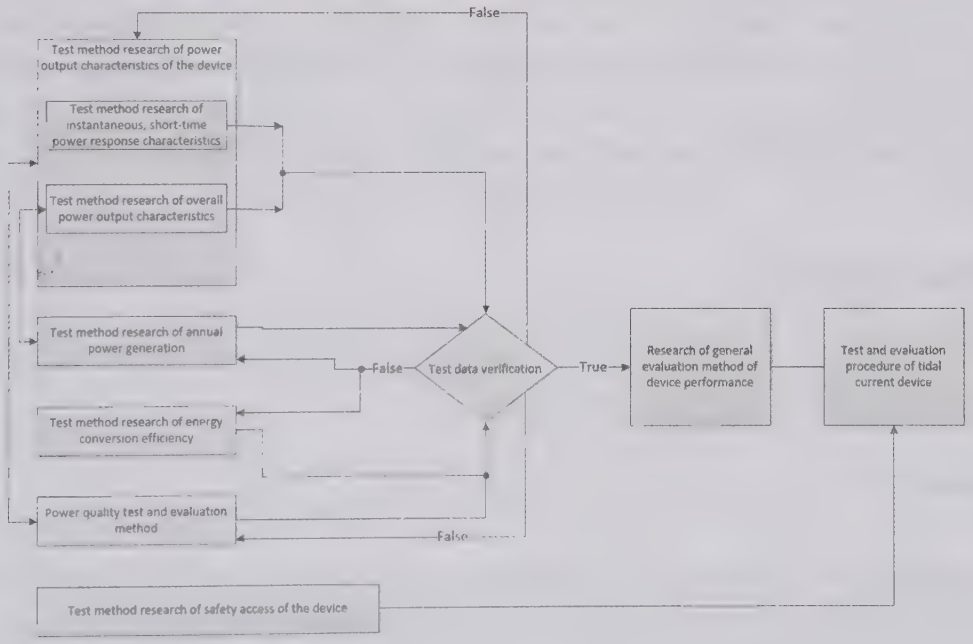
False
Test method research of power output characteristics of the device
Test method research of instantaneous, short-time power response characteristics
Test method research of overall power output characteristics
Test method research of annual power generation
False
Test data verification
True
Research of general evaluation method of device performance
Test and evaluation procedure of tidal current device
Test method research of energy conversion efficiency
Power quality test and evaluation method
False
Test method research of safety access of the device

Fig. 2 Method and research flow chart

Multi-spot stereoscopic observation and monitoring system will be applied to the test site in the aforementioned research to accurately determine the variable characteristics of offshore test sites, especially tidal current sites, wave sites and wind sites around berths of

the test site, and to get the motion law and extreme distribution of marine dynamic environment. Relevant methods of device acquisition test can be acquired after building the fluid-solid coupling computation method and models of marine dynamic environment, test devices and test platform being built, and testing the operation status, dynamic response and damage status of devices and platform under different external loads being tested.

7 Conclusions

With the objective of tidal current power generation, flow diagram of general testing and evaluation system method research is shown in Fig. 2, which includes three indices, power output characteristics, annual power output and power generation efficiency, and evaluation method of power quality of tidal current energy. Besides, multiple performance indices of devices such as environmental adaptability, stable operating hours and power output quality are also important measurement of the performance of tidal current devices. In addition, importance of different indices to devices also varies. Therefore, research should be carried out to determine reasonable weight of each index and to analyze correlation between the indices. Then, a set of complete and objective general evaluation method can be figured out. In the research, focus has been put on the physical background of characteristics of devices in order to find out internal relations and ways of mutual influence, and reasonable evaluation of operating status of tidal current devices is expected.

Acknowledgments

This paper is supported by the Implementation Programs for Marine Renewable Energy Special Funds (GHME2012ZC02).

References

[1] XIONG Y, WANG H F, CUI L, et al. Development strategy on development and utilization of marine renewable energy in China [J]. Ocean Technology, 2009, 28(03): 106 - 110.

[2] ZHU Y Q. New energy and distributed generation technologies [M]. Beijing: Peking University Press, 2010.

[3] YOU Y G, LI W, LIU W M, et al. Development Status and Perspective of Marine Energy Conversion Systems [J]. Automation of Electric Power Systems, 2010, 34(14): 1 - 12.

[4] Bfrigaard P, Kofoed J P, Rasmussen M R. Overtopping measurements on the Wave Dragon

Nissum Bredning prototype [C]. 14thAnnual Int, Offshore and Polar Engineering Conf. ISOPE, Toulon, France, 2004.

[5] EMEC. The years of marine energy experience [EB/OL]. http://www.emec.org.uk/, 2013.

[6] YUAN P, WANG S J, Shi H D. Overview and Proposal for Development of Ocean Energy Test Sites in China [C]. OCEANS 2012 MTS of IEEE. Yeosu, South Korea, 21-24 May, 2012.

[7] LI Y, LUO X Y, LU K. Tide energy, wave energy test sites construction analysis of main problems [J]. Ocean Development and Management, 2013, 02: 36 - 39.

[8] ZHANG R. Research on tidal current energy exploitation standards system [D]. Shandong: Ocean University of China, 2012.

[9] ZHANG Y F, ZHANG Z K, ZHANG J, et al. Research progress of marine spatial planning in the occident [J]. Marine Science Bulletin, 2013, 32(03): 353 - 360.

[10] National Marine Technology. Implementation Programs for Marine Renewable Energy Special Funds [R]. Tianjin, 2012.

[11] CUI L. Study on Gravitational Horizontal Axis Conversion Device Design of Tidal Current Energy [D]. Heilongjiang: Harbin Engineering University, 2012.

[12] ZHANG L, LI L F, SHENG Q H. Marine tidal current energy generation device power and efficiency test method research report [EB/OL]. http://wenku.baidu.com/view/898671c658f5f61fb736666b.html, 2011-03-19/2013-09-10.

[13] SHEN H Q. Economic analysis of electrical system and test about tidal current energy farm [D]. Beijing: North China Electric Power University, 2013.

[14] LI Q. Power Characteristics of Wind Turbines and Wind Farms and Power Quality Testing Research [D]. Beijing: China Electric Power Research Institute, 2006.

海上试验场潮流能发电装置综合测试与评价方法分析

郭文瑞[1]，朱永强[1]，叶 青[1]，李雪临[2]，王 鑫[2]，段春明[3*]

（1. 华北电力大学 电气与电子工程学院，北京 102206；2. 国家海洋技术中心，天津 300112；
3. 国网冀北电力有限公司 电力经济技术研究院，北京 100045）

摘 要：开展潮流能装置实海况试验、检测与评价方法研究，对海洋高科技成果的转化、海洋可再生能源开发提供了科学、有效的技术保障。文章通过对潮流能装置的功率输出特性、年发电量、能量转换效率三项核心指标进行分析，提出指标的测试内容和评价方法，为实现潮流能海上试验与测试场建设提供技术依据；并根据对海上风电场的研究，提出了海上试验场潮流能装置的电能质量测试与评估方法；给出潮流能装置安全准入的测试内容，全面评估试验场潮流能装置的运行状态。

关键词：试验场；潮流能；发电装置；综合测试；评价方法

Research on the characteristics of the vortex field of breakwaters by the PIV technique

QIE Lu-wen[1], XIA Qian[1], ZHANG Xiang[1], JIANG Xue-lian[2]

1. *College of Architecture and Civil Engineering of Hebei University, Baoding* 071002, *Hebei province, China;*

2. *Tianjin Institute of Urban Construction, Tianjin* 300384, *China*

Abstract: The flow field around the submerged breakwater has complex turbulent change; and breakwater is more prone to the damage. By the PIV technique, and based on the model test, the research about velocity flow field and eddy characteristics of submerged breakwater under the action of regular waves has been carried out, and the velocity distribution of flow field can be obtained. By analyzing the experimental data under different hydraulic conditions of different breakwaters, the vortex field characteristics around breakwaters are quantitatively studied.

Keywords: regular wave; particle image velocimetry technique; breakwater; vortex characteristics

Particle Image Velocimetry (PIV) Technique, which is a contactless transient flow field image analysis, was developed at the end of 1970's for measuring multi points in the 2D flow field. Unlike the single point measurement techniques, such as Laser Doppler Velocimetry (LDV), the PIV technique has the advantage that the large point velocity distribution information of flow field can be transiently recorded, and 3D flow field structure and its flow characteristics can be provided by PIV. PIV technique can distribute tracer particles to the flow field, and what's more, all the measuring equipments are not involved into the flow field, and it has the characteristics of undisturbance, accuracy, and efficiency when it measures the velocity distribution in the form of two-dimensional flow field. PIV technique is the latest development in the flow visualization research and it is accompanied with the development of high and new technologies such as fiber-optical, microelectronics, laser, digital signal processing and graphic image processing, which is widely used in other fields nowadays.

Over the years, the vortex wave flow theory receives much attention from many investigators. However, due to the limitation of the early experimental fluid mechanics and testing techniques, most of the previous researchers used the camera to take pictures of

Received on Jul. 9, 2014

Corresponding author: qieluwen@hbu.edu.cn

flow fields, and the vortex wave flow field were compared and analyzed qualitatively, but the accurate description of the formation mechanism of vortex wave has not been obtained. Pedley et al (1985) took pictures with a parallel light into the fluid on the wall cyclical compression channel, to observe the static photos of vortical wave-current field. Sobey (1985) used Nikon cameras with 250W flash in the periodic oscillation of the fluid through the channel employing the pearl powder as tracer particles to qualitatively analyzed the scroll wave and current characteristics of the field. The PIV technique does not interfere with the state of the original flow field, and the measured flow rate with a high degree of accuracy and precision. Fengxia Liu (2006) analyzed vortex flow field velocity and shear force distribution with PIV. Aihua Liu et al (2006) analyzed the characteristics of the eddy and obtained some important results using the PIV technique. Dong Min(2007) used PIV technique to research the process of the breaking wave affecting on the straight wall structures, and the characteristics of breaking wave force. Xiaojing Long(2009) studied the research of PIV technology in the wave flume, and analyzed the instantaneous velocity field of the entire test flow field. Dekui Yuan(2004) studied the hydraulic characteristics of the semi-circular breakwater which was based on the method and application of numerical simulation. Changgen Liu et al made use of time-varying Reynolds equation to simulate the interaction of solitary wave and the semi-circular breakwater with the steps, and studied the effect of Smoothed Partical Hydrodynamics (SPH) method between water waves and semi-circular breakwater.

Since the complex turbulent changes exist in the flow field around deepwater breakwaters, the breakwaters are prone to be damaged.

In this paper, an experimental test on periodic regular waves passing through the submerged breakwater has been conducted, and the instantaneous velocity distribution of wave field was obtained by using PIV technique. Through the analysis and settlement of experimental data, the characteristics of vortex wave flow field before and after the body of breakwater were studied quantitatively.

1 Test design and parameters

1.1 Test arrangement and process

The model experiment was taken at the State Key Laboratory of Coastal and Offshore Engineering of Dalian University of Technology. The experimental process was shown in Fig. 1 and Fig. 2. The test device mainly consisted of four parts: channel, reciprocating pump, PIV system and the external trigger device. The channel was made of organic glass, in order to realize the visible flow (see Fig. 3).

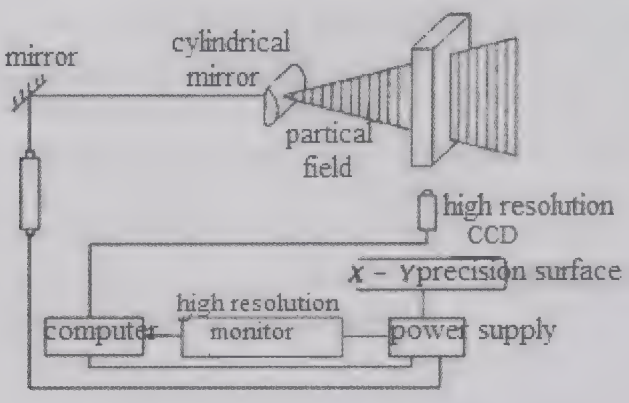

Fig. 1 PIV system diagram

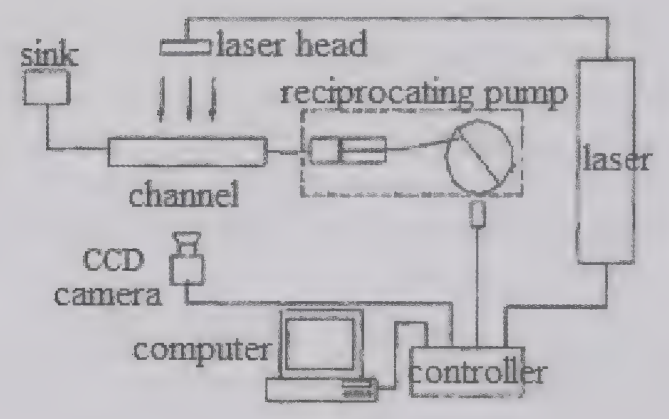

Fig. 2 PIV experiment flowchart

Fig. 3 Experiment site

Three types of breakwaters were used in the experiment, including Vertical breakwater (VB), Quarter-circular Breakwater (QB), Semi-circular Breakwater (SB), as shown in Fig. 4 – Fig. 6.

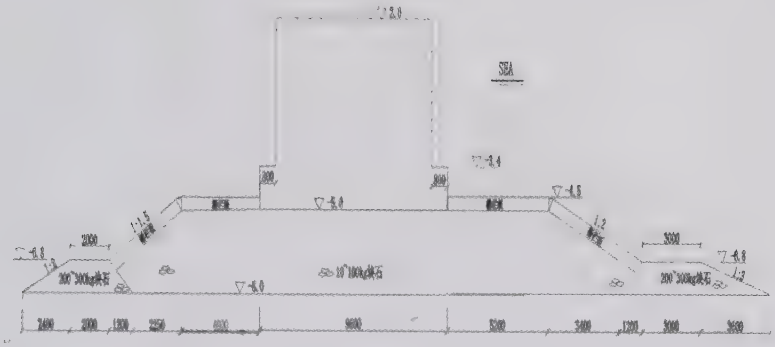

Fig. 4 Schematic diagram of VB model

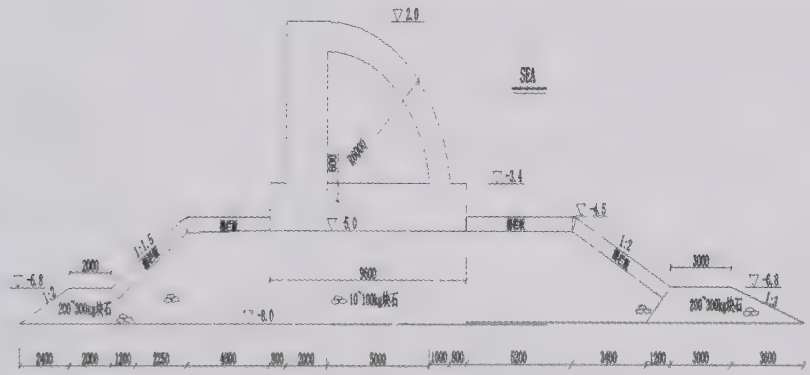

Fig. 5 Schematic diagram of QB model

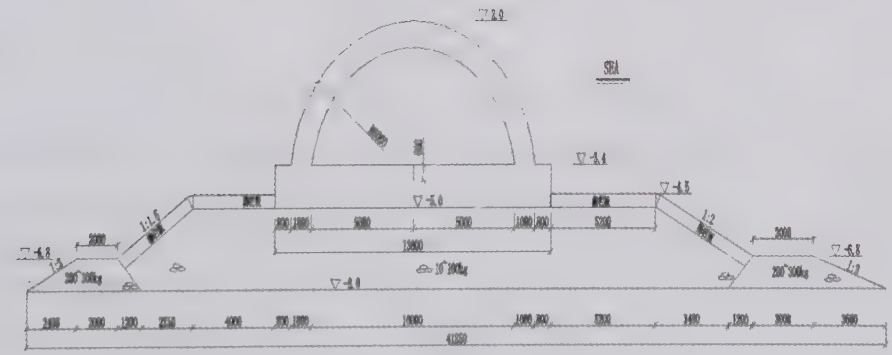

Fig. 6 Schematic diagram of SB model

Six kinds of wave hydraulic conditions were designed in the test. The experimental hydraulic conditions were listed in Tab. 1.

Tab. 1 Experimental hydraulic conditions

conditions	water depth D/m	wave height H/m	period T/s	wave length L/m	wave steepnessH/L
01	0.333	0.118	1.233	1.901	0.062
02	0.333	0.093	1.233	1.901	0.049
03	0.333	0.068	1.233	1.901	0.036
04	0.333	0.118	0.996	1.401	0.084
05	0.333	0.093	0.996	1.401	0.066
06	0.333	0.068	0.996	1.401	0.048

The experimental equipment layout of section model was shown in Fig. 7.

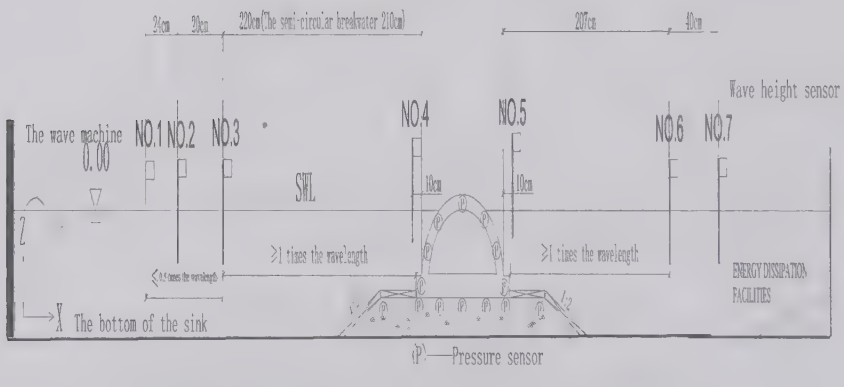

Fig. 7 Schematic diagram of experimental arrangement

Collection points located at No.4 and No.5 were shown in Fig. 7. When the figure on the left side of the wave machine began to make waves, it would pass through the No. 5 wave-height gauge. When three complete period images of waves were reflected in the data acquisition, the wave information began to be recorded. When regular period wave images were all shown on the terminal screen, the computer stopped the collection. The interval of wave probe collection was 0.02 s, and the chosen time of data section was 16s. It was the data range from the sample collection of 800 times. As shown in the right side of Fig. 7, it used gravels to build the slop for wave dissipation, which could avoid secondary waves interfering with experimental data.

1.2 Definition of vorticity

Vorticity is a vector, and the numerical value is equal to the rotation of the velocity vector , which is defined as follows:

$$\Omega = \frac{\partial W}{\partial x} - \frac{\partial U}{\partial z}$$

where Ω represents the vortex value of the flow field measurement, and *U*, *W* represent horizontal velocity and vertical velocity of water particle respectively. Using the central difference method, it can be calculated as:

$$\Omega_p = \frac{\partial W}{\partial x} - \frac{\partial U}{\partial z} \cong \left[\frac{W_{i+1,k} - W_{i-1,k}}{x_{i+1,k} - x_{i-1,k}}\right] - \left[\frac{U_{i,k+1} - U_{i,k-1}}{z_{i,k+1} - z_{i,k-1}}\right]$$

where Ω_p represents the vortex value of particle position at point (i,k). i,k represent the array code of the x,z direction. Positive Ω_p represents the counterclockwise vortex, and negative Ω_p represents the clockwise vortex.

2 Data processing and analyzing

Using PIV technique, we experimented with six kinds of working conditions of section waves in this study, and 45 instantaneous (interval=0.15s) at each measuring point velocity were collected for each hydraulic condition. The number of measuring points of sampling area was 48 × 35=1680. After the analysis of the measured velocity and vortex value, the velocity field diagram and vortex field contour plot can be obtained.

2.1 Relationship between velocity and vortex

The velocity values of each measuring point at each time can be calculated through experiment data collected by the computer, and as well as the vortex of observation area and the distribution of vortex field. Fig. 8 shows the velocity field and the contrast between vortex contours with vortex field of a semi-circular breakwater at the same time in No.1 hydraulic condition.

From the above, the speed of concentration and higher velocity variation rate place can be observed, and that is the region easily forming the higher vorticity. Also it confirms the previous formula that is the intrinsic link between the speed and vorticity.

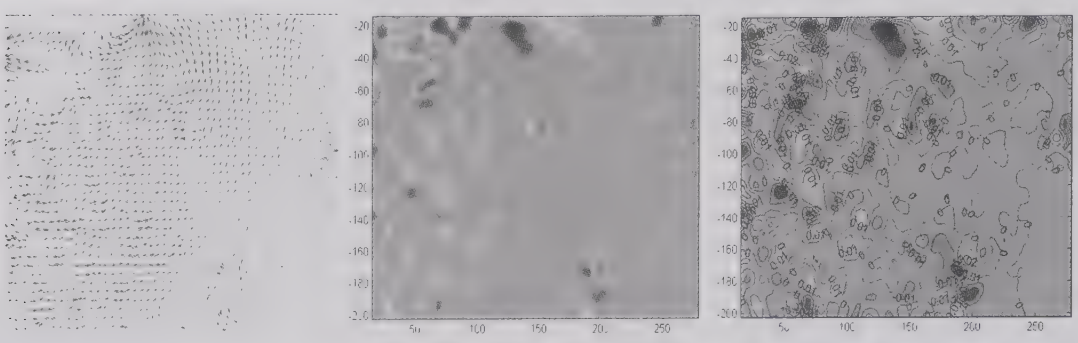

Fig. 8 Velocity, vortex field and vortex contour plot of SB

2.2 Wave process and vortex distribution

Using PIV technique, wave information was collected for 3 seconds during the test in order to obtain the process about 3 periods, corresponding to 45 frames that each frame interval was 1/15 seconds. Wavefront and PIV images were collected simultaneously, but the position was not completely overlapped. Wave height gauge can monitor the reflection coefficient and transmission coefficient, in order to compare the changes of coefficient and transmission with different vortex situation. Wave gauges were collected for 800 times, and the interval was 0.02 s.

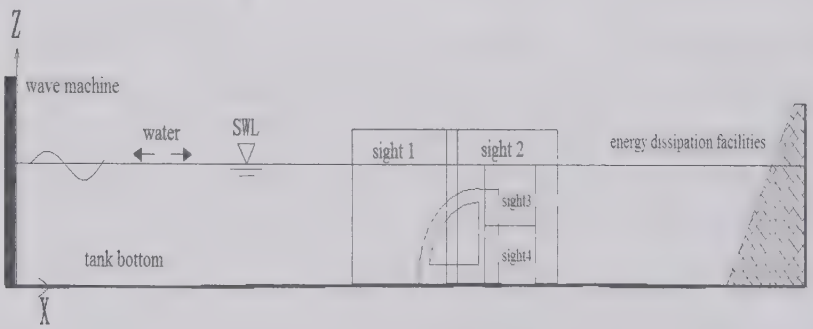

Fig. 9 Data collection area plan

In this experiment, the wave front process curve of a semi-circular breakwater and the algebraic mean curve of vortex value were shown in Fig. 10 - Fig. 12. From the above results, the vortex algebraic mean curve and wave front process curve do not coincide, then we get that:

(1) The regularity of the curve of front side of breakwater is opposite to the back one.

(2) The alternation of wavelength will not change the correlation of the original vortex algebra mean curve and wave front curve, but it will make the original correlation become

more obvious.

(3) The alternation of wave period will affect the correlation of the original vortex algebra mean curve and wave front curve.

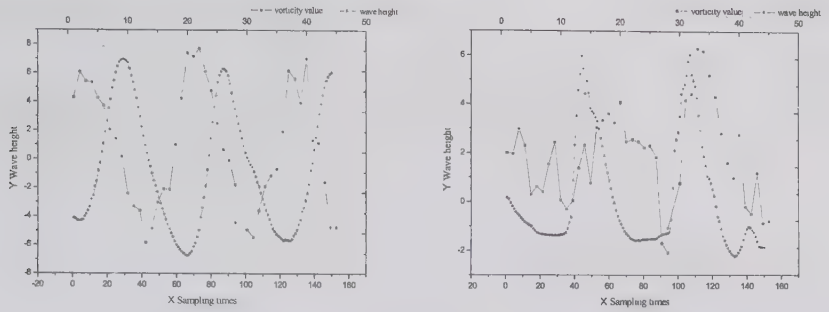

Fig. 10 Wave and vortex value curve of back side and front side of SB under the hydraulic condition 1

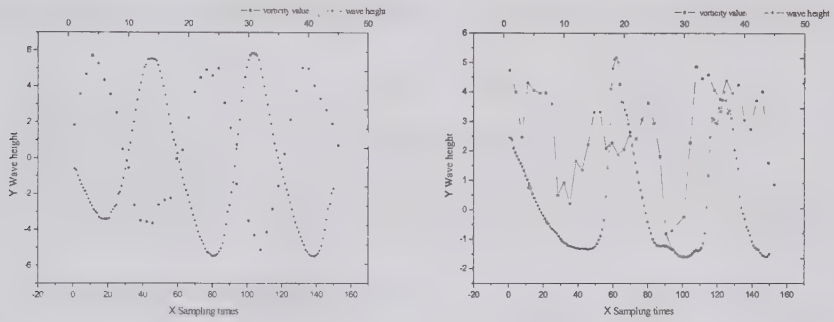

Fig. 11 Wave and vortex value curve of back side and front side of SB under the hydraulic condition 2

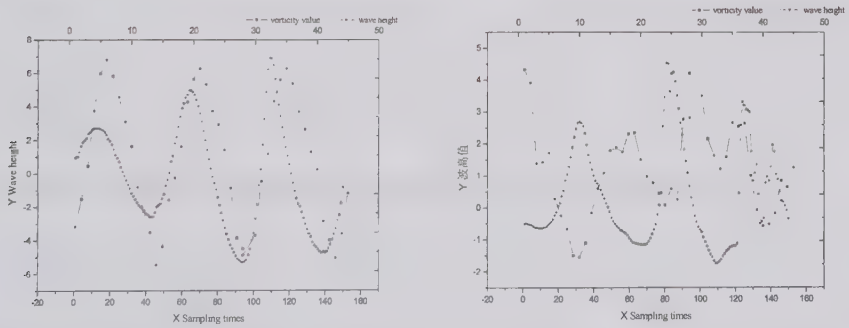

Fig. 12 Wave and vortex value curve of back side and front side of SB under the hydraulic condition 4

2.3 Analysis of vortex numerical characteristics

2.3.1 Analysis of vortex algebraic value at random measurement point

In order to research the formative rules of vortex value, the back of wave surface of a

semi-circular breakwater was analyzed, and the measuring points of different lines were randomly selected. (The water depths of point 1, 2, 3 within the same column increased in turn. Point 1, 2, 3 within the same row were away from the sea in turn.) In the sampling period, vortex value curves before and after the embankment and vortex algebraic curve have the same rules. The curves of measuring points within the same column have the same rules, as well as the trend, which is similar to QB, VB.

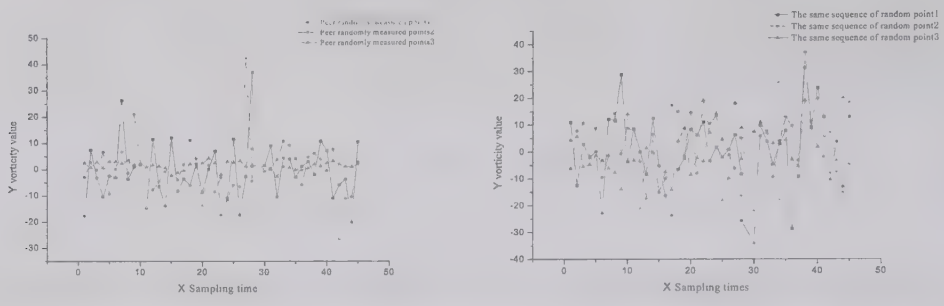
Peer randomly measured points2
Peer randomly measured points3
Y vorticity value
X Sampling time
The same sequence of random point1
The same sequence of random point2
The same sequence of random point3
Y vorticity value
X Sampling times

Fig. 13 Vortex algebraic curve of random points within the same lines of SB

2.3.2 Analysis of the most value of vortex algebra

The most vortex values of three breakwaters have been analyzed in the same hydraulic conditions. In the sampling interval, the minimum and maximum values for each case could be drawn as the following diagrams.

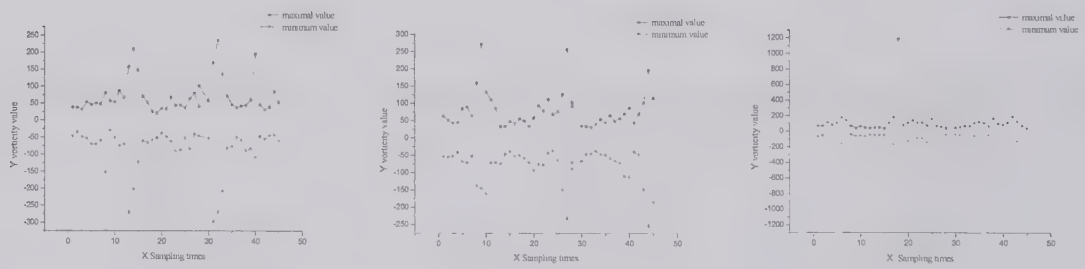

Fig. 14 Extreme value curve of the front wave surface of SB, QB and VB

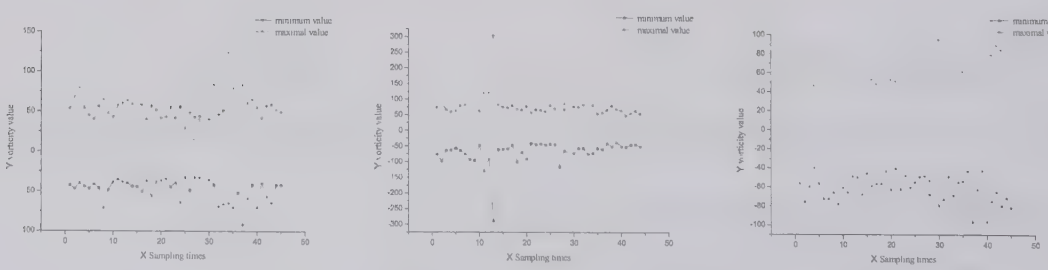

Fig. 15 Extreme value curve of the back wave surface of SB, QB and VB

Quantitative analysis of the experimental results about three kinds of breakwaters showed that the maximum and minimum values of the vortex of SB were 86% and 117% of QB in the front area of breakwater. In the back of breakwater, the values would be 40% and 30%, and the values of the vortex of VB were 31% and 33% of QB.

2.3.3 Analysis of vortex mean value

In the first hydraulic condition, the vortex mean values produced on each frame in the sampling interval about three kinds of breakwaters were analyzed. The mean curves of 45 frames could be drawn as follows:

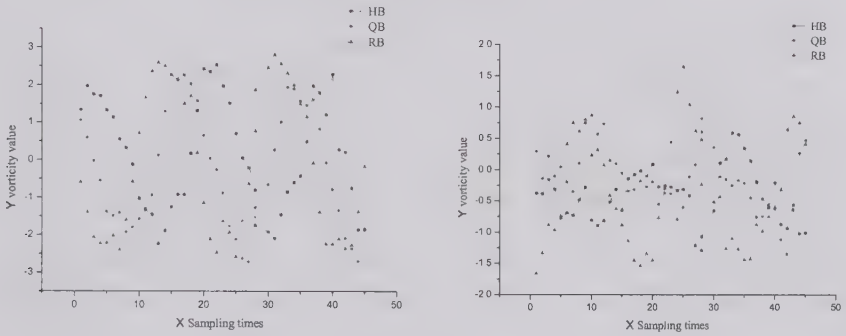

Fig. 16 Vorticity algebraic mean value curve of front and back of the wave surface of breakwaters

From the figure above, the characteristics of mean curve were similar to the sinusoidal curve, and the features before the breakwater were more obvious than those at the back. It was clear that vortex motion was very weak in the rear area of waves closing to the breakwater surface, whereas the bottom of the vortex motion became severe away from breakwater. However, the case of front side of waves was just the opposite, and vortex motion became severe closing to the surface. It was almost the same on the measuring points of other parts, and they changed smoothly.

2.3.4 Vortex algebraic value analysis with different wave heights

For the same breakwater in different hydraulic conditions, the numerical difference among the vortex was studied. The semi-circular breakwater was chosen in this test, and the numerical differences were studied in the case of wave height changes.

From Fig. 17 and Fig. 18, we can see that there was a positive correlation between the wave height and the vortex value. The higher the wave height was, the greater the maximum value was (the smaller the minimum value was). The vortex mean curve followed a sinusoidal curve. Numerical curve at the side was more stable than that at the back of breakwaters, and the characteristic was more obvious.

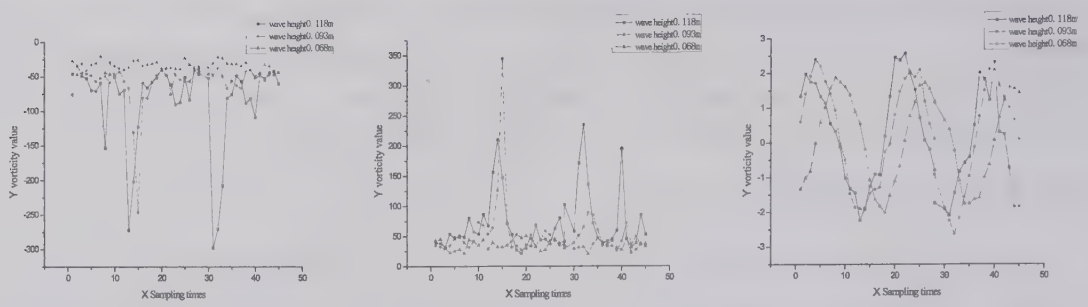

Fig. 17 Vorticity algebra minimum, maximum, mean curve of the front wave surface in three kinds of wave heights of SB

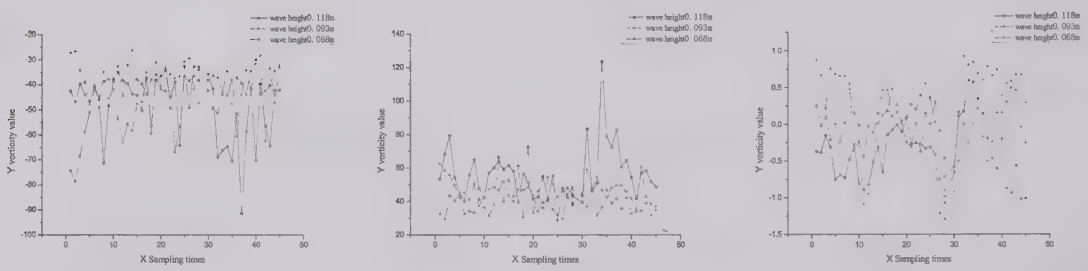

Fig. 18 Vorticity algebra minimum, maximum, mean curve of the back wave surface in three kinds of wave heights of SB

2.3.5 Vortex characteristics analysis of breakwaters in different wave periods

The vortex values were analyzed with the experimental data that were chosen in the condition No.1 and condition No.4.

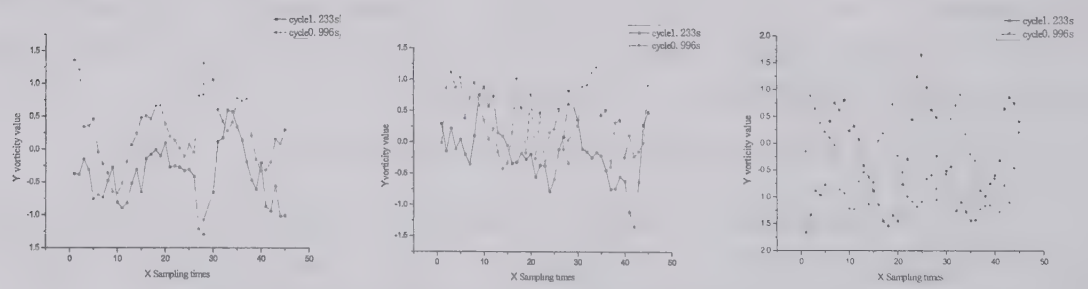

Fig. 19 Comparison of the vorticity back wave surfaces of SB, QB, VB

From the figures above, the vortex accumulation of the SB and QB increased with the wave period decreases, but the case of vertical breakwater was opposite. All of the algebraic mean curves reflected the characteristics of sinusoidal curve. With the wave period decreasing, the back of breakwater would generate more vorticities. The curve

characteristics of QB and VB were obvious, showing features of a sinusoidal curve. The wave period change influenced the sinusoidal fluctuation, and the phase difference between two curves approximate reached half a period.

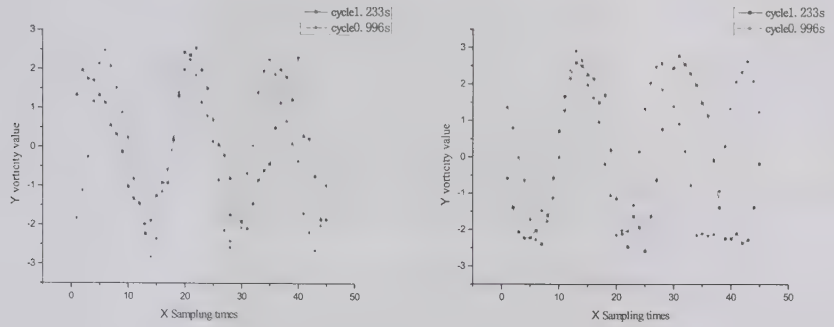

Fig. 20 Comparison of the vorticity algebra mean value of SB, VB in different hydraulic conditions

The front and back of breakwaters were slightly different. In the front part of the breakwater with the period reducing, the vortex motion was slight, and it was opposite at the back area. And the impact of wave period change in the vortex curve cycle was not obvious. From Fig. 20, we can see that, when the period decreased from 0.996s to 1.223s (approximately 18.6% reduction), the amplitude of mean vortex mean value of SB increased about 16%, and the average reduction of VB was approximately 4.5%.

2.4 Analysis of vortex formation and distribution characteristics for the back of different breakwaters

For three kinds of breakwaters, the obstruction of vorticity formation was not the same for each. While in the same kind of wave condition, the area of high vorticity value was also different for each.

For the semi-circular breakwater, the positive vorticity area mainly concentrated in the upper left of sampling area, and that was close to the back side of breakwater (as shown in Fig. 21a). While negative vorticity area mainly concentrated in the midfield zone of sampling area (as shown in Fig. 21b). That was to say, away from the back side of breakwater, it generated more clockwise swirl, and more counterclockwise swirl would be at the midfield zone. These vortex distribution would produce corresponding movement over time, positive vorticity area moving adjacent to the breakwater, and the original areas became the negative vorticity area (as shown in Fig. 21c). After some time, the positive vorticity region would return to its original position, and the negative vorticity region back to midfield. For the semi-circular breakwater, zero vorticity region appeared less throughout

the sampling period (as shown in Fig. 21d), and the sampling intervals were mostly affected by the vortex.

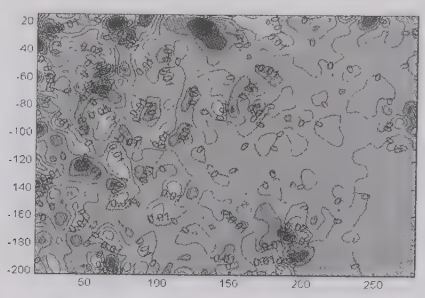

Fig. 21a 1 frame vorticity field of SB

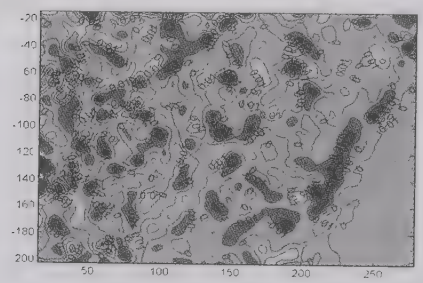

Fig. 21b 6 frame vorticity field of SB

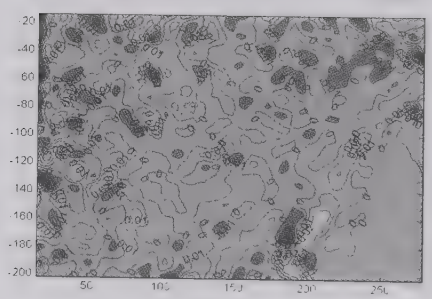

Fig. 21c 15 frame vorticity field of SB

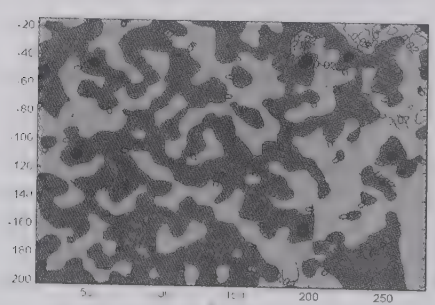

Fig. 21d 31 frame vorticity field of SB

For the quarter-circular breakwater, positive and negative vorticity intervals often appeared concomitantly, and there was no obvious difference between them. At the beginning, they appeared together in the upper left of sampling area, away from the back side of breakwater (Fig. 22a). Then they moved together to the upper middle part of the sampling area (Fig. 22b), and gradually disappeared, and finally came back to the initial position (Fig. 22c). The entire period was longer for the case of semi-circular breakwater. Relative to semi-circular breakwater, during the whole sampling period, the time of zero vorticity region increased in the central sampling area (Fig. 22d), and in contrast to the semi-circular breakwater, the generated vortex was more weaker in the sampling area.

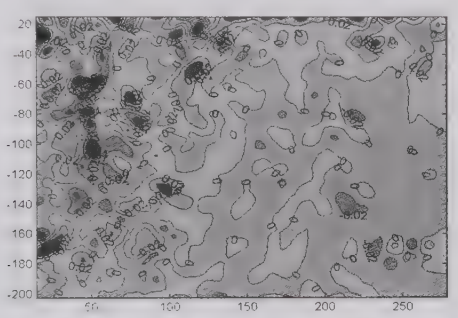

Fig. 22a 1 frame vorticity field of QB

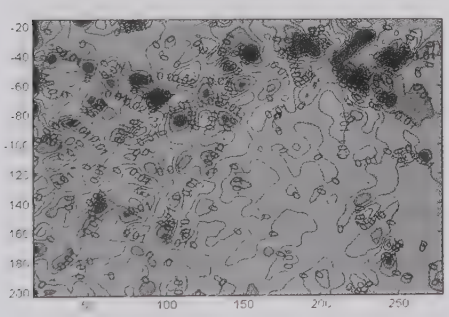

Fig. 22b 10 frame vorticity field of QB

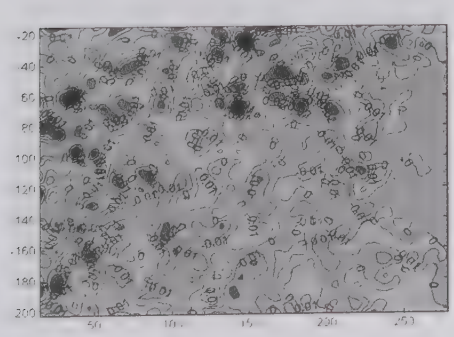

Fig. 22c 42 frame vorticity field of QB

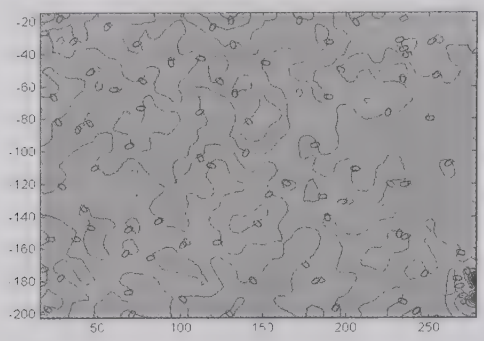

Fig. 22d 13 frame vorticity field of QB

For the vertical breakwater, the positive and negative vorticity areas concentrated in the upper part of the sampling area (Fig. 23a), and the scope was small. The two areas appeared concomitantly, and they became smaller gradually over time (Fig. 23b), but after a period of time, they recovered the initial state (Fig. 23c). In the cases of SB and QB, there had been the most zero vorticity areas in the sampling area of VB (Fig. 22d). That was to say, Vortex region was formed relatively small in the sampling interval.

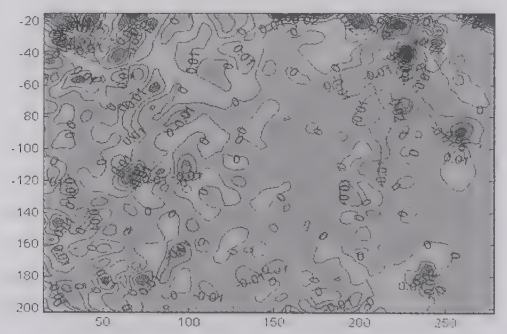

Fig. 23a 1 frame vorticity field of VB

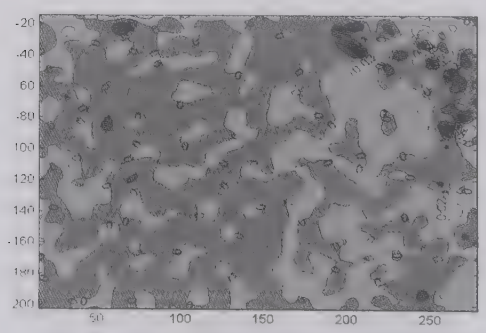

Fig. 23b 5 frame vorticity field of VB

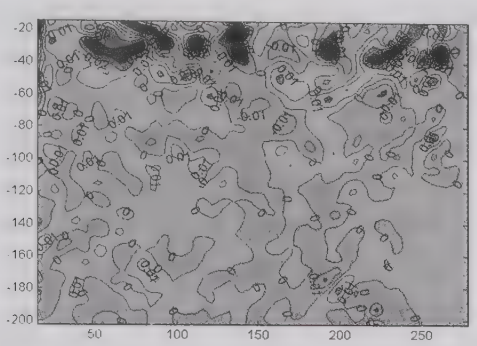

Fig. 23c 26 frame vorticity field of VB

3 Conclusions

By using PIV technique, and based on model experiments, the surface velocity field of breakwater and its vortex characteristics under the action of regular waves were investigated experimentally in this paper. By analyzing the experimental data under different hydraulic conditions of different breakwaters, the vortex field characteristics around breakwaters were quantitatively studied.

(a) There is a correlation between wave motion and vortex in the area, which is affected by the wave period and frequency, and the breakwater will change this correlation.

(b) In the same area, the vortex positive and negative extreme values appear symmetrically at the same time.

(c) In the place close to the surface of breakwater, vortex motion becomes violent, and at the bottom, away from the breakwater, vortex motion becomes weak and vortex motion is violent at the place close to the sea level. The case of the front wave surface is just the opposite.

(d) There is a positive correlation between the wave height and vortex value. The increase of wave period will affect the accumulation and production of vortex. The smaller the period is, the more vortex motion is, but the increase of accumulation is unchanged. The vortex mean value curve shows a sinusoidal nature, especially at the front side of the breakwater.

(e) The bottom of breakwater has a slip influence on the bottom of breakwater because of the vortex effect. It is the most violent for the quarter circle breakwater, then the semicircle case is the modest, and the vertical breakwater is the weakest.

(f) In the same hydraulic conditions and the collecting area of the back of wave surface, the vortex motion's migratory model and the aggregated distribution of three kinds of breakwater are similar, but the intensity and the size of vortex is variable. Compared with the other two types, the vertical breakwater's vortex motion is weaker in the sampling area at the back of breakwater, and the migration period is shorter.

Acknowledgements

This paper is supported by the Natural Science Foundation of Hebei province (E2012201057) and Open Fund of Key Lab of Hydraulic Engineering Simulation and Safety of Tianjin university (HESS-1310).

References

[1] Okajina A. Strouhal Nunmbers of Retangular Cylinder [J]. Fluid. Mech., 1982, 123: 379 - 398.

[2] Sobey I J. Observation of Waves During Oscillatory Channel Flow [J]. Fluid. Mech., 1985, 151: 395 - 426.

[3] Westerwell J. Fundamentals of digital particle image velocimetery [J]. Measurement Science and Technology, 1997, 8(12):1 379 - 1 392.

[4] Shen Gongxin. Concept trace trend on full field observation and measurement techniques [J]. Journal of Beijing University of Aeronautics and Astronautics, 1997, 23(3): 332 - 340.

[5] Duan Li, Kang Qi, Shen Gongxin. Image processing method of PIV technique [J]. Journal of Beijing University of Aeronautics and Astronautics, 2000, 2(1): 79 - 82.

[6] Wang Jun, Li Guoyuan, Wen Guozhen, et al. Test of flow inside hydraulic vortex core using PIV techniques and its analysis [J]. Journal of Hua Zhong University of Science and Technology(nature science edition), 2004, 12(12): 66 - 68.

[7] Sun Hequan, Shen Yongming, Wang Yongxue, et al. Introduction of algorithms used in PIV technique [J]. Advances in water science, 2004, 15(1): 105 - 108.

[8] Liu Fengxia, Shi Qicai, Liu Zhijun, et al. Investigation on the characteristics of vortex wave flow by PIV [J]. Journal of Experimental Mechanics, 2006, 21(5): 611 - 616.

[9] Liu Aihua, Hou Qinfu, Wang Huanyang, et al. Application of PIV in study of swirling flow tundish [J]. Journal of Materials and Metallurgy, 2006, 5(1): 26 - 29.

[10] Liu Fengxia, Liu Zhijun, Wang Lin, et al. On The Measurement of Velocities and Stress in Vortex Wave Field with Particle Image Velocimetry [J]. Journal of experimental mechanics, 2006, 3(6): 378 - 284.

[11] LI Yanbao, Kong Hui, Jiang Xuelian. Expected sliding distance model of meandering damage to the caisson breakwater [J]. Marine science bulletin, 2007, 26(2): 78 - 87.

[12] Dong Min. Experimental investigation of the breaking wave loads on a vertical-wall structure [D]. Master's thesis of Dalian University of Technology, 2007.

[13] Qi Erong, Lu Weijuan, Qiu Lan, et al. Research on vortices of cross flow past a horizontal square cylinder by PIV system [J]. Engineering Journal of Wuhan University: Engineering science, 2007, 40(1): 19 - 24.

[14] Shi Xiaojun, Wang Shuli, Li Tianen, et al. Experimental Study on Testing Flume Field with PIV [J]. Journal of Anhui University of Technology, 2008, 25(2): 151 - 154.

[15] Long Xiaojing. Particle Image Velocimetry Investigation on Waves in flume [D]. Master's thesis of Tianjin University, 2009.

[16] Li Hongfei, Song Wenwu. Application of PIV in the Test and Study of Flow Field [J]. Journal of Xihua University, Natural Science, 2009, 9(5): 27 - 31.

[17] Jiang Xuelian, Li Shanshan, Li Yanbao. Analytical solution of breakwater sliding and its application [J]. Marine science bulletin, 2012, 31(4): 441 - 448.

基于 PIV 技术不同形式防波堤周围涡旋场特性研究

郅禄文[1]，夏 乾[1]，张 翔[1]，蒋学炼[2]

（1. 河北大学建筑工程学院 河北 保定 071002；2. 天津城市建设学院 天津 300384）

摘 要：深水防波堤周围流场存在复杂的紊动变化，防波堤较容易发生失效破坏。本文利用 PIV 技术，基于模型实验，对规则波作用下防波堤周围的速度流场及其涡流特性进行了实验研究，获得了规则波流场的瞬时速度分布。通过对不同型式防波堤在不同的水力条件下的波浪流场实验数据的分析，定量地研究了防波堤堤身水域的涡旋流场的水力特性。

关键词：规则波，PIV 技术，防波堤，涡流特征

Comprehensive evaluation of water quality parameters in Tianjin Dagu Dainage Canal

DONG Yu-bo[1], DAI Yuan-yuan[2*], MA Chao[2], SUN Xue-liang[3]

1. *Fisheries Research Institute of Tianjin, Tianjin* 300221, *China;*

2. *Tianjin Bohai Sea Fisheries Research Institute, Bohai Sea Fisheries Research Center, Chinese Academy of Fishery Sciences, Tianjin* 300457, *China;*

3. *Tianjin Key Laboratory of Aquatic Ecology and Aquaculture, Department of Fisheries Science, Tianjin Agricultural College, Tianjin* 300380, *China*

Abstract: In this paper, some indices of sulfide, organic carbon, oil and heavy metals (copper, lead, zinc, cadmium, mercury, arsenic and chromium) in the sediments from Dagu Dainage Canal at the Bohai Bay during four seasons in 2012 - 2013 are selected, and Water Quality Pollution Index (API) is applied to evaluate water quality indices, aiming for the systematic evaluation of the water quality of Dagu Dainage Canal. The results showed that four stations of D3, D6, D7and D9 for S^{2-} had the type Ⅱ and Ⅲ of water; others had the type Ⅰ; the total level of TOC, TPH, Cu, Pb, Zn, Cd, Hg, As and Cr were type Ⅰ, Ⅳ, Ⅱ, Ⅴ, Ⅱ, Ⅴ, Ⅲ, Ⅴ and Ⅴ. Water Quality Pollution Index (API) was 3.28, which illustrated Dagu Dainage Canal was in the state of contamination and the degree of pollution exceeded the standard functional areas.

Keywords: Dagu Dainage Canal; water quality indices; spatial and temporal distribution; comprehensive evaluation

Dagu Dainage Canal is the drainage of the secondary river artificial excavation [1]. With the rapid development of urban industrial and population growth, the daily discharge of sewage and industrial effluent were untreated directly into rivers and lakes[2], and the urban sewage and waste matter emissions had generated contamination which made Dagu Dainage Canal not competent to carry, drain, and draw off floodwater [3]; and ecological and environmental degradation near the shore, decreased the fishery resource seriously [5]. Contamination of Haihe River Basin is studied, and pollution situation and spatial and temporal distribution of sediments in Haihe River Basin [4, 6-8] and Bohai Bay are investigated [5]. Therefore, this paper selected some water quality indicators of Dagu Dainage Canal, and comprehensively evaluated water quality based on the comprehensive evaluation.

Received on Jan. 31, 2013

*Corresponding author: dai-yuanyuan2007@163.com

1 The data sources

The data in this paper were from the National Marine Environmental Monitoring Bulletin for sediments of 2012 - 2013including sulfide, organic carbon, oil and heavy metals (copper, lead, zinc, cadmium, mercury, arsenic and chromium) in Dagu Dainage Canal .

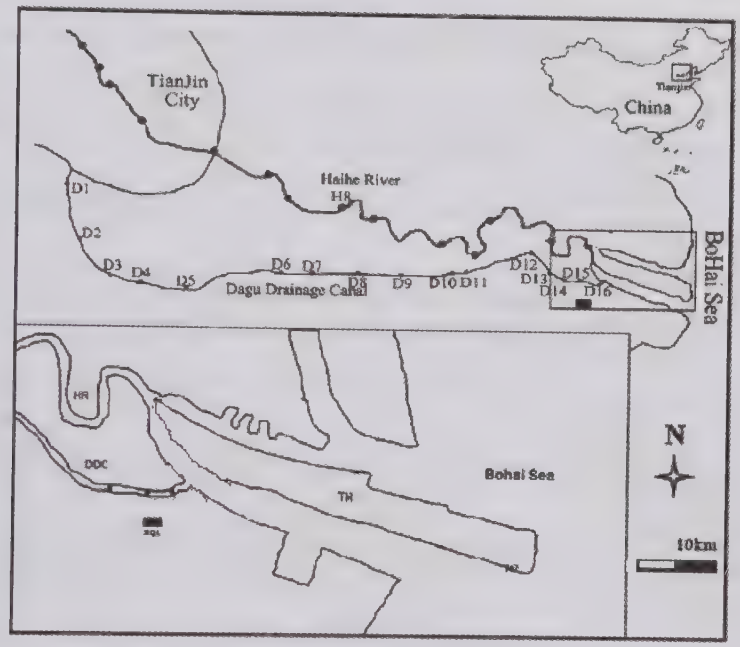

Fig.1 Dagu Dainage Canal station

2 Infusions and analysis

2.1 The main indicators for monitoring the water

The data of 2012 - 2013 for four seasons were collected and analyzed. The results are shown in Tab. 1.

The trend of concentration for each water quality index in different stations is as follows: the concentrations of S^{2-} are higher in stations of D3, D6, D7 and D9, which is related to the urban and industrial activities; the concentrations of TOC are In line with the standard of surface water; the concentrations of other water quality indices show a clear spatial distribution, which is close to the mouth of Bohai Sea.

Tab. 1 Monitoring indicators of each station

The station	Latitude and longitude	The main indicators for monitoring (Unit: mg/L)									
		S^{2-}	TOC	TPH	Cu	Pb	Zn	Cd	Hg	As	Cr
D1	117° 9' 38.523" E, 39° 2' 6.218" N	0.002	0.50	0.12	1.00	0.51	0.56	0.05	0.0001	0.75	0.58
D2	117° 10' 25.754" E, 38° 59' 5.172" N	0.003	0.55	0.09	0.94	0.54	0.54	0.05	0.0002	0.87	0.41
D3	117° 12' 0.218" E, 38° 57' 19.368" N	0.117	0.43	0.09	0.77	0.51	0.45	0.04	0.0002	0.67	0.64
D4	117° 14' 9.592" E, 38° 56' 40.883" N	0.003	0.48	0.10	0.69	0.46	0.49	0.06	0.0004	0.75	0.51
D5	117° 17' 6.197" E, 38° 56' 28.053" N	0.004	0.53	0.09	1.00	0.56	0.53	0.07	0.0001	0.78	0.69
D6	117° 22' 51.194" E, 38° 57' 32.195" N	0.182	0.65	0.09	0.82	0.51	0.47	0.07	0.0001	0.69	0.80
D7	117° 24' 54.407" E, 38° 57' 28.988" N	0.167	0.46	0.09	0.80	0.49	0.48	0.08	0.0002	0.64	0.46
D8	117° 27' 44.852" E, 38° 57' 38.608" N	0.001	0.46	0.09	0.75	0.49	0.49	0.06	0.0001	0.63	0.62
D9	117° 30' 35.297" E, 38° 57' 32.195" N	0.239	0.50	0.10	0.75	0.50	0.47	0.08	0.0001	0.69	0.53
D10	117° 33' 48.331" E, 38° 57' 51.435" N	0.002	0.76	0.11	0.71	0.44	0.42	0.07	0.0001	0.75	0.46
D11	117° 34' 54.045" E, 38° 57' 57.847" N	0.024	0.50	0.10	0.64	0.43	0.46	0.09	0.0001	0.56	0.62
D12	117° 38' 48.150" E, 38° 59' 3.569" N	0.008	0.27	0.09	0.71	0.52	0.47	0.09	0.0004	0.75	0.53
D13	117° 39' 51.810" E, 38° 58' 4.260" N	0.009	0.21	0.07	0.55	0.50	0.46	0.04	0.0001	0.50	0.46
D14	117° 40' 41.095" E, 38° 57' 30.592" N	0.002	0.30	0.11	0.57	0.44	0.43	0.04	0.0001	0.53	0.50
D15	117° 41' 36.541" E, 38° 57' 28.988" N	0.004	0.22	0.10	0.66	0.46	0.47	0.04	0.0001	0.50	0.41
D16	117° 43' 4.844" E, 38° 57' 25.782" N	0.003	0.26	0.07	0.69	0.47	0.44	0.04	0.0001	0.50	0.46

Combined with the actual situation, we select nine indicators for the evaluation: S^{2-}, TOC, TPH and heavy metals (Cu, Pb, Zn, Cd, As, Cr).

The specific formula is as the following:

$$P = \frac{1}{\mathrm{n}}\sum P_i = \frac{1}{n}\sum \frac{C_i}{S_i}$$

where C_i is the measured values and S_i is the quality standard values.

Referring to Tab. 2, P is 3.28. Combined with the Tab. 3, P is greater than 2.0, and most stations of Dagu Dainage Canal have heavy pollution.

2.2 Statistical analysis

2.2.1 Water quality

The following figures are drawn according to the monitoring data of each station in Tab. 1.

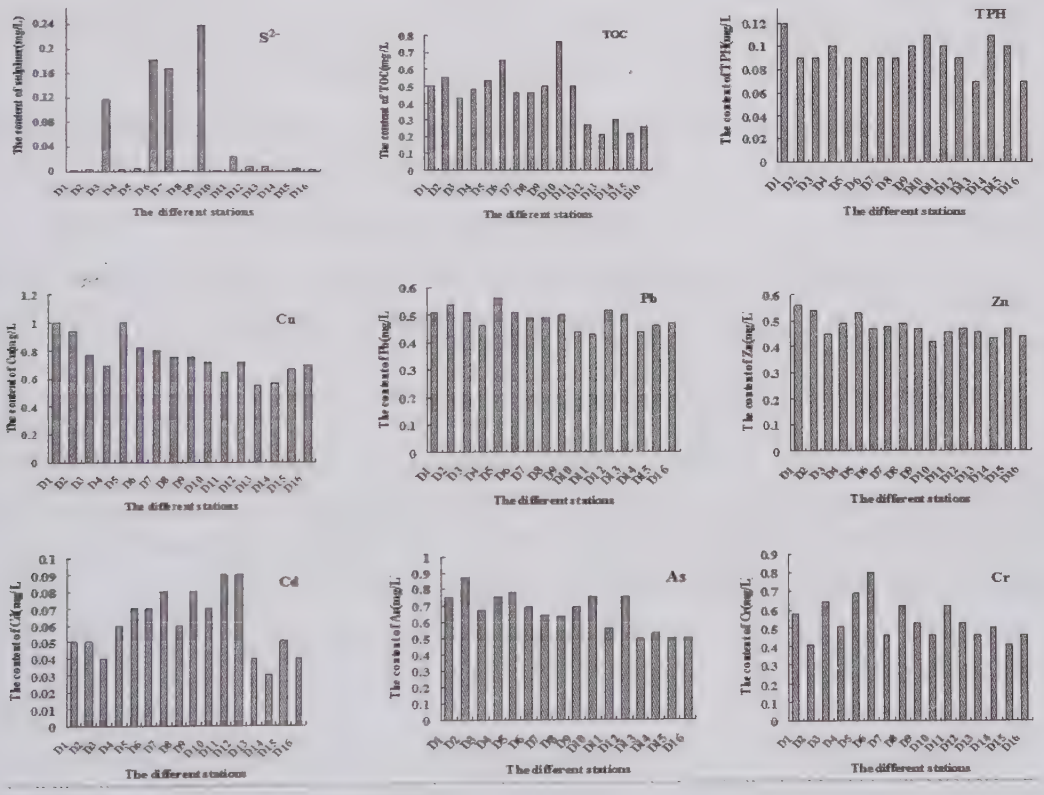

Fig. 2 Water quality Indices for different stations in Dagu Dainage Canal

Tab. 2 The levels for pollution indices

	I		II		III		IV		V	
	C_i	P_i	C_i	P_i	C_i	P_i	C_i	P_i	C_i	P_i
S^{2-}	0.05	0.96	0.1	0.48	0.2	0.24	0.5	0.10	1.0	0.05
TOC	1.5	0.30	2.5	0.18	4.5	0.10	8.0	0.06	8.0	0.06
TPH	0.05	1.88	0.05	1.88	0.05	1.88	0.5	0.19	1.0	0.09
Cu	0.01	75.30	1.0	0.75	1.0	0.75	1.0	0.75	1.0	0.75
Pb	0.01	48.90	0.01	48.90	0.05	9.78	0.05	9.78	0.1	4.89
Zn	0.05	9.54	1.0	0.48	1.0	0.48	2.0	0.24	2.0	0.24
Cd	0.001	61.00	0.005	12.20	0.005	12.20	0.005	12.20	0.01	6.10
As	0.05	13.20	0.05	13.20	0.05	13.20	0.1	6.60	0.1	6.60
Cr	0.01	54.30	0.05	10.86	0.05	10.86	0.05	10.86	0.1	5.43

Tab. 3 Standards

P	Judgment result
P≤0.8	Qualified, indicating that water quality objectives can basically achieve the appropriate functional criteria, with individual exceeding one time
0.8<P≤1.0	Basically qualified, a small number of indicators over the appropriate category standard, but there is no obvious damage to the water
1.0<P≤2.0	Pollution, most indicators will be restricted
P>2.0	Heavy pollution, the total number is more than the standard, with some indicators over several times, and water function subject to serious harm.

Tab. 4 shows the standard of national surface water quality.

The water quality of Dagu Dainage Canal is at Level Ⅴ. The causes of this phenomenon may be due to the deposition from atmosphere and the input from the upper stream outside Tianjin City, since no discharge is allowed in the whole reach in Tianjin to protect its function as a reserved resource for drinking water.

3 Conclusions

(1) The results show that four stations of D3, D6, D7 and D9 for S^{2-} have the type Ⅱ and Ⅲof water, and others belong the type Ⅰ; the total levels of TOC, TPH, Cu, Pb, Zn, Cd, Hg, As and Cr are type Ⅰ, Ⅳ, Ⅱ, Ⅴ, Ⅱ, Ⅴ, Ⅲ, Ⅴand Ⅴ.

(2) Water Quality Pollution Index (API) is 3.28, which illustrates Dagu Dainage Canal in the state of contamination that the degree of pollution exceeds the standard.

(3) Dagu Dainage Canal has potential ecological risk.

Tab. 4 Analysis results of monitoring indicators for all stations

The station	The main indicators for monitoring (Unit: mg/L)									
	S^{2-}	TOC	TPH	Cu	Pb	Zn	Cd	Hg	As	Cr
D1	I	I	IV	II	V	II	V	III	V	V
D2	I	I	IV	II	V	II	V	III	V	V
D3	II	I	IV	II	V	II	V	III	V	V
D4	I	I	IV	II	V	II	V	III	V	V
D5	I	I	IV	II	V	II	V	III	V	V
D6	II	I	IV	II	V	II	V	III	V	V
D7	II	I	IV	II	V	II	V	III	V	V
D8	I	I	IV	II	V	II	V	III	V	V
D9	III	I	IV	II	V	II	V	III	V	V
D10	I	I	IV	II	V	II	V	III	V	V
D11	I	I	IV	II	V	II	V	III	V	V
D12	I	I	IV	II	V	II	V	III	V	V
D13	I	I	IV	II	V	II	V	III	V	V
D14	I	I	IV	II	V	II	V	III	V	V
D15	I	I	IV	II	V	II	V	III	V	V
D16	I	I	IV	II	V	II	V	III	V	V
The total level	III	I	IV	II	V	II	V	III	V	V

Acknowledgements

This research is financially supported by Key Laboratory of Marine Oil Spill Identification and Damage Assessment Technology, State Oceanic Administration (201214) and Key Laboratory of Pollution Processes and Environmental Criteria (Nankai University), Ministry of Education (KL-PPEC-2013-09).

References

[1] Fasong Li, Hongwen Sun, Zhineng Hao. Perfluorinated compounds in Haihe River and Dagu Drainage Canal in Tianjin, China [J]. Chemosphere, 2011, 2(84): 265 - 271.

[2] Yanwei Zhang, Yuefei Ruan, Hongwen Sun. Hexabromocyclododecanes in surface sediments and a sediment core from Rivers and Harbor in the northern Chinese city of Tianjin [J]. Chemosphere, 2013, 5(90): 1 610 - 1 616.

[3] Ge Yu, Jing Chen, Xueqing Zhang, et al. Comprehensive analysis of an ecological risk assessment of the Daliao River estuary, China [J]. Environ. Monit. Assess., DOI 10.1007/s10661-013-3065-y.

[4] Qiuying Chen, Jingling Liu, Kin Chung Ho, et al. Development of a relative risk model for evaluating ecological risk of water environment in the Haihe River Basin estuary area. Science of The Total Environment [J], 2012(420): 79 - 89.

[5] Ning Jing Hu, Xue Fa Shi, Peng Huang. Polycyclic aromatic hydrocarbons in surface sediments of Laizhou Bay, Bohai Sea, China [J]. Environ. Earth Sci., 2011, 63:121 - 133.

[6] Cheng Y M, Zhu L Y, Tian S Y, et al. Distribution and sources of polycyclic aromatic hydrocarbons in surface sediments from the Haihe River and the Bohai Sea [J]. Acta Scientiae Circumstantiae, 2009, 29(11): 2 420 - 2 426.

[7] LUO Xian-xiang, ZHANG Q iu-yan, YANG Jian-qiang. Total Petroleum Hydrocarbon Contamination Characteristics in Shuangtaizi EstuaryWetlands [J]. Research of Environmental Sciences, 2010, 23(4):437 - 444.

[8] GUO Liang-Bo , JIANG Wen-Sheng , LI Feng-Qi. Environmental Capacity Calculation of COD and PAHs in the Bohai Sea [J]. Journal of Ocean University of China, 2007, 37 (2) :310 - 316.

天津大沽排污口水质参数综合评价

董玉波[1]，戴媛媛[2*]，马 超[2]，孙学亮[3]

（1. 天津市水产研究所，天津 300221；2. 天津渤海水产研究所 中国水产科学院渤海水产研究中心，天津 300457；
3. 天津农学院水产科学系，天津市水产生态及养殖重点实验室，天津 300380）

摘 要：本研究对 2012～2013 年大沽排污口沉积物中硫化物、有机碳、石油类以及 7 种重金属（铜、铅、锌、镉、总汞、砷和铬）等水质指标的监测数据进行统计，并对其中重要的水质指标进行水污染综合指数评估，旨在对海河水质进行较为系统的评价。结果显示，D3、D6、D7 和 D9 四个站位水质属于 II 和III类标准，其余各站位均为 I 类；其余各指标（TOC、TPH、Cu、Pb、Zn、Cd、Hg、As and Cr）的总体水平依次为 I、IV、II、V、II、V、III、V和V类。各站位综合评价结果得到海河流域指数为 3.28，说明海河流域处于严重污染状态，其污染程度超过该流域功能区的标准。

关键词：大沽排污口；水质参数；时空分布；综合评价

海 洋 通 报（英文版）

HAIYANG TONGBAO

2014 年 10 月 第 16 卷 第 2 期

目 次

基于舰船耐波性的中国近海海浪特征统计 …… 刘首华 等 (12)

温州鳌江近海建设工程环境影响潮汐潮流数值模拟 …… 吕和娜 等 (27)

实验室长波引起的同流低频频移 …… 岳心阳 等 (36)

海南儋州人工岛建设对海床冲辨影响数值模拟 …… 英晓明 等 (45)

基于遥感的天津滨海新区土地利用/覆盖变化分析 …… 王 丰 等 (59)

海上试验场潮流能发电装置综合测试与评价方法分析…… 郭文瑞 等 (71)

基于 PIV 技术不同形式防波堤周围涡旋声特征研究 …… 郄禄文 等 (89)

天津大沽排污口水质参数综合评价 …… 董玉波 等 (96)

Marine Science Bulletin

Marine Science Bulletin publishes papers on marine science and technology including physical oceanography, chemical oceanography, marine biology, marine geology, environmental oceanography, estuarine & coastal sciences, marine technology, digital ocean, coastal zone management, ocean engineering, marine economics, etc., and aims to promote international academic exchange.

Editor-in-Chief: XU Sheng (徐　胜)

Associate Editor-in-Chief: LI Dong-xu (李东旭)　XUE Hui-feng (薛惠芬)

Executive Editor: QIU Wen-jing (邱文静)　DONG Yi (董　艺)　LI Xiao-guang (李晓光)
LI Xue (李　雪)　YANG Rui (杨　瑞)　YUAN Ze-yi (袁泽轶)

English proofed by: WANG Qi (王　琦)

Semi-annually (started in 1999, sum 32)
Publication date: May 15th and Oct. 15th

Marine Science Bulletin **(Vol. 16, No. 2, Oct. 2014)**

Responsible Institution:
State Oceanic Administration of China
Sponsored by:
National Marine Data and Information Service
Edited by:
Office of Marine Science Bulletin (English edition)
Printed by:
Printery of National Marine Date and Information Service

Published by:
Office of Marine Science Bulletin (English edition)
E-mail: msb@mail.nmdis.gov.cn
Tel: (022) 24011287
Address: 93 Liuwei Rd., Hedong District, Tianjin 300171, China

ISSN1000-9620
CN12-1271/N

ISSN 1000-9620

Price: $ 30.00 / ￥40.00 Per year